INFORMATION TO USERS

This manuscript has been reproduced from the microfilm master. UMI films the text directly from the original or copy submitted. Thus, some thesis and dissertation copies are in typewriter face, while others may be from any type of computer printer.

The quality of this reproduction is dependent upon the quality of the copy submitted. Broken or indistinct print, colored or poor quality illustrations and photographs, print bleedthrough, substandard margins, and improper alignment can adversely affect reproduction.

In the unlikely event that the author did not send UMI a complete manuscript and there are missing pages, these will be noted. Also, if unauthorized copyright material had to be removed, a note will indicate the deletion.

Oversize materials (e.g., maps, drawings, charts) are reproduced by sectioning the original, beginning at the upper left-hand corner and continuing from left to right in equal sections with small overlaps.

Photographs included in the original manuscript have been reproduced xerographically in this copy. Higher quality 6" x 9" black and white photographic prints are available for any photographs or illustrations appearing in this copy for an additional charge. Contact UMI directly to order.

ProQuest Information and Learning
300 North Zeeb Road, Ann Arbor, MI 48106-1346 USA
800-521-0600

Strange Phases in Neutron Star Matter

Travis T. Norsen

A dissertation submitted in partial fulfillment of
the requirements for the degree of

Doctor of Philosophy

University of Washington

2002

Program Authorized to Offer Degree: Physics

ProQuest Information and Learning Company
300 North Zeeb Road
P.O. Box 1346
Ann Arbor, MI 48106-1346

In presenting this dissertation in partial fulfillment of the requirements for the Doctoral degree at the University of Washington, I agree that the Library shall make its copies freely available for inspection. I further agree that extensive copying of this dissertation is allowable only for scholarly purposes, consistent with "fair use" as prescribed in the U.S. Copyright Law. Requests for copying or reproduction of this dissertation may be referred to Bell and Howell Information and Learning, 300 North Zeeb Road, Ann Arbor, MI 48106-1346, to whom the author has granted "the right to reproduce and sell (a) copies of the manuscript in microform and/or (b) printed copies of the manuscript made from microform."

Signature 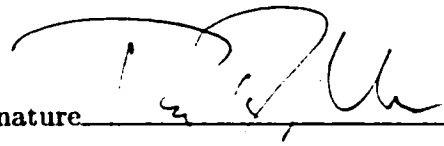

Date 6-13-02

University of Washington

Graduate School

This is to certify that I have examined this copy of a doctoral dissertation by

Travis T. Norsen

and have found that it is complete and satisfactory in all respects,
and that any and all revisions required by the final
examining committee have been made.

Chair of Supervisory Committee:

Wick Haxton

Reading Committee:

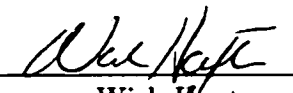

Wick Haxton

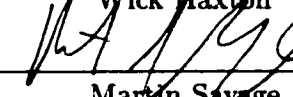

Martin Savage

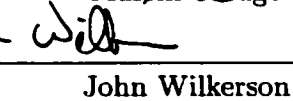

John Wilkerson

Date: 6-13-02

University of Washington

Abstract

Strange Phases in Neutron Star Matter

by Travis T. Norsen

Chair of Supervisory Committee:

Professor Wick Haxton
Department of Physics

Neutron stars are produced in nature as the remnants of core-collapse supernovae. Their masses lie in the range $1 - 2\,M_\odot$ and they possess radii of order $10\,km$, yielding central densities of several times the density of nuclear matter at saturation. At these extreme densities, the usual degrees of freedom of low-energy matter (neutrons, protons, and electrons) will be supplemented by more exotic components. In particular, matter containing strange quarks is expected to appear beyond some critical density in the form of hyperons, negative kaons, or perhaps three-flavor quark matter. After reviewing relevant background material, in this thesis we focus on the possibility of a first-order phase transition to a state containing a condensate of negative kaons. We calculate the importance of finite-size effects in a kaonic-nuclear charge-separated mixed phase. ("Finite-size effects" here refers to surface-tension-induced pressure differences between the two phases and Debye screening corrections to the charged particle distributions.) We then discuss the question of when and how the kaonic phase is nucleated during the formation of a neutron star. The results of nucleation rate calculations are presented and analyzed in detail, including a discussion of the implications to the interpretation of observational data. Finally, we turn to an alternative form in which kaons may appear in high-density matter. This involves the condensation of kaon-like mesons in a background of flavor-symmetric superconducting quark matter. We present the results of a stability analysis designed to identify whether a homogeneous or a

heterogeneous condensate is energetically favored. We conclude by summarizing the new work presented, discussing its limitations, and indicating directions for future work.

TABLE OF CONTENTS

LIST OF FIGURES

ACKNOWLEDGMENTS

Thanks to Wick for putting up with my unconventional style and to Sanjay for helping me find a path leading to graduation. Sarah's honest vision helped keep me moving in the right direction. And thanks to AR, LP, HB, and DW for occasionally reminding me what it's all for.

Chapter 1

INTRODUCTION TO NEUTRON STARS: FORMATION, PROPERTIES, AND OBSERVATIONS

The new work presented in this thesis concerns several issues involving the structure of matter at very high density. Such matter is expected to occur in nature in the interiors of neutron stars. In this introductory chapter, we discuss the formation and basic properties of neutron stars, as well as reviewing the observational evidence used to constrain the theoretical models that will be addressed and developed in detail later.

1.1 Core-Collapse Supernovae

Neutron stars are believed to be produced during the death throes of very massive stars with $M \gtrsim 10 M_\odot$. Here $M_\odot = 2 \cdot 10^{30} kg$ is the mass of our sun. At the end of their early, hydrogen-burning phase, such massive stars contract somewhat under their own gravitational weight. The work done by gravity during the contraction increases the temperature and density in the star's core to the point at which the triple alpha process $\alpha + \alpha + \alpha \rightarrow {}^{12}C$ ignites, initiating a helium-burning phase.

When the helium fuel begins to run out, additional gravitational contraction again heats and compresses the star's core, igniting burning phases for heavier elements. These cycles continue, producing an onion-skin structure with heavier and heavier elements being burned at deeper and deeper layers within the star. Once the nuclear burning produces iron, however, additional energy can no longer be extracted by further fusion reactions, since iron is the most deeply bound nucleus. (That is, the binding energy per nucleon is greater in iron than in any other element.) Hence, a core of relatively inert iron begins to develop in the center of the star, with nuclear burning above continuing to produce iron, increasing

the size of the core. Subsequent burning phases beyond the initial hydrogen-burning phase proceed at an accelerating pace: the original hydrogen burning phase may last for millions of years, while the final stage in which silicon is burned to iron lasts only a matter of days.

Because no additional energy can be extracted from iron by nuclear reactions, the iron core is unable to contribute any thermal pressure to the star's ability to support itself. What then prevents the core from simply collapsing under the weight of the material above? The answer is the degeneracy pressure of electrons — but as we will show, even this has a limit beyond which the star cannot avoid a cataclysmic collapse.

The density in the iron core is of order $\rho \sim \text{few} \cdot 10^9 g/cm^3$. Most of this mass comes simply from the mass of the proton and neutron constituents of iron, so we may write: $\rho \sim m_N(n_n + n_p)$ where $m_N = 939MeV$ is the nucleon mass and $n_{(n,p)}$ are the neutron and proton number densities. Equating these two expressions for the energy density, we find $n_n + n_p \sim \text{couple} \cdot 10^{-6} fm^{-3}$. (Here couple = few/1.782.) Since the nuclei in the core are mostly iron, we also have $Y_p = n_p/(n_n + n_p) \approx 26/56$ giving a proton number density of order $n_p \approx 10^{-6} fm^{-3}$. Note we have set $\hbar = c = 1$ here, and have switched to the same typical nuclear physics units (e.g., expressing number densities in fm^{-3}) that will be most convenient later.

Because the bulk matter in the core must be electrically neutral, the electron number density will also be given by $n_e = n_p \approx 10^{-6} fm^{-3}$. We may treat the electrons as a homogeneous Fermi gas and thus relate the number density to the Fermi energy:

$$n_e = 2 \int_0^\infty \frac{d^3k}{(2\pi)^3} g_F(k,T) \tag{1.1}$$

where $g_F(k,T)$ is the Fermi-Dirac distribution function. Upon assuming the $T = 0$ form $g_F(k,0) = \theta(\mu_e - E(k))$ and ignoring the electron mass m_e, becomes

$$n_e = 2 \int_0^{k_F} \frac{d^3k}{(2\pi)^3} = \frac{\mu_e^3}{3\pi^2}. \tag{1.2}$$

where μ_e is the electron chemical potential. The overall factor of 2 is due to the two independent spin states of the electron. We made two approximations: we assumed the gas was relativistic so that the electron mass m_e could be ignored in $E(k) = \sqrt{k^2 + m_e^2}$ (implying, in particular, that $k_F = \mu_e$), and we assumed that $T = 0$. Using our earlier

estimate for n_e to solve for μ_e from the last line gives $\mu_e \sim 5 - 6MeV$. This is an order of magnitude greater than both the electron mass and the typical expected temperature of the iron core (Silicon burning occurs at about $T \sim 0.5MeV$), so the two approximations introduce only about 10% corrections.

The total energy density can be rewritten in terms of the electron chemical potential as follows:

$$\begin{aligned} \rho &= m_N(n_n + n_p) = m_N \frac{(n_n + n_p)}{n_p} n_e \\ &= \frac{m_N}{Y_p} \frac{\mu_e^3}{3\pi^2}. \end{aligned} \tag{1.3}$$

We may also write a simple expression for the electron degeneracy pressure using the standard ($T = 0$) thermodynamic relation $\Omega_e = \epsilon_e - \mu_e n_e = -P_e$. Here ϵ_e is the energy density in the electron gas

$$\epsilon_e = 2 \int_0^{\mu_e} \frac{d^3k}{(2\pi)^3} k = \frac{\mu_e^4}{4\pi^2}. \tag{1.4}$$

This then gives for the pressure

$$P_e = \frac{\mu_e^4}{12\pi^2} \tag{1.5}$$

which we recognize as the usual result for a relativistic gas: $P = \epsilon/3$.

The structure of the iron core is determined by the condition of hydro-static equilibrium, which requires the net upward force on a shell of matter (due to the slightly higher pressure below as compared to the pressure above) to just cancel the inward force of gravity. In terms of the pressure and total energy density, the condition reads:

$$\frac{dP(r)}{dr} = \frac{-GM(r)\rho(r)}{r^2} \tag{1.6}$$

where

$$M(r) = \int_0^r 4\pi r'^2 \rho(r') dr' \tag{1.7}$$

is the total mass inside the radius r and G is Newton's gravitational constant. Dividing both sides by $\rho(r)/r^2$ and differentiating with respect to r allows us to write Equations 1.6 and 1.7 as a single second-order differential equation

$$\frac{d}{dr} \frac{r^2}{\rho(r)} \frac{dP(r)}{dr} = -4\pi G r^2 \rho(r) \tag{1.8}$$

which can be solved for a given equation of state — that is, relation between the pressure and energy density $P(\rho)$ — by picking a value for the central density $\rho(0)$ and integrating outward. Note that the second boundary condition at $r = 0$ is that $d\rho(0)/dr = 0$ since the energy density must be an analytic function of x, y, and z at the origin. The outer edge of the star is reached, by definition, at the point where the pressure vanishes: $P(R) = 0$.

For the (massless, zero temperature) degenerate electron gas considered above we can solve explicitly for the equation of state:

$$P = \frac{\mu_e^4}{12\pi^2} = \frac{1}{12\pi^2}\left(\frac{3\pi^2 Y_p}{m_N}\right)^{4/3}\rho^{4/3}. \tag{1.9}$$

This equation of state belongs to the class of "polytropes" for which the general form is $P = K\rho^\gamma$. Polytropes are unique in that the equation of gravitational structure, Eq. 1.8, can be solved analytically in terms of Lane-Emden functions of index $1/(\gamma - 1)$. Here we will simply quote the surprising result[1] for a polytrope with $\gamma = 4/3$. In this special case, and with K taken as the coefficient of $\rho^{4/3}$ in Equation 1.9, the total mass as a function of the central density $\rho(0)$ is given by:

$$M = 5.87\, Y_p^2\, M_\odot. \tag{1.10}$$

That is, the total mass of a $\gamma = 4/3$ polytrope is independent of the central density: addition of material to the surface of such a star causes the star to contract such that the added mass energy is just cancelled by the increased gravitational binding energy. Plugging in our earlier value $Y_p \approx 26/56$ gives a value $1.3M_\odot$ for the mass in Eq. 1.10.

What does this mean for the stability of the iron core of our supermassive star? Recall our assumption that the electron mass could be neglected, i.e., that the electron gas was ultra-relativistic. In fact, had we included finite-m_e corrections, we would find that the total mass of the core would grow monotonically with increasing central density, reaching the limit of Eq. 1.10 as an asymptote. For mass greater than this limit — that is, when the mass of the iron core exceeds $1.3M_\odot$ — the degeneracy pressure of electrons becomes insufficient to hold the star up under gravitational forces and it therefore becomes unstable to collapse.

---

[1] See Weinberg's book [1] for further details.

A few caveats should be mentioned before describing the subsequent collapse. In addition to treating the electron gas as ultra-relativistic, the limiting mass above (discovered originally by Chandrasekhar [2] and hence denoted the "Chandrasekhar mass") was derived under the assumption that the pressure went to zero at the edge of the iron core. In a real star, however, there is a tremendous amount of material resting on top of the core; hence, the actual pressure here will be somewhat greater than zero, and the actual maximum core mass will be somewhat smaller than the result of Eq. 1.10. On the other hand, we have treated the electron gas at zero temperature; in actual stars, the temperature of the iron core is of order $T \approx .5MeV$. The extra contribution to the pressure from thermal effects helps to hold the star up, thus tending to increase the maximum mass from the limit quoted above. The lesson is that there *is* an absolute upper limit to the mass of the iron core, but that the specific number $M_{Chandra} = 1.3M_{\odot}$ is only accurate to within about $\pm 20\%$.

When the maximum core mass $M_{Chandra}$ is exceeded in a real star, the core collapses under its own weight, and all the material above begins to fall in toward the center. As the core begins to compress, electrons undergo weak reactions with protons in the nuclei according to

$$e^- + p \rightleftharpoons n + \nu_e. \tag{1.11}$$

That this process must begin to occur can be understood from the weak interaction equilibrium condition

$$\mu_e + \mu_p = \mu_n + \mu_{\nu_e} \tag{1.12}$$

where μ_i denotes the chemical potential for species i. As matter is compressed during the collapse, μ_e increases as $(n_e)^{1/3}$ while μ_p and μ_n remain initially unchanged. This pushes reaction 1.11 to the right, with the resulting electron neutrinos being simply radiated away during this early stage, as the probability for a neutrino to scatter on its way out of the core is quite small. The total lepton fraction in the core, initially equal to $Y_e = Y_p \approx 26/56 = .46$ drops to about $.35 \sim .40$ before the neutrino scattering rates (which rise steeply with temperature and density) become sufficiently fast that neutrinos get trapped in the dense matter [3]. This occurs when the total energy density reaches about $10^{12} g/cm^3$ which corresponds to about 1% of nuclear saturation density, n_0.

The early decrease in the electron fraction implies, referring back to Eq. 1.10, that once the collapse begins, the maximum mass begins to shrink. Hence, the more the star collapses, the more unstable it becomes, and the collapse accelerates extremely rapidly, typically at half or more of the free-fall rate corresponding to no supporting pressure at all. Equivalently, one can simply observe that electron capture reduces the effectiveness of the dominant contribution to the pressure, namely, electron degeneracy pressure. Because the local speed of sound exceeds the infall speeds, pressure variations are able to equilibrate as the core continues to collapse. It thus collapses as a (homologous) unit, retaining its $\gamma = 4/3$ polytrope density profile. This accelerating collapse continues until the total baryon number density, now dominated by neutrons, reaches a few times nuclear saturation density, $n_0 = 0.16 fm^{-3}$.

At this point, the hard-core repulsive nucleon-nucleon interactions cause an enormous and sudden increase in the material's stiffness. ($K = 9 m_N dP/d\rho \approx 220 MeV$ at nuclear matter density.) The matter falling onto the core bounces from this stiff material as if from a brick wall, sending pressure waves back up through the still-infalling material above. These pressure waves slow down as they propagate outward, due to the fact that the speed of sound decreases with decreasing density. The pressure waves pile up at the sonic point (where $v_{sound} = v_{infall}$) forming a shockwave, which is subsequently launched upward into the infalling material as the homologous core completes its bounce.

As the shockwave propagates outward, it heats up the material falling through it by dissociating heavy nuclei into constituent nucleons and α-particles. Due to these energetic losses, the shockwave stalls about $0.01 - 0.1\,sec$ after bounce at a radius of $200 - 300\,km$, forming an accretion shock which continues to melt the nuclei falling through it. This initial stalling of the shockwave indicates the failure of the so-called "prompt" supernova explosion mechanism.

The delayed explosion mechanism, however, is believed to revive the shock, allowing it to continue propagating outward eventually to tear off the star's mantle in a supernova explosion. This delayed mechanism depends on neutrino (and anti-neutrino) capture on the free nucleons which now exist in the matter below the accretion shock. The charged current

reactions

$$n + \nu_e \rightarrow p + e^- \tag{1.13}$$

$$p + \bar{\nu_e} \rightarrow n + e^+ \tag{1.14}$$

deposit thermal energy to the matter behind the shock, which increases its material pressure and helps the shock to begin moving outward. This mechanism depends sensitively on several details. In addition to absorbing energy by capturing neutrinos from the core, the hot matter behind the shock may also radiate energy in the form of neutrinos and anti-neutrinos. One thus defines the gain radius as the point at which these two processes exactly cancel — that is, the point at which radiative neutrino loss rates just equal the neutrino energy deposition rates. Inside of the gain radius, there is net cooling due to neutrino emission, while outside of the gain radius, there is net heating due to neutrino capture [4]. If the shockwave stalls too far above the gain radius, neutrino reheating of the material behind the shock is too weak, and the shock will never be revived; if the shock stalls inside of the gain radius, there is again no hope for it, as its energy is radiated away by neutrinos.

It is worth noting that the total change in gravitational binding energy of the original near-Chandrasekhar mass core is of order

$$\Delta U \sim \frac{GM_{core}^2}{R_{NS}} \sim \text{few} \cdot 10^{53}\,\text{erg} \tag{1.15}$$

where $R_{NS} \sim 10\,km$ is a typical neutron star radius, *i.e.*, the final core radius at the end of collapse. (This number will be explained below.) Less than 1% of this energy is converted into the outward kinetic energy of the exploded matter, while the rest is radiated away by the neutrinos (and anti-neutrinos) which are initially trapped in the core. So in principle there is more-than-sufficient energy available to revive the shockwave and produce supernova explosions. Detailed numerical simulations of the core-collapse process, however, have had long-running difficulties reproducing exploding stars. This is due to the extreme complexity of the simulations, which must include realistic (multi-dimensional, spectral) neutrino transport physics alongside the detailed hydrodynamics, as well as to the delicate

sensitivity of the delayed explosion mechanism. Accurate simulations are only just becoming feasible with current computer technology [5].

Nature, however, does not suffer from the same paucity of computing resources, and seems to have no difficulty producing successful core-collapse supernova explosions. We will say more about the direct observational evidence for supernovae (and, consequently, their products) in Section 1.3. For now, let us turn to a brief overview of the structure and properties of supernova remnants: neutron stars.

1.2 Basic Neutron Star Structure

As a result of the collapse process outlined above, the supernova leaves behind a remnant which is approximately the mass of the original iron core (*i.e.*, close to the Chandrasekhar mass limit of $\sim 1.3 M_\odot$), has an average density near nuclear saturation density, and is composed mostly of neutrons. We will refer to such an object as a neutron star (NS), though it should be noted at the outset that our picture of the detailed composition and structure will be revised substantially as we progress.

Let us begin our discussion by following the strategy used above, namely: calculate the equation of state (for pure neutron matter this time) and then solve the hydro-dynamic equations in order to understand the allowed ranges of mass and radius for stable stars. (Note that the assumption of pure neutron matter is unrealistic; real neutron star matter will be in β-equilibrium and will therefore contain a small $\sim 10-20\%$ proton component. A more detailed treatment will be given subsequently; here we are only interested in identifying the basic concepts.) Assuming for the moment that it is appropriate to treat the neutrons as a non-interacting Fermi gas, we may again relate the number density, energy density, and pressure to the Fermi momentum. Here it is crucial to retain the neutron mass, since the Fermi momentum will by no means be large compared to $1GeV$. The number density is given as before by

$$n_n = 2\int_0^{k_F} \frac{d^3k}{(2\pi)^3} = \frac{k_F^3}{3\pi^2} \tag{1.16}$$

where again the factor of two comes from counting the independent spin states. The energy density involves the same integral with an additional factor of $E(k) = \sqrt{k^2 + m_N^2}$ in the

integrand:

$$\begin{aligned}\rho_n &= \int_0^{k_F} \frac{d^3k}{(2\pi)^3} E(k) \\ &= \frac{1}{8\pi^2}\left(m_N^2 k_F \mu_n + 2k_F^3 \mu_n + m_N^4 \ln\frac{m_N}{k_F + \mu_n}\right) \end{aligned} \tag{1.17}$$

where $\mu_n = \sqrt{k_F^2 + m_N^2}$ is the neutron Fermi energy. The pressure is then given as before by $P_n = \mu_n n_n - \rho_n$:

$$P_n = \frac{1}{12\pi^2} k_F^3 \mu_n - \frac{1}{8\pi^2}\left(m_N^2 k_F \mu_n + m_N^4 \ln\frac{m_N}{k_F + \mu_n}\right). \tag{1.18}$$

In principle, one can eliminate the variable k_F from Equations 1.17 and 1.18 in order to write the equation of state $P_n(\rho_n)$. Unlike the case of a relativistic Fermi gas, however, we cannot put this equation in any useful closed form. But this is not really necessary anyway; all we require for solution of the gravitational structure equations is a definite relation among n_n, ρ_n, and P_n, which we clearly have.

Another complication which arises compared to the earlier example is the need to use a fully general-relativistic version of the gravitational hydro-static equilibrium equation. This equation [6] was originally written down by Tolmann, Oppenheimer, and Volkoff (TOV) and can be put in an especially clear form in which the GR corrections to the Newtonian version can be seen explicitly:

$$\frac{dP(r)}{dr} = -\frac{GM(r)\rho(r)}{r^2}\left(1 + \frac{P(r)}{\rho(r)}\right)\left(1 + \frac{4\pi r^3 P(r)}{M(r)}\right)\left(1 - \frac{2GM(r)}{r}\right)^{-1} \tag{1.19}$$

where (somewhat miraculously) $M(r) = \int_0^r 4\pi r'^2 dr' \rho(r')$ just as before. The apparent miracle is that the expected relativistic length-contraction does not appear explicitly in the volume integration, and the relativistic time-dilation factor does not appear to dilate the energy density we are integrating over. The "miracle" is actually a cancellation between these two effects, a cancellation which only occurs for gravitationally stable matter configurations satisfying Equation 1.19. As Glendenning writes, this lovely cancellation would not occur for an *arbitrary* mass distribution $\rho(r)$ — however, "there are no arbitrary distributions in gravity." [3]

As before, we solve the equations of gravitational structure for a given equation of state by integrating out from the center of the star ($r = 0$) where we assume some initial energy density $\rho(0)$. By definition, we have reached the edge of the star when the pressure drops to zero: $P(R) = 0$. Thus, we expect a one-parameter family of allowed stars (each with a different central density) for any proposed equation of state.

Of particular interest is the free neutron gas equation of state developed above. Solving the TOV equation numerically for this equation of state shows that, as in the case of the relativistic electron gas equation of state considered previously, there is a maximum mass for stable configurations. Numerically, the maximum mass is achieved for a star of mass $M_{max} = 0.7M_{\odot}$ and radius $R = 9.6km$ [3]. Any pure neutron ideal-gas star with $M > M_{max}$ will be unstable against continued gravitational collapse.

Indeed, in such a case, the star will collapse "completely" and form a black hole — no sudden increase in the pressure at higher densities can prevent this collapse. (Such an increase *did*, recall, prevent the complete collapse of the supernova progenitor's iron core.) The Schwartzchild radius $R_{sch} = 2GM$ for a neutron star of mass $0.7M_{\odot}$ is $2.1km$, so only a small compression is required to bring the entire star within its own gravitational event horizon, thus signalling the inevitable formation of a black hole. In addition, inspection of Eq. 1.19 shows that, in the general relativistic equation for stellar structure, pressure enters alongside energy density in contributing to the inward gravitational force on a shell of matter. This implies that no equation of state — no matter how stiff it becomes at very high density — can prevent the neutron star from ultimately collapsing to a black hole once the maximum mass is exceeded.

At this point, one might worry that neutron stars should not be found in nature, since the Chandrasekhar mass of $\sim 1.3M_{\odot}$ seems to exceed the maximum neutron star mass of $0.7M_{\odot}$ we have just derived. This would seem to imply that black holes — and not neutron stars — will be produced as the final product of all core-collapse supernovae. However, we must recall that we assumed a non-interacting neutron gas in deriving this result for the maximum mass. A more realistic model (in particular, one which incorporates the hard-core repulsive interaction between nucleons) will provide a much stiffer equation of state and will thus raise the maximum mass to near or above the Chandresekhar mass. We will say

more about maximum masses for various equations of state when we discuss neutron star matter in more detail in the following chapter. Our present goal is only to give a qualitative picture of neutron star structure to set the stage for a discussion of observational methods and results.

Before going on, it is worth making one final point about neutron star maximum masses. We can place a hard upper limit on the maximum mass by requiring that the equation of state $P(\rho)$ satisfy the causality condition: $v^2_{sound} = dP/d\rho \leq c^2$. This states that the speed of soundwaves in matter cannot exceed the speed of light, which puts an absolute limit on the slope of $P(\rho)$. If we "pin" the equation of state to the known energy density of symmetric nuclear matter at saturation density (with zero pressure), we may then construct the stiffest possible equation of state by simply drawing a straight line with slope c^2 from this point. Solving numerically for the sequence of stable stars with this equation of state yields a (limiting) maximum mass of $M_{max} \leq 3.2 M_{\odot}$. [3]

Lest the reader be left with a worry that the true equation of state of neutron star matter be too soft to allow their production in core collapse supernovae, let us turn to consider the direct observational evidence for the existence and properties of neutron stars in nature.

1.3 Observational Data

The first historical supernova to be recorded was observed by Chinese astronomers in the year 1054. Legendary astronomer Tycho Brahe also recorded his observations of a supernova in the 16th century. Since then, many supernovae have been observed and studied, most spectacularly the event in the Large Magellanic Cloud (a nearby satellite to our own galaxy) which occurred in 1987. Several large neutrino detectors operating at the time were able to isolate 19 detections as due to the neutrino pulse from SN-1987A [7, 8].

Given the above outline of the formation of neutron stars in core collapse supernovae, these observations might be taken as indirect evidence for the existence of neutron stars in nature. The first direct evidence came in 1967 with the discovery by Bell & Hewish [9] of the first radio pulsar: an apparently pointlike emitter of extremely regular pulses of electromagnetic radiation. Shortly after the initial discovery by Bell & Hewish, another

pulsar was discovered within the Crab nebula — interestingly, this was later identified with the supernova observed in 1054. Since the 1970's, hundreds of additional pulsars have been discovered, with pulse-rates ranging from several milliseconds to of order seconds and with pulse-spectra ranging from the radio to the gamma-ray part of the spectrum.

Pulsars are believed to be neutron stars with large frozen-in magnetic fields. If the angular momentum and magnetic moment vectors of such an object are non-parallel, a cone of electromagnetic radiation will be swept out as the star rotates. A distant observer who happens to lie on this cone can then be expected to see a regular pulsation of radiation. The pulse rate is the simplest property which can be measured; these rates are sufficiently stable, and have been measured so precisely, that in several cases the limiting systematic uncertainties are due to the imprecision of terrestrial clocks.

What can be learned about the emitting objects from pulse rates? The Crab and Vela pulsars, two of the earliest-discovered examples, are observed to have pulse periods of $33\,ms$ and $89\,ms$ respectively. Assuming this frequency (= 1/period) can be identified with the spin frequency of the emitting object, the surface of the object would be experiencing an outward centrifugal force of order

$$F_{cent} \sim R\,\omega^2\,\delta m \tag{1.20}$$

where δm is the mass of the outer crust. The inward gravitational force on this same outer crust is of order

$$F_{grav} \sim \frac{G\,M(R)\,\delta m}{R^2}. \tag{1.21}$$

Stability requires $F_{grav} > F_{cent}$ which immediately implies $R < \left(GM(R)/\omega^2\right)^{1/3}$. Plugging in a typical Chandrasekhar mass for $M(R)$ and the observed tens-of-ms frequencies mentioned above yields $R < 10^2 km$. This limit rules out the possibility that pulsars are, say, spinning white dwarfs, thus leaving neutron stars as the only reasonable possibility. (No known equation of state allows for stable stars between the white dwarf and neutron star branches.)

Recently, extremely fast pulsars have been discovered with pulse periods on the order of $1\,ms$. The first such pulsar, with $P = 1.56 ms$, was identified in the 1980's by Backer et

al [10]. For such a rapidly rotating star to avoid breaking up under centrifugal forces, we again must have

$$\zeta^2 \frac{G\,\delta m\,M}{R^2} > \delta m\,\Omega^2\,R \tag{1.22}$$

where here $\zeta \sim 0.6$ incorporates the GR corrections to Newtonian gravity. Rewriting the above as an inequality on the average neutron star density $\bar{\rho} = M/(4\pi R^3/3)$ gives a limit [3]

$$\bar{\rho} \gtrsim 3.6 \cdot 10^{14} g/cm^3 \tag{1.23}$$

for a rotational period $P = 1ms$. This value is about 50% higher than nuclear matter density $\rho_0 \sim m_N n_0$, implying that the neutron star central density is several times ρ_0 since the density must decrease monotonically from the center. This same limit coming from centrifugal break-up can also be used to put constraints on the equation of state by ruling out those which tend to predict stars with too-large radii.

In 1974 Hulse and Taylor [11] discovered the first binary pulsar, that is, a pulsar orbiting a companion star in a binary system. Since then, a number of additional neutron stars have been found in binaries, including several in which (like the Hulse-Taylor binary system) both objects appear to be neutron stars. Much can be learned about the masses of neutron stars by careful observations of pulse timing in such binary systems.

In particular, several uniquely general relativistic properties of neutron star binaries can be measured [12]. These GR corrections to a purely Newtonian orbit (or "PK properties" as they are often called, PK standing for Post-Keplerian) include:

- Advance of periastron, like that observed in the planet Mercury (representing, at the time, an important piece of evidence for GR) but with typically larger amplitudes in neutron star binaries. For example, the periastron precession rate in the Hulse-Taylor system is some 4.2 degrees per year, compared to the 43 seconds of arc per century observed for Mercury [3].

- The (combined) effects of gravitational redshift (and transverse Doppler shift) produced as the pulse radiation climbs out of the binary system's gravitational potential well.

- The shape and amplitude of the Shapiro delay curve, due to the increased distance traveled by a gravitationally-lensed light ray as the emitter passes behind its companion.

- The rate of decay of the orbital period as the binary system loses energy to gravitational radiation.

Given measured values for the Keplerian parameters of the orbit (the orbital period, eccentricity, time and direction of periastron, and orientation of orbital plane with respect to our line of sight) knowledge of any two of the PK parameters will uniquely determine the individual masses M_1 and M_2 of the two binary partners. (See Ref. [12] for details.) Thus, careful observations of the orbital properties of binary systems allows us to infer the masses of actual neutron stars.

It is also possible to acquire independent information about the mass of a pulsar's binary partner, for example through optical observations of white dwarf companions. Since the equation of state of white dwarfs is better understood than that of neutron stars, measurement of the radius can allow one to reliably infer the white dwarf mass (and hence also the pulsar mass if at least one PK property is measured). The white dwarf radius can be calculated by measuring the total flux F, fitting the spectrum to a thermal distribution to infer $T_{surface}$, and using

$$F = \sigma T_{surface}^4 R^2/d^2 \tag{1.24}$$

which assumes that the distance d from Earth to the binary system is known. (σ here is the Stefan-Boltzmann radiation constant.) Alternatively, it is sometimes possible to fit a model atmosphere to the observed spectrum (and total luminosity) of the companion, allowing one to infer the surface gravitational potential (and hence M/R). Finally, we will mention that if the pulsar happens to orbit a main-sequence star, the mass can be estimated from its brightness and color characteristics.

The most precisely measured neutron star mass is that of the pulsar in the Hulse-Taylor binary. Observations stretching over several decades have led to precise measurements of three different PK parameters [12]. From these, the pulsar mass can be fit at the 90%

confidence level as $M = 1.4411 \pm .0007 M_\odot$, while the non-pulsing companion (believed also to be a neutron star) has a mass given by $1.3874 \pm .0007 M_\odot$. Mass measurements of several other radio pulsars have been performed by similar techniques (though with typically far greater uncertainties in the masses). The masses generally clump in the range $M \sim 1.35 \pm .1 M_\odot$. Since the gravitational binding energy ($\sim GM^2/R$) of a neutron star is typically about 10% of the mass M, this implies that most neutron stars are formed from about $1.5 M_\odot$ of pre-collapse matter. This number is almost exactly the Chandrasekhar mass discussed previously, leading to speculation that the observed uniformity in measured neutron star masses is due to their production mechanism, rather than a small maximum mass. That is, the fact that neutron stars with $M > 1.5 M_\odot$ are not typically observed, does not necessarily imply that the maximum neutron star mass is of this order. Indeed, as we will see shortly, there is some preliminary evidence for the existence of somewhat anomalously massive $M \sim 2.0 M_\odot$ neutron stars. Please see Fig. 1.3 for a collection of neutron star masses inferred from observations via the techniques mentioned above.

Another specific neutron star which deserves mention is RX-J1856-35-3754, an isolated neutron star quite close to our solar system. Because of its proximity, the distance d can be measured by parallax, i.e., by observing the shift in the apparent location of the object relative to the "fixed stars" as the earth moves from one side of its yearly orbit to the other. Modeling of the heavy-element atmosphere surrounding the star's surface [13] allows one to infer the gravitational redshift $z + 1 = (1 - 2GM/R)^{-1/2}$ experienced by radiation from the surface. Additionally, the observed total flux F (whose spectrum is roughly consistent with a $T = 57eV$ blackbody) can be used to infer the surface radius through Equation 1.24. Earlier measurements of the parallax distance seemed to indicate $d \sim 60pc$ ($1pc = 3.26\ c{\cdot}yr$), implying a radius $R \sim 5 - 8km$ and mass $M \sim 0.6 - 1.2 M_\odot$ [13]. These numbers (in particular the exceptionally small radius) are inconsistent with any reasonable neutron star matter equation of state. A recently revised parallax measurement, however, suggests the value $d = 117 \pm 12pc$. This implies $R = 11.4 \pm 2.0km$ and $M = 1.7 \pm 0.4 M_\odot$ [14], values that are much more in line with the various equations of state to be discussed in more detail in Chapter 2.

Before wrapping up our discussion of mass and radius measurements, it is worth men-

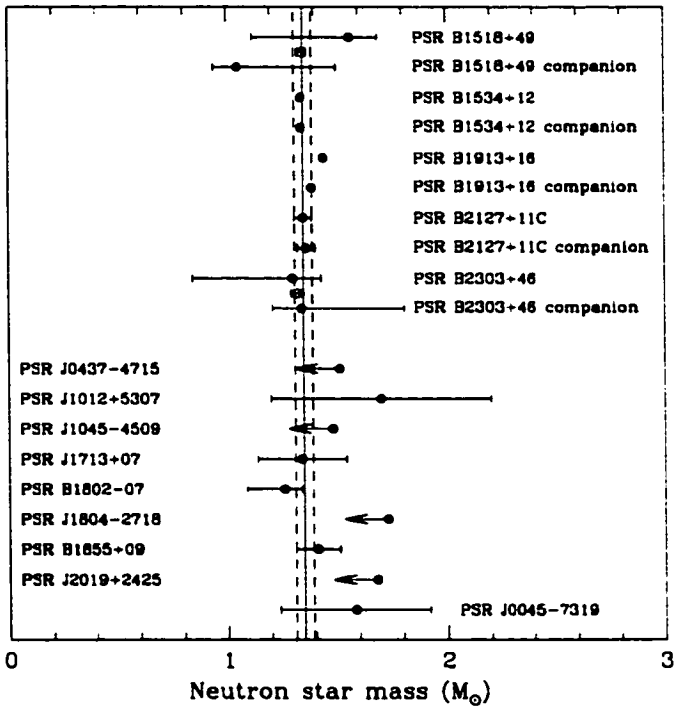

Figure 1.1: Neutron star masses from observations of radio pulsar systems. Error bars indicate central 68% confidence limits, except upper limits are one-sided 95% confidence limits. The vertical lines are drawn at a mass $1.35 \pm 0.04 M_{\odot}$. Taken from Ref. [12].

tioning a few additional means of study. One promising method that is still in its early stages is the possibility of resolving discrete absorption lines from the neutron star surface X-ray spectra [15]. In principle, this would allow a much less model-dependent measurement of the gravitational red-shift (and hence M/R) as compared to the assumption-laden atmospheric modelling mentioned above. However, the first observations using XMM and Chandra have failed to detect any clearly identifiable line features [16]. As resolution improves in the future, however, this will undoubtedly become an exciting method of obtaining detailed information about neutron star masses and radii.

Another intriguing bit of recent progress is the observation of kHz frequency Quasi-Periodic Oscillations (QPOs) in the X-ray emission of neutron stars with low-mass companions. The QPOs are believed to be produced by matter that is accreting onto the neutron star from the companion. The accreting matter orbits the star just above its surface with a (Keplerian) orbital frequency given by

$$\nu_{QPO} = \frac{1}{2\pi}\sqrt{GM/R^3_{orbit}}. \tag{1.25}$$

The observed oscillations in the brightness of the radiation are thought to be caused by the beat frequency between the orbit of the accreting matter and the spin frequency of the underlying neutron star surface: $\nu_{beat} = \nu_{QPO} - \nu_{spin}$. In a few cases, the accretion can be tracked to the innermost stable orbit

$$R_{min} = 6GM = 3R_{Schwartzchild} \tag{1.26}$$

which, for an assumed slowly rotating underlying star, implies

$$M \sim 2.2M_{\odot}\left(\frac{\nu_{QPO}}{kHz}\right)^{-1}. \tag{1.27}$$

Several QPOs with frequencies very near 1 kHz [17, 18, 19, 20, 21] then imply neutron star masses near $2.2M_{\odot}$, though uncertainties may be as high as $.4-.5M_{\odot}$. Nevertheless, neutron star masses as high as $1.7 - 1.8M_{\odot}$ would be very interesting in constraining proposed equations of state; masses as high as $2.2 - 2.5M_{\odot}$ would be devastating for many such proposals.

Clearly quite a bit is now known about real neutron star masses and radii, and there is much room for optimism about future measurements. Ideally, one would like simultaneous,

precise measurement of both M and R for a number of different neutron stars. The resulting $M(R)$ curve would then *uniquely* determine the equation of state $P(\rho)$ of dense nuclear matter, at least up to some highest density.

Let us then briefly review what else (beyond masses and radii) is known empirically about neutron stars. One interesting phenomenon is the so-called pulsar "glitches". Returning to the basic picture of a pulsar as a rotating neutron star with an off-axis frozen-in magnetic moment, we immediately infer that the pulse rate must slowly decrease over time as electromagnetic energy is radiated away:

$$\frac{d}{dt}\left(\frac{1}{2}I\Omega^2\right) = \frac{2}{3}R^6B^2\Omega^4\sin^2\alpha \tag{1.28}$$

where I is the rotational inertia, Ω the spin frequency, B the magnetic field strength at the surface R, and α the angle between the angular momentum and magnetic moment vectors [3]. Solving this equation for B allows one to infer neutron star magnetic field strengths from observed spin-down rates $\dot{\Omega}$. Results are typically of order 10^{12} *Gauss*, which is the size one would expect based on magnetic flux conservation during the core collapse supernova event assuming the progenitor star contained fields of order 10^2 *Gauss*.

Interestingly, the slow decrease of Ω in observed pulsars is not completely smooth — occasionally, between long periods of very constant $\dot{\Omega} < 0$, there is an extremely sudden increase in Ω. Such a phenomenon is referred to as a glitch. Glitches are probably due to sudden, structural rearrangements of the matter in a neutron star, resulting in a small but nearly instantaneous decrease in the moment of inertia I. Conservation of angular momentum then requires the spin frequency Ω to increase equally suddenly. Clearly such a process would argue for the existence of some solid, crystalline component in the neutron star. As we will see in the next chapter, neutron star matter near the outer edge of the star is expected to form just such a solid crust. Glitches are then likely explained by the cracking and subsequent reforming of this solid crust as the neutron star spins down and reduces its equatorial bulge. As we will see, however, there is also some evidence to suggest that glitches might involve similar crystalline phases in neutron star cores or perhaps even superfluid vortices, if a superfluid phase is realized in neutron star interiors.

As a final topic, let us consider the cooling of neutron stars. The initial temperatures of

proto-neutron stars (PNSs) produced in core collapse supernova is of order tens of MeV. After a period of order a few minutes, the PNS will have cooled to less than an MeV. The most obvious candidate cooling mechanism for the next several hundred thousand years is neutrino emission via the Urca processes

$$n \rightarrow p + e^- + \bar{\nu}_e \tag{1.29}$$

and

$$p + e^- \rightarrow n + \nu_e. \tag{1.30}$$

(The same processes with e's replaced by μ's may also occur.) Repeating the two reactions again and again results, obviously, in no change to the composition of matter except that energy is radiated away by neutrino-antineutrino pairs. However, momentum conservation in these processes requires that the Fermi momenta for neutrons, protons, and electrons satisfy a triangle inequality: $k_F^n < k_F^p + k_F^e$. If this is not satisfied, the final neutron state in the second reaction above will be Pauli blocked, suppressing the reaction.

If the direct Urca processes above are suppressed by Pauli blocking, the following modified Urca processes may still occur:

$$N + n \rightarrow N + p + e^- + \bar{\nu}_e \tag{1.31}$$

and

$$N + p + e^- \rightarrow N + n + \nu_e \tag{1.32}$$

where here N is a spectator neutron or proton that allows energy and momentum to be conserved. It is expected that these two scenarios (direct Urca cooling vs. modified Urca cooling) will result in distinguishable cooling rates which may in principle be useful in determining the composition of bulk neutron star matter. The inequality above, for instance, obviously puts a constraint on the proton to neutron density ratio which, as we will see in Chapter 2, may be quite different for different proposed equations of state [16].

It is not likely that the neutrinos from this cooling epoch will ever be detected directly, though obviously one can still infer interior temperatures from standard optical measurements of the surface radiation if one assumes the star is in thermal equilibrium. Such

observations may be useful in constraining equations of state when combined with knowledge of the age of the neutron star; this can be estimated in several ways, the simplest being simply to use the so-called "dipole age" $\tau \sim \Omega/\dot{\Omega}$ equivalent to the time-scale over which the spin rate Ω changes appreciably due to electromagnetic radiation. At later times in the cooling history, weak interactions involving neutrino emission become slow compared to electromagnetic radiation, and the star spends a near-eternity slowly cooling down by emitting thermal photons.

Possible superfluid phases in neutron star interiors (mentioned above in the context of glitches and which will be discussed in the subsequent chapter) may, if realized in real neutron stars, dramatically reduce neutrino emissivities (and hence cooling rates) compared to the "standard" cooling scenarios outlined above. The suppression would be due to the pairing of neutrons near the (neutron) Fermi surface, leaving no quasi-particle excitations of energy less than the pairing energy (or "gap") Δ. Consequently, cooling rates could be suppressed by a factor of order $e^{-\Delta/T}$. Again, future observations of NS temperature-age correlations may thus help in constraining models of neutron star matter.

We will close this discussion by returning to our starting point, namely core collapse supernovae. Several neutrino detectors of unprecedented size and fidelity are currently online around the world (most notably SNO in Canada and Super-Kamiokande in Japan) studying various aspects of neutrino astrophysics. If a supernova were to occur in our galaxy (or close by, as was the case with SN-1987A) we could expect many thousands of neutrinos to be detected. A tremendous amount of information could thereby be learned about (P)NS formation and structure, for example:

- The total electron neutrino number (that is, $n_{\nu_e} - n_{\bar{\nu}_e}$) emitted from a core collapse supernova may allow us to infer the lepton fraction of the remaining material, thus possibly signalling or ruling out the presence of certain exotic types of matter which contain zero (or, at any rate, less than "normal") lepton density. Various types of superconducting quark matter, for example, achieve charge neutrality without the help of electrons, so the total electron neutrino luminosity may be 20-30% higher if this kind of matter is formed in the PNS core. Additionally, a precise measurement

of the total lepton number emitted could help constrain the nuclear symmetry energy at high density; such a measurement would be quite difficult, however, as it involves the difference of two large numbers.

- The energy spectra of the emitted neutrinos contains information about the temperatures achieved in the PNS, knowledge of which would help us better understand the complex core collapse process.

- Relative energies among neutrinos of different flavors could help constrain models of neutrino mixing and neutrino masses. Alternatively, independent knowledge of neutrino mixing (which is being slowly honed in on already) would allow us to infer from observed energies something about the density profiles encountered by neutrinos on their way out of the PNS core.

- Neutrino light-curves will give an indirect measure of neutrino scattering processes within the PNS. Some models of neutron star matter, for example, predict complicated crystal structure of droplets of new exotic phases within the core. Such droplets may significantly reduce neutrino scattering mean free paths and hence "stretch" light curves out by a factor of order $10 - 100$ compared to the standard case.

- Observation of the early cooling rate of the newly-formed neutron star may help us understand the composition and structure of NS matter in the ways described above.

- Should a pulsar be produced by our hypothetical galactic supernova, observation of its spin history $\Omega(t)$ could yield valuable information about not only the equation of state, but also the cause of timing irregularities like glitches.

For a variety of reasons, it is believed that core collapse supernovae occur at a rate of $1 - 3$ per century in our galaxy. Whether or not a nearby supernova occurs in the next decade, it will be an exciting time during which a tremendous amount is learned about the properties of compact stars and the nuclear physics which gives rise to them. But a nearby supernova, allowing us to witness the birth of a neutron star from the front row,

is an especially exciting possibility. In the following chapter, we will begin to explore in detail the composition of neutron star matter and thereby fill out the explanatory gaps in the possible future discoveries mentioned above.

Chapter 2

NEUTRON STAR MATTER

In the previous chapter we saw in outline how neutron stars are created in core collapse supernova explosions; we also saw that neutron stars are indeed found in nature and that quite a lot is known from observations about their masses, radii, and other properties. Yet the theoretical model used previously to discuss their structure (namely, a non-interacting Fermi gas of pure neutrons) was obviously quite crude. In this chapter we will present a far more detailed account of the physics of bulk neutron star matter.

We begin with a schematic cross-sectional picture of the expected structure of a neutron star, showing the structure of matter at various positions within the radial extent of the star. This diagram is shown in Fig. 2.1. In the following sections we will analyze the physics of the different regions from the outside in, beginning with the outer crust and working our way in toward the higher-density and possibly exotic matter expected to be present in the cores of neutron stars.

2.1 Neutron Star Crusts

As was mentioned previously, ^{56}Fe has the largest binding energy per nucleon of any nucleus. It therefore represents the absolute ground state of hadronic matter at zero temperature and zero pressure. As was also mentioned, the outer edge of a star is defined as the point at which the pressure drops to zero. Since typical late-time surface temperatures of neutron stars are small on the scale of nuclear physics (i.e., $T << MeV$), it follows that the outer edge of a neutron star consists of iron nuclei and electrons, not unlike the solid iron we are familiar with terrestrially. However, since typical neutron star surface temperatures are large compared to the scale of atomic ionization energies ($\sim eV$), the iron atoms in the outer crust are almost completely ionized, and the matter can be accurately described as a Coulomb (BCC) lattice of iron nuclei surrounded by a more-or-less homogeneous gas of

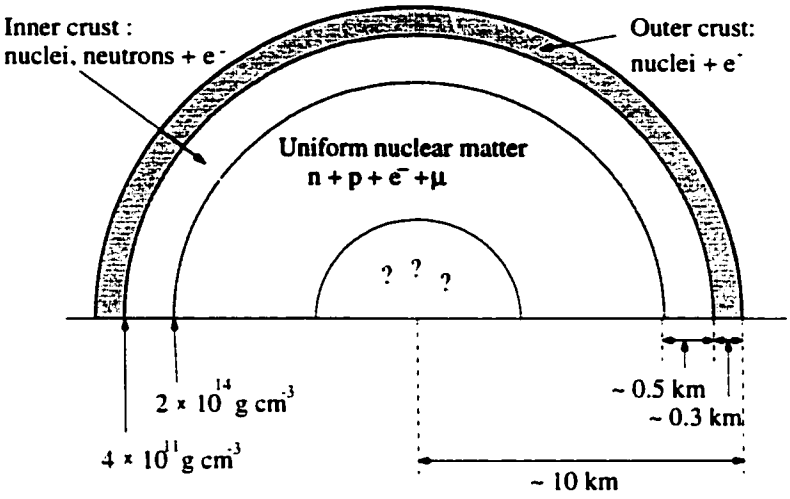

Figure 2.1: Schematic cross-section of a neutron star, taken from Ref. [16]. The outer region of the star consists of a solid "crust" of iron-like nuclei surrounded by a gas of degenerate electrons. The inner crust region begins when the density reaches the neutron drip point at which neutrons begin to leak out of nuclei. In this region, matter consists of positively charged nuclei surrounded by a gas of both electrons and neutrons. At higher densities, the nuclei merge together and matter becomes a homogeneous, electrically neutral fluid of neutrons, protons, and electrons (and muons beyond some critical density) in β-equilibrium. At the even higher densities reached only in the core of the star, new exotic states of matter may occur, e.g., deconfined quarks or a kaon condensate.

ionized electrons.

Of course, this description assumes that matter has had sufficient time to reach its ground state, i.e., that equilibration timescales are fast compared to whatever dynamical processes may occur to perturb the matter away from equilibrium. Accretion of hydrogen-rich matter from a companion star, for example, will obviously pollute the neutron star's surface with non-iron materials. Periodically, however, such materials will undergo explosive fusion reactions, restoring equilibrium. In any case, the description above applies to matter more than a few inches below the NS surface, even if the surface itself is polluted by accretion of matter rich in lighter elements.

The picture of NS matter as consisting of a lattice of iron nuclei surrounded by a gas of electrons, is valid up to a density of about $\rho \sim 10^7 g/cm^3$, reached a few hundred meters from the edge of the star. Near this point the pressure of the by-now relativistic degenerate electron gas begins to affect the equilibrium structure of the hadronic nuclei, altering somewhat the nature of the most-favored-nucleus. In particular, just as we saw in the supernova progenitor core, the increasing density of electrons tends to favor the reaction $e^- + p \rightarrow n + \nu_e$. As before, the neutrino mean free path is much greater than the size of the star so it simply escapes; the reaction tends to decrease the proton fraction of hadronic matter, pulling the nuclei from ^{56}Fe toward more neutron-rich configurations.

We may analyze this situation in more detail by considering the conditions for the minimization of the energy of matter; since baryon number is a conserved quantity, it is sufficient to minimize the energy per baryon

$$\frac{E}{N_B} = \frac{\epsilon}{n_B} = \frac{E(A,Z)}{A} + \frac{\epsilon_e}{n_e}\frac{Z}{A} \tag{2.1}$$

where $E(A,Z)$ is the energy of a nucleus with baryon/proton number A/Z. ϵ and n_B here represent the overall energy and baryon number densities respectively. The second term is the electron gas contribution to the energy per baryon; we have assumed electric charge neutrality, i.e., $n_e = n_p$. Minimizing this total energy with respect to strong-interaction allowed processes (which conserve the separate numbers of neutrons, protons, and electrons) is simply equivalent to minimizing the first term, the energy per baryon of the nucleus. For nuclei not too far from the valley of stability, the physics involved in this minimization is

well-understood and well-constrained by terrestrial experiments.

Weak interaction processes may alter the ratio of neutrons to protons, so minimization with respect to such processes involves a trade-off between the two terms above. Chemical equilibrium of the weak reaction $e^- + p \rightarrow n + \nu_e$ requires that no energy can be gained by allowing the reaction to proceed in either direction. This implies

$$\mu_p + \mu_e = \mu_n \tag{2.2}$$

where we have assumed that neutrinos simply leave the star so that $\mu_\nu = 0$. The chemical potentials are given by $\mu_i = \partial\epsilon/\partial n_i$. As stated previously, increasing μ_e at higher densities requires $\mu_n - \mu_p$ to increase, pushing nuclei toward increasing neutron richness. Thus minimization with respect to weak interaction processes fixes the proton fraction $x = Z/A = n_p/n_B$ at a given total baryon number n_B.

To understand the general trends, we can utilize the simple semi-empirical nuclear mass formula

$$\begin{aligned} E(A,Z) &= E_{bulk} + E_{surface} + E_{Coulomb} \\ &= A\epsilon(n_B,x) + 4\pi\sigma(n_B,x)R^2 + E_{Coulomb} \end{aligned} \tag{2.3}$$

where $\epsilon(n_B,x)$ is the bulk energy density of hadronic matter with total baryon density n_B and proton fraction x. $\sigma(n_B,x)$ is the surface tension between this bulk matter and the hadronic vacuum. The surface tension between two phases is calculated by assuming semi-infinite regions of bulk matter with a planar interface between them — the interface region is then allowed to adjust in a way that minimizes the total energy, equivalent to minimizing $\sigma = \int_{-\infty}^{\infty} \Delta\Omega(z)dz$ where $\Delta\Omega$ is the excess (free) energy density ($\Omega = \epsilon - \Sigma\mu_i n_i$) relative to the values in bulk matter at $z = \pm\infty$. The Coulomb energy term (for a spherically symmetric nucleus) is of order

$$E_{Coulomb} \sim \frac{3}{5}\frac{Z^2e^2}{R}. \tag{2.4}$$

an expression which ignores electromagnetic correlations among neighboring nuclei. We may approximate these correlations by using the Wigner-Seitz approach, in which matter is analyzed in terms of overall charge neutral cells consisting of a single nucleus surrounded

by a region of (negatively charged) electron gas. The Coulomb energy of such a cell is

$$\begin{aligned} E_{Coulomb} &= \frac{3}{5}\frac{Z^2e^2}{R} - \frac{9}{10}\frac{Z^2e^2}{R_{WS}} + \frac{3}{10}\frac{Z^2e^2R^2}{R_{WS}^3} \\ &= \frac{3}{5}\frac{Z^2e^2}{R}\left(1 - \frac{3}{2}\frac{R}{R_{WS}} + \frac{1}{2}\left(\frac{R}{R_{WS}}\right)^3\right) \end{aligned} \tag{2.5}$$

which is calculated by simply integrating the electrostatic Coulomb energy $\frac{\epsilon_0}{2}|\vec{E}|^2$ out to the Wigner-Seitz cell radius R_{WS}, defined as the radius at which the total enclosed electric charge vanishes. The order-$(R/R_{WS})^{(1,3)}$ corrections to Eq. 2.4 are the "lattice energy" contributions. Below the density at which neutron drip begins to occur, R/R_{WS} is typically $\sim .1$ or lower, so these corrections do not substantially affect the ground state composition of matter. They are crucial, however, in determining the favored geometrical configuration of the Coulomb lattice of nuclei.

It should be noted as well that the Wigner-Seitz approach itself [24] involves an approximation which is only strictly correct in the limit of small filling fraction $f \to 0$. This arises due to the fact that 3-Dimensional space cannot be filled with spheres or cylinders. (Space can be filled with the 1-D slab geometry, so the Wigner-Seitz approach is also exact in this special case.) Thus, the approximation introduces an error associated with the difference between the spherical or cylindrical unit cell and the polyhedral unit cells which will in fact be realized. In addition, the Wigner-Seitz approximation excludes the energy differences associated with different possible lattice arrangements (for example, body-centered-cubic vs. face-centered-cubic lattices in the case of droplets). See Ref. [25] for a discussion. In addition, the analysis here neglects possible shell effect contributions to the energy density [26].

As mentioned previously, minimization with respect to the strong interactions amounts to a minimization of $E(A,Z)$ with respect to A, holding the proton fraction $x = Z/A$ fixed. Writing the three terms in Eq. 2.3 in terms of x and A, we see that the first term is independent of A while the Surface and Coulomb contributions scale as $A^{2/3}$ and $A^{-1/3}$ respectively, neglecting the lattice energy contributions to $E_{Coulomb}$. Minimization with respect to A therefore immediately implies

$$E_{Surface} = 2E_{Coulomb} \tag{2.6}$$

which can be rewritten as the following equation for the energetically favored nucleon number A:

$$A \sim \frac{5}{2n_{in}e^2}\frac{\sigma(x)}{x^2\left(1-\frac{3}{2}(n_{in}/n_{overall})^{1/3}\right)} \tag{2.7}$$

where n_{in} is the density of nucleons within the nucleus, and $n_{overall}$ is the nucleon number density averaged across a Wigner-Seitz cell. Plugging in the value for σ coming from the semi-empirical mass formula [22] gives $A \sim 12/x^2$. This is consistent with iron-like nuclei for $x \lesssim 1/2$. At higher densities within the NS where x is reduced from $x \sim .5$ by virtue of the weak-interaction equilibrium condition Equation 2.2 ($x \sim .35$ at neutron drip) we see that larger nuclei with $A > 56$ are favored.

In addition to minimizing the total energy density with respect to the various allowed chemical processes, the system must also be in mechanical equilibrium, equivalent to minimizing the total energy with respect to changes in the volume of the nucleus. This requirement immediately implies that

$$P_{nuc} = P_e, \tag{2.8}$$

i.e., the hadronic matter in the nucleus and the electron gas surrounding it must be at the same pressure. (Note we have ignored the small corrections proportional to the surface tension σ which arise from differentiating $E_{Surface}$ and $E_{Coulomb}$ with respect to the nuclear volume V.) The nuclear pressure can be related to the compressibility term in the semi-empirical mass formula, while the pressure of the degenerate electron gas was calculated in Chapter 1. For matter below the neutron drip density, the mechanical equilibrium requirement yields nuclei with very close to nuclear saturation density — that is, nuclei in NS crusts below neutron drip are not substantially compressed relative to terrestrial, atomic nuclei.

To summarize, the proton fraction x decreases due to weak interaction equilibrium as the density of matter in the crust is increased. This leads to increasingly large ($A > 56$) neutron-rich ($x < 1/2$) nuclei. Such nuclei are less well understood since neutron-rich nuclei are unstable in the terrestrial environment — our understanding of neutron star matter in this regime therefore involves extrapolations of observed nuclear properties to nuclei with somewhat bizarre isospin. For small neutron excess ($1 - 2x$) and small pressure (P_{nuc}) we

may simply extrapolate from the semi-empirical mass formula

$$\epsilon(n,x) \sim b_{bulk} + b_{sym}(1-2x)^2 + \frac{1}{18}K(n-n_s)^2 + \cdots \tag{2.9}$$

where b_{sym} is the symmetry energy coefficient, K is the nuclear compressibility, and n_s is nuclear saturation density. However, this extrapolation becomes less and less reliable for nuclei farther and farther from the valley of stability. In addition, the shell structure of nuclei will modify the predictions of the naive semi-empirical mass formula treatment given here. In particular, nuclei with closed neutron and proton shells (magic numbers) will be greatly favored, though again our understanding of the shell structure of neutron-rich nuclei is not yet complete.

As the density continues to increase, eventually all the neutron states in the nuclear potential well (thinking for the moment in terms of a fixed, finite-depth potential well picture of the nuclear interactions) become filled. This occurs at a density of $\rho \sim 4.3 \cdot 10^{11} g/cm^3$, corresponding to a depth of a few hundred meters inside the NS [22]. At this point, neutrons are free to leak or "drip" out of nuclei, and the electron bath surrounding positively-charged nuclei will be supplemented with a free-neutron-gas component. It is far from obvious that the simple extrapolation of Eq. 2.9 can be relied on to describe either the extremely neutron-rich matter in nuclei near and beyond neutron drip, or the pure neutron matter hadronic component of the background gas. In practice, the best description of such matter comes from complicated many-body calculations of the bulk properties of neutron rich or pure neutron matter. We will describe these methods in the following section.

For now, let us simply mention the basic equilibrium conditions applicable to matter beyond neutron drip. We may generally describe the matter as before, in terms of two co-existing phases, I (referring to the positively-charged matter in nuclei) and II (referring to the electron-neutron gas surrounding the nuclei). Diffusive equilibrium between the two phases requires

$$\mu_i^I = \mu_i^{II} \tag{2.10}$$

where i runs over all species: neutrons, protons, and electrons. (Electrons are usually assumed to form a homogenous background through both phases, so this condition is satisfied trivially for them.) Similarly, equilibrium with respect to the weak interactions requires, as

before, that

$$\mu_e + \mu_p = \mu_n \tag{2.11}$$

where, given Equation 2.10, we have dropped the I vs. II labels on the chemical potentials. This implies that the total energy cannot be lowered by allowing weak interactions to change the relative composition of matter. Finally, we have as before the mechanical equilibrium constraint coming from minimizing the energy with respect to the size of nuclei:

$$P^I = P^{II} \tag{2.12}$$

as well as the requirement of overall electric charge neutrality

$$n_Q = n_p - n_e = 0 \tag{2.13}$$

where n_p and n_e are the values averaged across an entire Wigner-Seitz cell.

For the same physical reasons we saw operating below neutron drip, the continuing increase in density results in ground state nuclei with larger and larger A and smaller and smaller proton fraction x. This tends to decrease the amount of negatively-charged material surrounding a given nucleus needed to achieve overall electric charge neutrality within a Wigner-Seitz cell — that is, the ratio R/R_{WS} slowly increases to nearly unity with increasing density. As this occurs, adjacent nuclei are increasingly close to being in contact, and it becomes possible to lower the surface energy by allowing nuclei to merge into rods. Subsequently, at higher densities, rods merge to form planar slabs. Eventually, the matter ceases to be separated into two distinct phases — the nuclei dissolve and we are left with a homogenous, electrically neutral liquid of neutrons, electrons, and protons. This so-called liquid-gas phase transition occurs (not unexpectedly) near nuclear saturation density, or when $\rho \sim 2.4 \cdot 10^{14} g/cm^3$. Explicit calculations of the sort outlined above [22, 23] show that between neutron drip and the liquid-gas transition, the proton number Z of stable nuclei increases from about 40 to nearly 100, while the nucleon number A rises from about 120 at neutron drip to more than 500 at the phase transition.

One surprising aspect of the phase transition mentioned here is the appearance of a seeming continuum of geometrical structures from nuclei to rods to slabs (and back again, as the two phases "turn inside out" on their way to the homogenous liquid phase). We

will give a more detailed analysis of these geometrical structures in Section 2.3, as the same physics is likely to recur for any phase transition to exotic states of matter occurring in the dense cores of neutron stars. For now, let us conclude this section by showing that, as we come down in density from the uniform phase, an instability toward "proton clumping" develops just at the point where explicit calculations show that the ground state configuration of matter involves nuclei (or rods, slabs, etc.) surrounded by a negatively-charged electron/neutron gas. This stability analysis foreshadows a calculation performed in a later chapter in a different physical context.

Let us assume a homogenous phase consisting of neutrons, protons, and electrons, with number densities n_n, n_p, and n_e respectively. We then allow for small density inhomogeneities by introducing $n_n(\vec{r}) = n_n + \delta n_n(\vec{r})$, and likewise for the other particles. The total energy density of matter can then be written

$$\epsilon = \epsilon_0 + \epsilon_{Coulomb} + \epsilon_{curvature} \tag{2.14}$$

where ϵ_0 is the energy density of homogenous matter, $\epsilon_{Coulomb}$ is the contribution arising from possible charge separations (which occur if $\delta n_p(\vec{r}) \neq \delta n_e(\vec{r})$), and $\epsilon_{curvature}$ is the surface-energy-like contribution arising from gradient terms in the density-functional expression for ϵ. If we assume a harmonic perturbation $\delta n_p(\vec{r}) = A\cos(\vec{q}\cdot\vec{r})$ the deviation from the bulk energy density is given by

$$\epsilon - \epsilon_0 = \frac{1}{2}A^2 v(q) \tag{2.15}$$

where the effective interaction among protons is given by

$$v(q) = v_0 + \beta q^2 + \frac{4\pi e^2}{q^2 + k_D^2}. \tag{2.16}$$

Here $v_0 = \left(\frac{\partial \mu_p}{\partial n_p}\right)_{\mu_n, n_e}$, k_D is the electron Debye screening length, and β is a constant characterizing the energy cost of fluctuations in n_p relative to n_n. We are assuming that the density fluctuations are infinitesimal, and have therefore kept only those terms which are quadratic in the amplitude A; the first-order terms vanish if we assume that the fluctuations preserve the total baryon number and the total electric charge.

The function $v(q)$ is minimized for a specific wave number $q = Q$ given by

$$Q^2 = \left(\frac{4\pi e^2}{\beta}\right)^{1/2} - k_D^2. \tag{2.17}$$

and the value at the minimum is given by

$$v(Q) = v_0 + 2(4\pi e^2 \beta)^{1/2} - \beta k_D^2 \tag{2.18}$$

A numerical calculation [23] shows that an instability (i.e., a possible configuration having $v(Q) < 0$) appears when the density falls below $\rho \sim 3 \cdot 10^{14} g/cm^3$. The (half) wavelength of the unstable mode is about $Q/2 \sim 10 fm$ suggesting that the true ground state below this density will consist of geometrical structures of about this size, instead of the homogenous fluid. This is of course consistent with what we saw earlier, namely, that matter below this density exists in a charge-separated configuration consisting of positively-charged nuclei in a bath of electrons and neutrons. It is interesting, however, to see information about the ground state configuration (homogenous electrically neutral fluid vs. charge-separated mixed phase) fall out of a simple stability analysis.

2.2 Bulk Nuclear Matter

The outer km or so of a neutron star (consisting of matter up to a density $\rho \sim 10^{14} g/cm^3$) thus consists of positively-charged nuclei surrounded by a gas of neutrons and/or electrons. Above this density, matter is expected to consist of a homogenous, electrically-neutral, neutron-rich fluid of neutrons, protons, and electrons. This latter phase is believed to be present through the majority of the central regions of most neutron stars; a detailed understanding of its properties is therefore essential if we are to understand the NS masses and radii observed in nature.

In Chapter 1, we calculated the equation of state for non-interacting neutron matter. A slightly-improved version of this simplified model can be had by including the weak-interaction equilibrium constraint, Eq. 2.2. We then have a total baryon number density given by

$$n_B = \sum_{i=n,p} 2 \int_0^{k_F^i} \frac{d^3k}{(2\pi)^3} \tag{2.19}$$

and an energy density given by

$$\epsilon = \sum_{i=n,p,e} 2 \int_0^{k_F^i} \frac{d^3k}{(2\pi)^3} E_i(k) \tag{2.20}$$

where $E_i(k) = \sqrt{k^2 + m_i^2}$ is the energy of a particle of species i and momentum k. The Fermi momenta k_F^i satisfy $\mu_i = E_i(k_F^i)$ where μ_i is the chemical potential for species i. Electric charge neutrality requires the proton and electron number densities to be equal, i.e., $k_F^e = k_F^p$.

This analysis of the three-component substance subjected to two constraints (weak equilibrium and charge neutrality) allows us to understand qualitatively how the composition of matter changes as the density n_B is increased. Because it ignores interactions among the baryons, however, the energy density (and pressure) predicted by this model are completely unreliable. Interactions will of course also affect the naive predictions of composition: for example, a symmetry-energy-like term will tend to push the proton fraction x back toward 1/2 from the value predicted by the non-interacting Fermi gas analysis. Thus, a realistic analysis of extended nuclear matter like that found in neutron stars simply must include nucleon-nucleon interactions.

The (momentum space) nucleon-nucleon interaction potential at low momentum transfers is well-known from experimental scattering data. In the last 10 years, the scattering data for energies below about $300 MeV$ has been organized into a systematic database by the Nijmegen group [27]. These data have subsequently been fit to a number of specific phenomenological NN interaction forms, e.g., the Argonne v18 potential [28] which are based on a non-relativistic potential model (with different radial potential functions attached to various non-relativistic operators involving the spin, isospin, and angular momentum of the interacting nucleons), and the Bonn interactions [29] which are based on a relativistic meson-exchange picture of NN interactions. Given one of these modern potentials, the properties of bulk hadronic matter can be calculated using standard many-body physics techniques, which we will briefly describe.

For a given NN interaction V, the free-space interaction matrix for two-nucleon scattering

is derived from the Lippmann-Schwinger equation, which in the center of mass frame reads:

$$R(k,k',\omega) = V(k,k') + \int \frac{d^3q}{(2\pi)^3} V(k,q) \frac{1}{\omega - H_0} R(q,k',\omega) \tag{2.21}$$

where angular momentum, spin, and isospin indices have been suppressed. Here the operator H_0 represents the kinetic energy of the intermediate states, while ω is the total energy transfer of the scattering process. Equation 2.21 must be solved self-consistently for the interaction matrix; this is equivalent to summing over all possible numbers of potential interactions V between the nucleons, i.e., summing the so-called ladder diagrams.

In a nuclear medium (as opposed to free-space) we must include the effects of Pauli blocking of nucleonic intermediate states. This is accomplished in the Brueckner-Hartree approach by introducing the G-matrix given by:

$$G(k,k',\omega) = V(k,k') + \int \frac{d^3q}{(2\pi)^3} V(k,q) Q \frac{1}{\omega - QH_0Q} QG(q,k',\omega) \tag{2.22}$$

where Q is the Pauli operator which prevents scattering into occupied states. The G-matrix thus acts as an effective interaction between nucleons in the Fermi sea. As before, this equation automatically re-sums the ladder diagrams with two-particle intermediate states. The single-particle energies can then be written as

$$\epsilon_i = \frac{k_i^2}{2m} + u_i \tag{2.23}$$

where m is the nucleon mass and

$$u_i = \sum_{j \leq k_F} < i,j|G(\omega = \epsilon_i + \epsilon_j)|i,j > . \tag{2.24}$$

Here $|i,j>$ represents a two-particle state with the spin, isospin, etc. indices supressed. The single-particle energies must of course be determined self-consistently as the total energy depends on the momentum (via equation 2.23) and vice versa (via equation 2.24). Once this calculation has been performed, the total energy density of bulk matter can be approximated by simply adding up the energies of the filled levels below k_F. (The result is only approximate since we have included only the 2-particle ladder diagrams — see below.) Note also that as in the case of the simple non-interacting model above, the requirements

of β-equilibrium and charge neutrality put constraints on the otherwise-independent Fermi momenta for the three particle species involved.

To summarize, given an explicit form for the 2-body NN potential (for example one of the modern Nijmegen-based forms) we can calculate the total energy density of bulk electrically neutral, equilibrated neutron star matter. Similarly, the pressure can be calculated by observing how the energy density varies with the baryon number density: $P = \partial E/\partial V = n^2\partial(\epsilon/n)/\partial n$. Since the various modern potentials are all fit to the same low energy scattering data, their predictions are very similar for low densities when the Fermi momenta are below about $300MeV$. In this regime, small differences arise from the different extrapolations to off-shell amplitudes associated with the different physical models. For larger densities, the differences between different potentials can become quite large, as they are being extrapolated beyond the energy range of the data to which they were fit. For more details, see the excellent review by Heiselberg [16]. We reproduce in Figure 2.2 the energy densities of several different modern potentials (as functions of the overall baryon number density) calculated as described above. As one example of the differing behaviors of the different potentials at high densities, the Bonn and Argonne potentials mentioned previously, solved in the Brueckner-Hartree-Fock approach, predict NS matter energy densities differing by $20 - 30\%$ at $4 - 5$ times nuclear matter density.

The state-of-the-art for equation of state calculations based on microscopic potential models involves the use of quantum Green's function Monte Carlo (GFMC) methods in which a trial A-nucleon wave function $\Psi(\mathbf{R})$ (with $\mathbf{R} = \mathbf{r_1}, ..., \mathbf{r_A}$) is operated on by the imaginary time evolution operator $\exp(-H\tau)$ which projects out the exact ground state, $\Psi_0(\mathbf{R})$. Due to the fast increase of required degrees of freedom with increasing A, such calculations have been limited to $A < 10$ for nuclei. Carlson has used this method to calculate the exact ground state for 14 neutrons in a periodic box [30].

It should be noted that even the approaches outlined so far are still not sufficient to produce realistic results. As is well-known from attempts to calculate the binding energy of tritium, the basic 2-body scattering potentials must be supplemented with 3- (and higher-) body interactions. The effects of these multi-body interactions are expected to become increasingly important at higher densities where the nucleons increasingly overlap with one

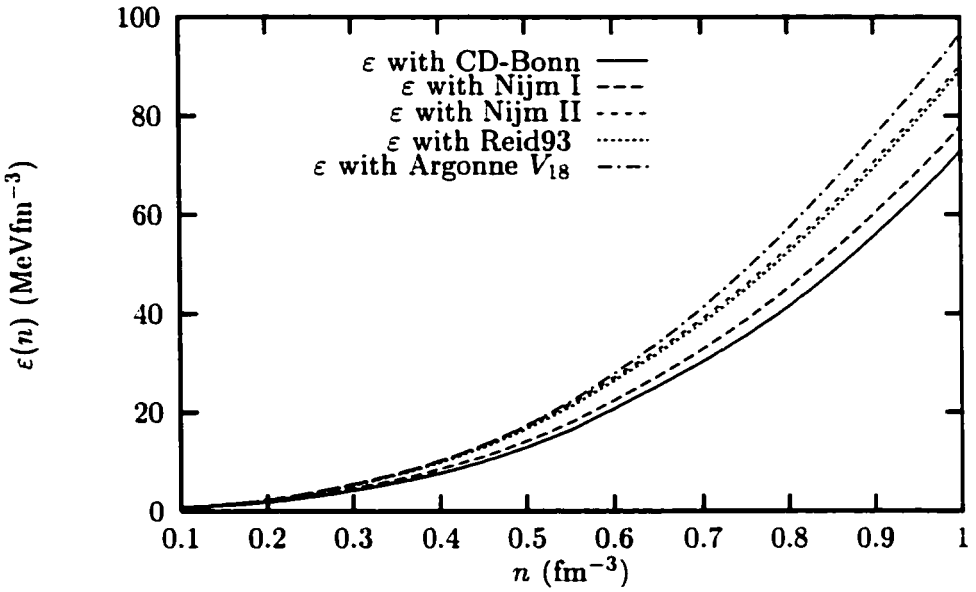

Figure 2.2: The total energy density of β-stable matter as a function of the baryon number density n. In addition to the Bonn and Argonne potentials mentioned in the text, results are shown for Nijmegen I and II and Reid potentials of the Nijmegen group [27]. The figure is taken from Ref. [16].

another. As less is known about 3- and 4-body interactions than is known about 2-body interactions, inclusion of the former necessarily involves physical assumptions that cannot be reliably fit to empirical data.

Another shortcoming of the approach outlined above is the failure to include all possible intermediate states in the calculation of the effective potential. Inclusion of intermediate particle-hole and hole-hole states, for example, will modify the results somewhat. Also, new particles such as hyperons (strangeness-containing baryons) can be expected to appear at high densities; here again, little is known about the microscopic nucleon-hyperon and hyperon-hyperon interactions so it is difficult to include such effects accurately in the microscopic many-body calculations. Also, because many of the modern potentials are based on non-relativistic potential models, one must include "by hand" relativistic corrections. The need for this can be seen quite strikingly by considering that the un-corrected potentials tend to predict superluminal sound speeds (i.e., $v_{sound}^2 = \partial P/\partial \epsilon \geq c^2$) for neutron star matter with density above a few times nuclear matter density. This prediction is obviously unphysical. Methods of resolving this problem include using Dirac-Brueckner or Dirac-Hartree-Fock many body theory, including relativistic boost corrections to the non-relativistic NN interactions, and/or simply forcing the equation of state to obey causality ($v_{sound} \leq c$) by arbitrarily reducing the pressure at high densities [16]. In order to illustrate the effects of several of these corrections, we show in Fig. 2.3 the mass-radius relation for neutron stars calculated with several variants of the Argonne v18 potential.

The several difficulties mentioned above (especially those involving the inclusion of relativistic effects) motivated very early on the creation of a simple, fully relativistic formalism for dealing with high density nuclear matter. Such a model was first proposed (in its modern form) by Walecka [33] in the 1970's. The idea is to begin with a relativistic field theory of nucleons (treated as Dirac spinors) interacting via Yukawa couplings to several mesons: the scalar/isoscalar σ, the vector/isoscalar ω, and the vector/isovector ρ. The model is often referred to as QHD (for Quantum HadroDynamics) to emphasize the formal similarity to the relativistic field theories (QED and QCD) describing the fundamental electromagnetic and color interactions among electrons and quarks. Because the theory is built on the framework of a relativistic field theory, QHD (or the "Walecka model" as it is also often

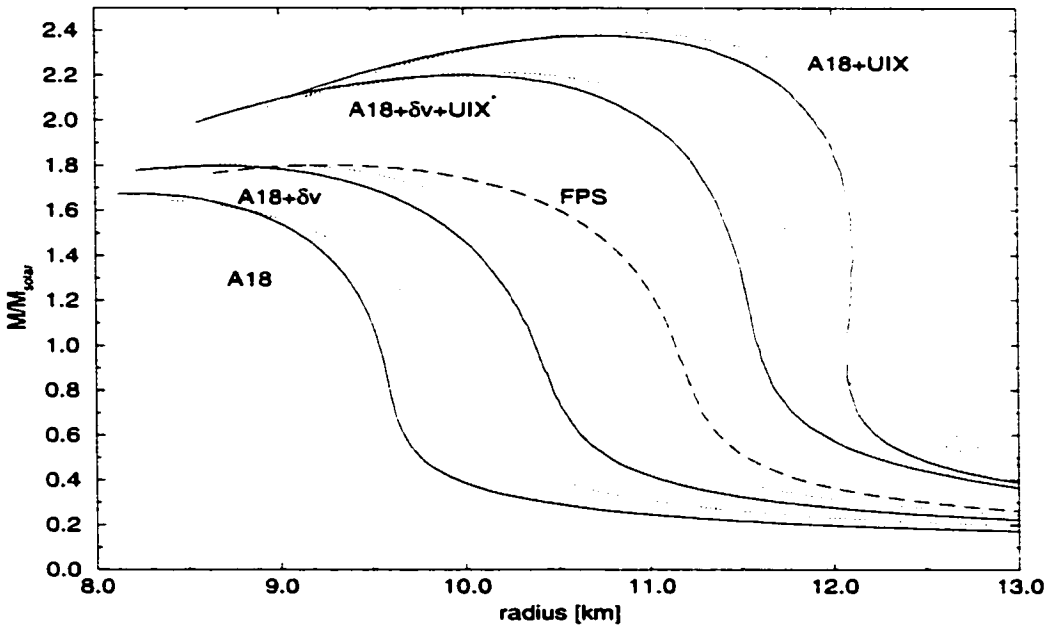

Figure 2.3: Neutron star gravitational mass $M(R)$ vs. radius R for several variants of the microscopic potential models described in the text. The label δv indicates the leading order-$(v/c)^2$ relativistic boost correction, while UIX refers to a 3-nucleon interaction term. Full curves are for β-stable matter and dotted ones for pure neutron matter. The curve labelled FPS is taken from an older calculation of Ref. [31], shown simply for comparison. Figure taken from Ref. [32].

called) automatically preserves causality ($v_{sound} \leq c$) at arbitrarily high densities.

As indicated, the fundamental degrees of freedom in QHD are Dirac nucleons and several mesons (scalar, vector, and vector-isovector) which mediate interactions among the baryons. The QHD Lagrangian is written:

$$\begin{aligned}
\mathcal{L}_N &= \overline{\Psi}_N \Big(i\gamma^\mu \partial_\mu - m_N^* - g_{\omega N}\gamma^\mu V_\mu - g_{\rho N}\gamma^\mu \vec{\tau}_N \cdot \vec{R}_\mu \Big) \Psi_N \\
&\quad + \frac{1}{2}\partial_\mu \sigma \partial^\mu \sigma - \frac{1}{2}m_\sigma^2 \sigma^2 - U(\sigma) - \frac{1}{4}V_{\mu\nu}V^{\mu\nu} \\
&\quad + \frac{1}{2}m_\omega^2 V_\mu V^\mu - \frac{1}{4}\vec{R}_{\mu\nu} \cdot \vec{R}^{\mu\nu} + \frac{1}{2}m_\rho^2 \vec{R}_\mu \cdot \vec{R}^\mu ,
\end{aligned} \tag{2.25}$$

where $m_N^* = m_N - g_{\sigma N}\sigma$ is the nucleon effective mass, which is reduced compared to the free nucleon mass due to the scalar field σ. This is of course equivalent to a Yukawa 3-point interaction between the nucleon and the scalar meson σ. The vector fields corresponding to the omega and rho mesons are given by $V_{\mu\nu} = \partial_\mu V_\nu - \partial_\nu V_\mu$, and $\vec{R}_{\mu\nu} = \partial_\mu \vec{R}_\nu - \partial_\nu \vec{R}_\mu$ respectively. This is exactly analogous to the form of the electromagnetic field $F_{\mu\nu}$ in the usual relativistic version of, for instance, the QED Lagrangian — one significant difference is that here we have included mass terms for the vector mesons; in QED such terms are forbidden by gauge invariance. We have also included terms representing 3- and 4-point self-interactions of the scalar meson; these are given by $U(\sigma) = (1/3)bm_N(g_{\sigma N}\sigma)^3 + (1/4)c(g_{\sigma N}\sigma)^4$, where b and c are dimensionless coupling constants. Ψ_N is the nucleon field operator with $\vec{\tau}_N$ the nucleon isospin operator.

In principle the above Lagrangian should be supplemented by any and all higher-dimension operators which respect the relevant symmetries; such operators would include, for example, self-interactions among the ω and ρ mesons, direct 4-Fermi interactions among nucleons, etc. As written, therefore, the theory defined by the QHD Lagrangian above should be treated as an effective theory — the hope is that it contains sufficient freedom (and the appropriate low energy *degrees* of freedom) to accurately reproduce empirically observed properties of hadronic matter. The five coupling constants in the QHD Lagrangian can, in principle, be fit to any convenient empirical properties. Since our goal is to use the model to describe the bulk properties of extended nuclear matter, the obvious choice is to choose coupling constants in order to reproduce the experimentally measured properties of bulk nuclear matter at saturation density. This is essentially equivalent to matching the

theory onto the first several terms in the semi-empirical mass formula. One then hopes that the automatically-relativistic extrapolation to higher densities will result in accurate predictions for the densities of interest for neutron stars. This hope can be partially justified by analyzing the QHD approach from the perspective of density-functional theory in which one treats the energy density and pressure as expansions in the baryon number density. The "small parameter" of this expansion is approximately 1/3 at nuclear matter density, and remains less than unity for densities less than a few times nuclear matter density [34].

It should be noted that the coupling constants in the QHD Lagrangian are generally large, $g \geq 1$. Therefore, one cannot rely on perturbation theory as one does, for example, in QED. Instead, one usually solves the theory in the mean-field approximation, which involves replacing the meson fields σ, ω, ρ by their expectation values $< \sigma >, < \omega >, < \rho >$. Physically, this approximation is equivalent to treating the nuclear forces as being due to a homogeneous background of mesons, rather than as due to discrete meson exchanges. Such an approximation is expected to be quite accurate if the typical separation between nucleons is small compared to the Compton wavelength of the mesons [32]. This limit is approached for very dense neutron star matter, but is not satisfied for nuclear matter near nuclear saturation density. (Moreover, the densities required to nearly saturate this limit exceed the density at which quarks, rather than hadrons, become the relevant degrees of freedom.) On the other hand, the Walecka model at low density doesn't rely strongly on the mean-field approximation; as discussed above, it can be viewed as simply an effective field theory or density-functional theory with sufficient parametric freedom to reproduce observed nuclear matter properties [34]. Thus, we will assume that the mean-field description retains some accuracy at saturation density, so that we may fix the parameters of the model (specifically the five coupling constants in Equation 2.25) by matching to five "bulk" properties of nuclear matter [3, 35]:

- nuclear saturation density $n_0 = 0.16 fm^{-3}$
- symmetry energy $a_{sym} = 32.5 MeV$
- binding energy per nucleon $B/A = -16.3 MeV$

- compressibility $K = 230MeV$
- nucleon effective mass $m^*/m_N = 0.78$. [1]

It is interesting that the extrapolation involved in the mean-field description of neutron star matter is, in a sense, opposite to that used in the description of NS matter by the modern NN potentials. In the latter case, the description is known to be accurate at low energies (i.e., low densities), and one must worry about the extrapolation to high density. In the case of the Walecka-type models, however, the mean-field approximation itself can be safely relied on at high density, while the extrapolation to low density (where the mean-field approximation is less certain) is required to fit the theory to some empirically known nuclear properties. (Of course, it should also be noted that at sufficiently high densities, it will no longer be appropriate to describe hadronic matter in terms of nucleonic degrees of freedom: beyond this point, the QHD description is obviously inapplicable.) We will say more later about the relative merits of the relativistic mean-field approach as against the microscopic potential approaches described previously.

Let us return for the moment to the Walecka model and see how it is used to calculate the bulk properties of extended matter. Replacing the meson fields with their expectation values (the mean-field approximation) and then calculating equations of motion in the usual way yields the standard Dirac equation for the nucleons, with effective mass given by m_N^* and with an E&M-like coupling to the (Lorentz) vector fields ω and ρ:

$$\left[\gamma_\mu(k^\mu - g_\omega\omega^\mu - g_\rho\vec{\tau}\cdot\vec{R}^\mu) - m_N^*\right]\psi(k) = 0. \tag{2.26}$$

The equations of motion for the meson (mean-) fields (note we denote by r the expectation value of the ρ meson field, to avoid confusion with the baryon densities ρ_n^s, *etc.*.) are

$$-\nabla^2\sigma + m_\sigma^2\sigma = -\frac{dU}{d\sigma} + g_{\sigma B}(\rho_n^s + \rho_p^s)\,, \tag{2.27}$$

$$-\nabla^2\omega + m_\omega^2\omega = g_\omega(\rho_n + \rho_p)\,, \tag{2.28}$$

$$-\nabla^2 r + m_\rho^2 r = g_\rho(\rho_p - \rho_n). \tag{2.29}$$

[1] Strictly speaking, m^* is a model parameter arising in calculations of nuclear matter properties, and is thus not itself a "bulk property."

where the baryon densities ρ_i (for $i = n, p$) are given by

$$n_i = \frac{k_F^{(i)}}{3\pi^2} \tag{2.30}$$

while the scalar densities ρ_i^s are given by

$$n_i^s = \int_0^{k_F^{(i)}} \frac{k^2 \mathrm{d}k}{\pi^2} \frac{m_N^*}{\sqrt{k^2 + (m_N^*)^2}}. \tag{2.31}$$

For bulk nuclear matter, the meson mean fields are constants independent of space and time, and the ∇^2 terms in the meson equations of motion vanish. Note also that due to the rotational invariance of extended nuclear matter, only the time components of the ω and R fields (and only the isospin-3 component of $\vec{R}$) may take on nonzero expectation values. One pleasant feature of this model is that the five coupling constants (b, c, g_σ, g_ω, and g_ρ) can be written down as explicit algebraic functions of the five empirical quantities to which they are matched [3].

The energy density of bulk matter in the mean-field Walecka model can be found by summing the neutron and proton single-particle energies up to the Fermi momenta k_F^n and k_F^p. (Note that as before, the single particle spectrum must be determined self-consistently since the effective mass m_N^* depends on the scalar field σ.) This is supplemented with the meson field contributions. The total energy density is thus:

$$\begin{aligned} \epsilon &= \frac{1}{3} b m_N (g_\sigma \sigma)^3 + \frac{1}{4} c (g_\sigma \sigma)^4 + \frac{1}{2} m_\sigma^2 \sigma^2 + \frac{1}{2} m_\omega^2 \omega^2 + \frac{1}{2} m_\rho^2 \rho_{03}^2 \\ &\quad + \int_0^{k_F^{(p)}} \frac{k^2 \mathrm{d}k}{\pi^2} \sqrt{k^2 + (m_N^*)^2} + \int_0^{k_F^{(n)}} \frac{k^2 \mathrm{d}k}{\pi^2} \sqrt{k^2 + (m_N^*)^2}. \end{aligned} \tag{2.32}$$

Similarly, the pressure is given by:

$$\begin{aligned} P &= -\frac{1}{3} b m_N (g_\sigma \sigma)^3 - \frac{1}{4} c (g_\sigma \sigma)^4 - \frac{1}{2} m_\sigma^2 \sigma^2 + \frac{1}{2} m_\omega^2 \omega^2 + \frac{1}{2} m_\rho^2 \rho_{03}^2 \\ &\quad + \int_0^{k_F^{(p)}} \frac{k^4 \mathrm{d}k}{3\pi^2} \frac{1}{\sqrt{k^2 + (m_N^*)^2}} + \int_0^{k_F^{(n)}} \frac{k^4 \mathrm{d}k}{3\pi^2} \frac{1}{\sqrt{k^2 + (m_N^*)^2}}. \end{aligned} \tag{2.33}$$

In Figure 2.4 we compare the energy density, pressure, and electron chemical potential of electrically neutral, β-equilibrated extended nuclear matter as computed in the Walecka model to the simple non-interacting Fermi gas model discussed at the beginning of this section.

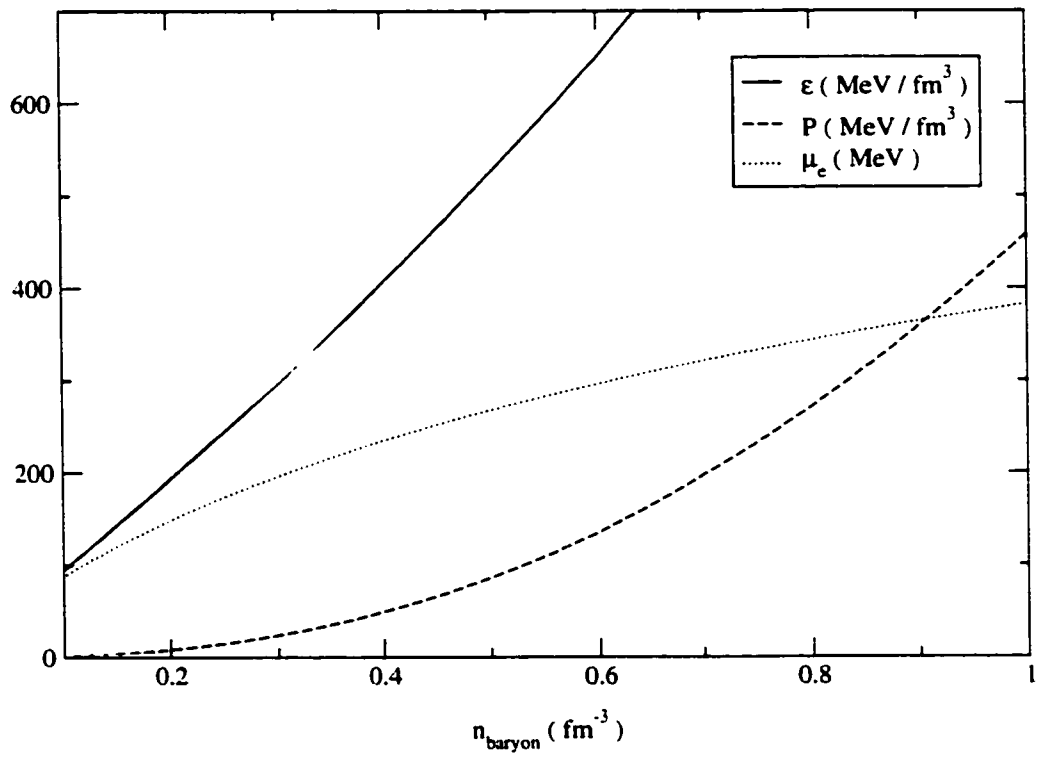

Figure 2.4: Energy density, pressure, and electron chemical potential for neutron star matter, calculated using the relativistic mean field model described in the text. The five coupling constants in the model are fit to match five empirical properties of (symmetric) nuclear matter at saturation. The gray-colored lines are a reproduction of the non-interacting model shown earlier. Note that as the density is increased to a few times nuclear matter density ($\rho_0 \sim 0.16 fm^{-3}$) the energy density and pressure are higher than in the non-interacting model. This is due primarily to the short-range repulsive interaction between nucleons, described in the Walecka model through the ω meson field. (It is not particularly clear on the graph, but at smaller densities near saturation, the energy density and pressure of the interacting theory are lower than the non-interacting theory, due to the long-range attractive interaction mediated by σ.) In addition, the electron chemical potential μ_e rises much more steeply with density in the model with realistic nuclear interactions. This is due to the symmetry energy term (incorporated via the ρ meson) which tends to increase the equilibrium number density of protons at a fixed baryon density. The requirement of charge neutrality in turn forces the number of electrons to increase, hence the rise in μ_e.

As already mentioned, one major advantage of the relativistic mean-field models is that they are automatically consistent with one thing we know absolutely about asymptotically dense nuclear matter: it must obey relativistic causality, which here means the speed of sound $\sqrt{\partial P/\partial \epsilon}$ must be smaller than c. Thus we might say that the Walecka model is "pinned" both to low density physics (via the fitting of coupling constants to properties of nuclear matter at saturation) and to high density physics (via the causality requirement), perhaps suggesting that the extrapolation to high density is more like an interpolation, and hence perhaps more reliable compared to the non-relativistic potential models which, as we have seen, tend to predict superluminal sound speeds at high density [36]. On the other hand, the mean-field models contain far fewer free parameters than the modern phenomenological potentials, and can therefore be fit to only a relatively small amount of low energy data. Both treatments involve a very extreme extrapolation to extreme isospin, from nearly symmetric nuclear matter to neutron star matter in which the neutron:proton ratio is as high as ten or more. Given the calculational simplicity of the mean-field models, we choose to use them for much of the subsequent work presented. Ultimately, though, the correct perspective on this choice is to give primacy to experiment: the clearest way to determine the high-density NS matter EOS is to simply observe the properties of real neutron stars. Consistency with such observations is the ultimate test of different theoretical approaches, not any hand-waving about which set of extrapolations is the least dubious. Ultimately, as we indicated in Chapter 1, the observed mass-radius curve of real neutron stars will determine uniquely the equation of state for matter above nuclear saturation density.

Before moving on to discuss phase transitions in NS matter, we should mention the possibility of superfluidity. As is well-known from the BCS theory of superfluidity / superconductivity, any aribitrarily weak attractive interaction between pairs of particles at the Fermi surface renders the surface unstable to so-called Cooper pairing. In this phenomenon, pairs of particles near the Fermi surface form pseudo-bound states which, since the pairs are bosonic quasi-particles, can form a ground state condensate $< \psi\psi > \neq 0$. In the case of electron Cooper pairing in metals, this condensate of charged particles spontaneously breaks the $U(1)$ symmetry of electromagnetism, resulting in superconductivity.

In the low density outer part of a neutron star, similar pairing is likely to occur in the

attractive $^1S_0$ channel between pairs of neutrons on opposite sides of the Fermi surface. At higher densities above the liquid-gas phase transition, protons are likely to form a superconducting condensate in the same $^1S_0$ channel, while neutrons are expected for form a superfluid in the coupled $^3P_2 - {}^3F_2$ channel. These expectations are confirmed by explicit solutions of the BCS gap equations using the modern phenomenological potentials [16].

As hinted at previously, the presence of superfluid phases in neutron star matter may be relevant in explaining observationally accessible NS phenomenology including glitches and cooling rates. Glitches, for example, may be related to the pinning of superfluid vortices to the Coulomb lattice in the neutron star crust: as the star spins down, the superfluid component gives up its angular momentum in discrete bursts as vortices become unpinned and recoil away. A precise knowledge of the $^3P_2 - {}^3F_2$ pairing gap is also relevant to understanding the cooling rates of NS matter. The presence of a gap Δ can be expected to suppress cooling rates by a factor $\sim e^{-\Delta/T}$, since no quasi-particle excitations will be present with $E < \Delta$. Calculations suggest a small gap of order $.1MeV$ for the $^3P_2$ partial wave channel; this is therefore likely to affect only the relatively late-time cooling history when $T < 1MeV$.

2.3 Phase Transitions in Neutron Star Matter

So far our discussion has assumed that neutron star matter is made up exclusively of neutrons, protons, and electrons. While this is likely the case for matter not too far above saturation density n_0, new particles *must* appear as the density is increased. This can be seen by examining Fig. 2.4, in which the electron chemical potential rises monotonically with the baryon density. At some point near a few times ρ_0 (for the non-interacting model) or near ρ_0 itself (for the interacting Walecka model) μ_e becomes as large as the mass of the muon, m_μ. At this point, it will become energetically favorable for electrons at the top of the Fermi sea to decay according to

$$e^- \rightarrow \mu^- + \nu_e + \bar{\nu}_\mu \tag{2.34}$$

where, as before, the neutrinos will simply escape the star.

Similarly, it is clear that when the chemical potential for baryon number (μ_n) exceeds the mass of the next-heavier baryons beyond neutrons and protons (for example, the Σ and Λ) these hyperons will begin to replace neutrons and protons from the top of their respective Fermi seas. Interestingly, despite the fact that the Λ hyperon is nearly $100\,MeV$ lighter than the isospin triplet of Σ's, the Σ^- is expected to appear first due to its negative electric charge. Its chemical potential in β-equilibrium should satisfy

$$\mu_{\Sigma^-} = \mu_n - \mu_e \tag{2.35}$$

and the Σ^- hyperon will thus begin to appear when this quantity exceeds its mass. (Actually, what is relevant is not its rest mass, but its in-medium mass, i.e., the energy of a zero-momentum Σ^- including the potential energy arising from interactions with the background of neutrons and protons.) That this will occur before $\mu_\Lambda = \mu_n$ exceeds m_Λ is clear from examination of Fig. 2.4.

One may think of the appearance of new particle species at high density as an attempt by the system to "elude" the Pauli exlusion principle. By spreading the conserved charges (such as baryon number and electric charge) over as many distinct Fermi seas as possible, the overall energy is reduced. It is clear, then, that an even more effective means of reducing the energy would be to replace some fermions by bosons. Since the latter are not subject to the exclusion principle, an unlimited number of particles can be put in the lowest energy state.

This is precisely the motivation behind several hypothesized phase transitions including pion- and kaon-condensation. Returning again to Fig. 2.4, we can argue as before that whenever μ_e exceeds the in-medium effective mass of a π^- or K^- meson, a Bose-Einstein condensate of mesons will be an energetically favored storehouse for negative electric charge and mesons will appear according to

$$e^- \rightarrow \nu_e + \left(\pi^- \text{ or } K^-\right). \tag{2.36}$$

Given the relative lightness of the pion compared to the kaon (in vacuum) one naively expects π^- to condense at a lower density. Due to the repulsive s-wave interaction between pions and nucleons, however, the in-medium pion mass grows with increasing baryon density, and pion-condensation is disfavored [37, 38].

We will analyze the case of negative kaon condensation in detail in the following chapter. Let us, however, first derive several useful results applicable to any first-order phase transition which may occur in neutron star matter. We will consider the case of a phase transition to deconfined quark matter for purely illustrative purposes.

So far, we have assumed that the allowed particle spectrum in high density neutron star matter is the same as the observed particle spectrum in vacuum: at lower densities, matter is composed of neutrons, protons, and electrons, while "exotic" particles such as muons, hyperons, and various mesons may appear at higher densities. Given the asymptotic freedom of QCD, however, it is clear that at some point hadrons (baryons and mesons) will cease to be the appropriate quasi-particles for description of high-density matter. Instead, the appropriate degrees of freedom will be the explicit particles in the QCD Lagrangian, namely quarks and gluons. At some density, then, a deconfining phase transition will occur in which quarks lose their "family ties" to distinct baryons and mesons [39, 40, 41, 42].

Deconfined quark matter can be described using the so-called bag models. For the simplest case of non-interacting quarks, the pressure and energy density of deconfined quark matter can be written using the same Fermi gas integrals seen previously:

$$\epsilon = \sum_f \frac{1}{\pi^2} \int k^2\, dk\, \epsilon_f(k)\, [n(k, \mu_f) + n(k, -\mu_f)] + B \tag{2.37}$$

and

$$P_0 = \sum_f \frac{1}{3}\frac{1}{\pi^2} \int k^3\, dk\, \frac{\partial \epsilon_f(k)}{\partial k}\, [n(k, \mu_f) + n(k, -\mu_f)] - B \tag{2.38}$$

where we have included terms for both quarks and anti-quarks. The constant B — the "bag constant" — represents the (negative) energy density of the usual, hadronic vacuum which is expelled by the presence of free quarks. This adds a positive relative energy density to kinetic contributions to ϵ arising from the quarks themselves, and acts as a constant (negative) shift in the pressure of quark matter representing the tendency of the hadronic vacuum to refill the bag. $\epsilon_f(k)$ is the usual expression $\sqrt{m_f^2 + k^2}$ while $n(k, \mu_f) = 1/[1 + \exp(\epsilon_f(k) - \mu_f)/T]$. The label f runs over the various flavors of quarks (up, down, and/or strange) which are assumed to be present.

It is possible to include interactions among the quarks; for example, the pressure is

modified by order-$\alpha_s = g_{QCD}^2/4\pi$ corrections [16] as

$$P \to P_0 - \frac{\alpha_s}{\pi^3}\sum_f \left[\frac{3}{2}\left(\mu_f k_f - m_f^2 ln\left(\frac{\mu_f + k_f}{m_f}\right)\right)^2 - k_f^4\right]. \tag{2.39}$$

(It should be noted, though, that at the relevant densities the strong coupling constant α_s is by no means small compared to unity. Hence, the first-order-in-α_s correction to the energy density in Eq. 2.39 is really rather meaningless, as the series is not a converging one.) Both the pressure and energy density should be supplemented with the contributions of electrons, which are in general needed to ensure electric charge neutrality.

The usual expectation is that a phase transition from hadronic matter to deconfined quark matter will occur at some critical density. As we have seen, electric charge neutrality of the hadronic phase implies that $n_p = n_e$, possibly supplemented by contributions from charged muons or hyperons. Weak equilibrium among the various hadronic species places a second constraint on the three components, leaving only a single free parameter which we may take as the baryon density n_B. Similarly, for quark matter, electric charge neutrality requires

$$\frac{2}{3}n_u - \frac{1}{3}n_d - \frac{1}{3}n_s = n_e \tag{2.40}$$

while β-equilibrium will guarantee that $\mu_d = \mu_s = \mu_u + \mu_e$. Again, these constraints leave only a single degree of freedom which can again be taken as $n_B = (n_u + n_d + n_s)/3$.

The critical density at which bulk hadronic matter is replaced by bulk quark matter is determined by the requirements of phase coexistence. As we have seen before, mechanical equilibrium across the boundary requires that $P^I = P^{II}$ and $\mu_i^I = \mu_i^{II}$ where the labels I and II refer to the hadronic and quark phases respecitvely. The index i runs over all conserved charges (namely baryon number and electric charge); the baryon number chemical potential in the quark phase is defined as $\mu_n^{II} = (2\mu_d + \mu_u)$. The coexistence conditions can be satisfied by the usual Maxwell construction [43], which occurs over a range of n_B with constant pressure. That is, if n_B is continuously increased from zero, the new quark matter phase will first appear (as droplets with a small volume filling fraction) at some critical density n_{crit}. As n_B is raised beyond n_{crit} the volume fraction of the quark phase increases smoothly until it reaches unity at a second critical density, n'_{crit}. At this point pure quark

matter is the favored configuration. Between n_{crit} and n'_{crit} the pressure remains fixed at a constant value P_{crit}. (This is shown in Fig. 2.3.)

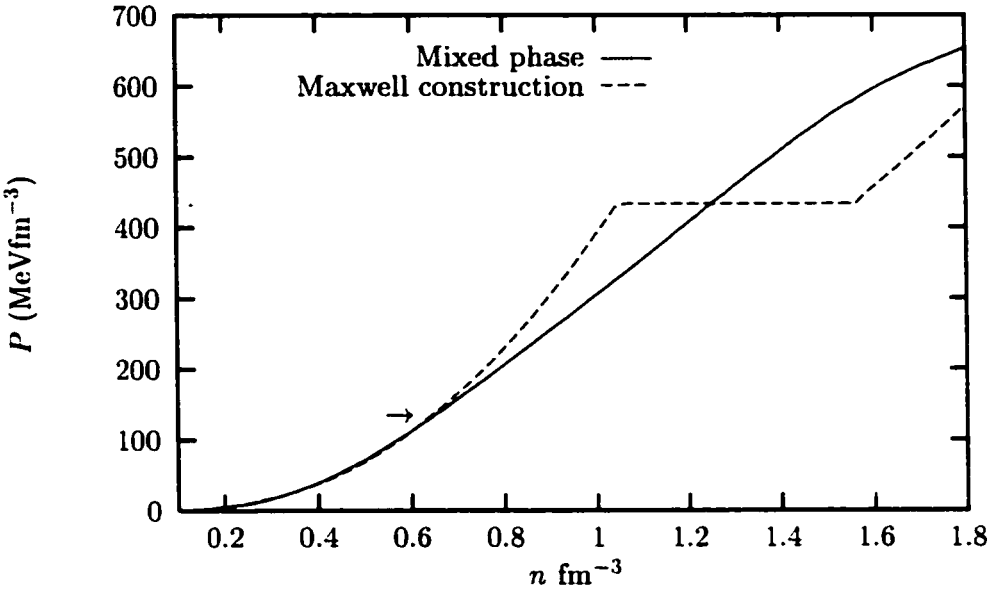

Figure 2.5: Pressure as function of density for both the Maxwell construction and crystalline mixed phase. The bag constant was taken to be $B^{1/4} = 200MeV/fm^3$. The arrow on the figure indicates the beginning of the mixed phase region. Taken from Ref. [16].

Examination of the equations for hydrostatic equilibrium, however, shows that a finite region of constant pressure in a neutron star is strictly forbidden — the pressure must increase monotonically with increasing depth in the star, since the energy density $\epsilon(r)$ nowhere vanishes. This implies that the transition from hadronic to deconfined quark matter will occur suddenly in the star at the point where the pressure reaches P_{crit}. Outside of this radius, matter will be electrically neutral bulk hadronic matter, while the core of the star will consist of electrically neutral deconfined quark matter.

As was realized recently by Glendenning, however, this qualitative picture may be dramatically changed if we relax the assumption of seperate electric charge neutrality in the two phases. Indeed, as we saw in the case of the low-density liquid-gas phase transition, matter need not be absolutely homogenous, i.e., *locally* charge neutral. Instead, the absolute lowest energy configuration may involve regions of electrically-charged phases which form a

lattice structure in a way that preserves overall or global charge neutrality. In the case of the hadron-quark phase transition, it is simple to see that relaxing the constraint of local electric charge neutrality allows for the coexistence of the two phases over a much wider range of n_B and — more importantly for the structure of neutron stars — over a wide range of pressures.

Previously we saw that each phase was described by a single free parameter, the baryon number density. Now, with one fewer constraint, we have an additional free parameter which we may take to be the electron chemical potential μ_e. This can be varied so as to satisfy mechanical equilibrium ($P^I = P^{II}$) between the two phases. At a given n_B this fixes the composition of each phase, in particular determining the electric charge densities which are

$$\rho^I_{charge} = n_p - n_e \tag{2.41}$$

for the hadronic phase and

$$\rho^{II}_{charge} = \frac{2}{3}n_u - \frac{1}{3}n_d - \frac{1}{3}n_s - n_e \tag{2.42}$$

for the quark matter phase. Overall electric charge neutrality is then satisfied by introducing the quark phase filling fraction

$$f = \frac{V^{II}}{V^I + V^{II}} = \frac{\rho^I_{charge}}{\rho^I_{charge} - \rho^{II}_{charge}}. \tag{2.43}$$

This quantity describes the fraction of spatial volume that will be filled by phase II in order that matter will be overall electrically neutral. Other thermodynamic quantities of interest can then be calculated by volume-fraction-weighted averaging; the energy density of the mixed phase, for example, is given by

$$\epsilon_{bulk} = f\,\epsilon^{II} + (1-f)\,\epsilon^I \tag{2.44}$$

where $\epsilon^{(I,II)}$ are the bulk energy densities of the two phases. Actually, this is not quite complete — as in the case of the liquid-gas transition discussed previously, there are contributions to the energy from surface and Coulomb terms. These have precisely the same form seen above, so we may simply write

$$\epsilon = \epsilon_{bulk} + \epsilon_{surface} + \epsilon_{Coulomb}. \tag{2.45}$$

Also as before, the favored geometrical arrangement of the two phases is determined by minimizing the surface and Coulomb contributions to the energy density. For $f \ll 1$ (small filling fraction) this is achieved by having small spherical droplets of (negatively charged) quark matter immersed in a positively charged hadronic matter background. Minimizing $\epsilon_{surface} + \epsilon_{Coulomb}$ with respect to the droplet radius R gives a favored radius

$$R_0 = \left[\frac{15}{8\pi} \frac{\sigma}{(\rho^{II}_{charge} - \rho^{I}_{charge})^2} \right]^{1/3} \tag{2.46}$$

which is typically of order $5\,fm$ for realistic values of the surface tension σ and the charge densities of the two phases. As in the case of the liquid-gas transition, at higher filling densities where the filling fraction is larger, spherical droplets (sometimes called "meatballs") are expected to merge into rods ("spaghetti") and eventually slabs ("lasagna"). Then, as f grows from about 1/2 to 1, the phases turn inside out (forming "anti-pasta") — slabs of quark matter merge together leaving rod-shaped regions of hadronic matter, the rods break apart and shrink to spherical bubbles, and finally we reach bulk electrically neutral quark matter when $f \to 1$.

This construction allows a crystalline mixed phase to exist over a wide range of pressures (see Fig. 2.5) and therefore over a large radial extent of the neutron star. In Fig. 2.6 is shown a plot of the favored geometry (droplets vs. rods, etc.) as well as the structure size and spacing as the filling fraction is varied from 0 to 1. As mentioned in the previous chapter, the existence of a heterogenous mixed phase region throughout the interior of a neutron star may affect observable properties such as supernova neutrino light curves, cooling histories, and spin-down rates. Perhaps more importantly, the presence of this new phase of matter through much of the star will generally soften the equation of state for densities above the critical density at which the new phase first appears. By definition, an energetically-favored new phase will reduce the energy density at constant baryon density. This will tend to reduce the gravitational mass M of a neutron star with total baryon number N_B. Similarly, it will reduce the maximum neutron star mass M_{max} as compared to the pure hadronic equation of state. A softer equation of state could also affect the supernova mechanism itself, producing gravitationally-deeper and hence more energetic bounces.

Future empirical observations of neutron star masses and radii may thus shed much light on the nature of possible phase transitions in dense matter. In particular, the deviation of the empirical mass-radius curve from that expected for pure hadronic (neutron, proton, electron, ...) matter will signal the density at which a new phase such as deconfined quark matter is appearing. As we have seen, however, the hadronic equation of state is not currently known for matter at several times nuclear density, so one does not know which empirical mass and radius data points are to be regarded as "deviant." On the other hand, many otherwise well-motivated models predicting phase transitions at relatively low densities yield maximum NS masses which are substantially below the $M_{NS} \geq 2.0 M_{\odot}$ observations mentioned in Chapter 1. It should also be mentioned that even a clear observation of the softening of the high-density equation of state may not allow us to distinguish *which* phase transition has occurred in the star. Here we have used the quark-deconfinement transition as a pedagogical example to illustrate the basic physics, but as we will see shortly, other phase transitions are possible. Mass-radius curves for kaon-condensate stars, for example, may turn out to be virtually indistinguishable from those for stars containing deconfined quark matter.

In subsequent chapters, we will apply much of the technology developed here to the specific case of the proposed condensation of kaons in dense matter.

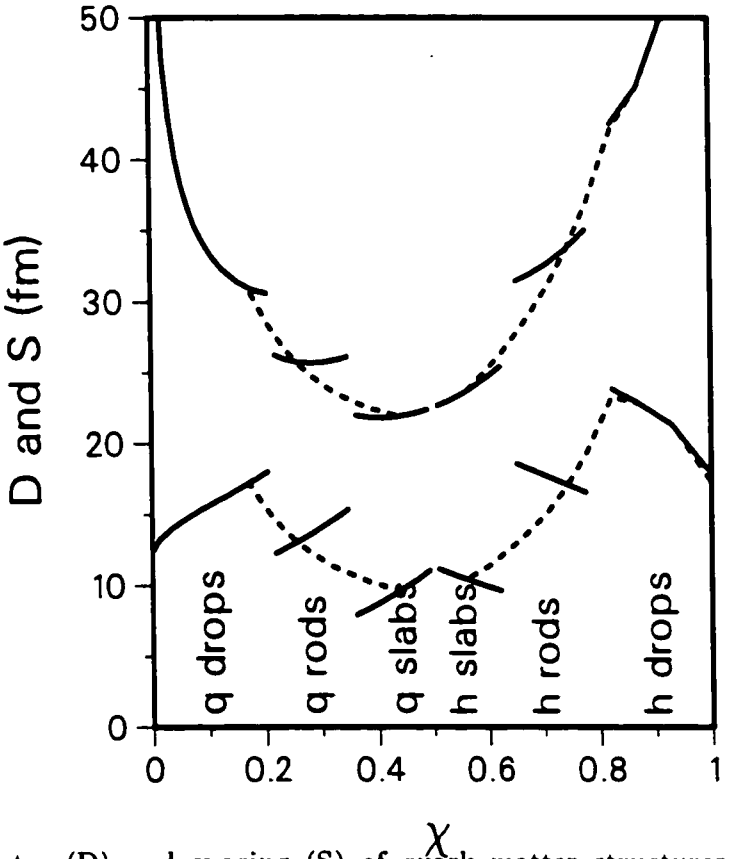

Figure 2.6: Diameter (D) and spacing (S) of quark matter structures as a function of the quark phase filling fraction. Each separate piece of the curve is calculated under the assumption of a specific geometry (spherical droplets, cylindrical rods, etc.) — only the geometry which minimizes $\epsilon_{surface} + \epsilon_{Coulomb}$ is shown for each value of the filling fraction. The dotted line represents an interpolation suggesting the possibility of "fractal" geometries lying, e.g., somewhere between spherical and cylindrical symmetry, etc. Figure taken from Ref. [44]

Chapter 3

FIRST ORDER KAON CONDENSATION: FINITE SIZE EFFECTS IN THE MIXED PHASE

In this chapter we study in detail one particular phase transition hypothesized to occur in neutron star matter: kaon condensation. After presenting the original arguments motivating the consideration of kaon condensation, we present a specific model in which the transition to kaon-condensed matter is first order. The standard methods of analyzing the resulting mixed-phase region in the neutron star are then reviewed. Finally, we present the results of detailed calculations of the role played by Coulomb and surface effects in the mixed phase, including the effect of Debye screening by electrons and other charged particles. We briefly mention possible implications for neutron star phenomenology, saving a more systematic discussion for the final chapter.

3.1 Introduction to Kaon Condensation

The original motivation for consideration of negative kaon condensation in high-density matter was an argument put forward by Kaplan and Nelson [45]. They wrote down the leading pion-octet - baryon coupling terms in the $SU(3)_L \times SU(3)_R$ chiral Lagrangian:

$$\begin{aligned}\mathcal{L} &= \frac{1}{4}f^2\mathrm{Tr}\partial_\mu U\partial^\mu U^\dagger + C\mathrm{Tr}M(U+U^\dagger-2) + i\mathrm{Tr}\bar{B}\gamma^\mu\left[V_\mu, B\right] \\ &+a_1\mathrm{Tr}\bar{B}\left(\xi M\xi + \xi^\dagger M^\dagger\xi^\dagger\right)B + a_2\mathrm{Tr}\bar{B}B\left(\xi M\xi + \xi^\dagger M^\dagger\xi^\dagger\right) \\ &+a_3\left(\mathrm{Tr}\bar{B}B\right)\left(\mathrm{Tr}MU + \mathrm{Tr}U^\dagger M^\dagger\right) \end{aligned} \tag{3.1}$$

Here $U = \xi^2$ is the usual non-linear sigma model (octet) pion field, $f = 93MeV$ is the pion decay constant, and $M = \mathrm{diag}(0, 0, m_s)$ is the quark mass matrix (where we have ignored

m_u and m_d relative to the much larger m_s). The octet of baryon fields is given by

$$B = \begin{pmatrix} \sqrt{\frac{1}{2}}\Sigma^0 + \sqrt{\frac{1}{6}}\Lambda & \Sigma^+ & p \\ \Sigma^- & -\sqrt{\frac{1}{2}}\Sigma^0 + \sqrt{\frac{1}{6}}\Lambda & n \\ \Xi^- & \Xi^0 & -\sqrt{\frac{2}{3}}\Lambda \end{pmatrix}. \tag{3.2}$$

The meson vector current is $V_\mu = \frac{1}{2}\left(\xi^\dagger \partial_\mu \xi + \xi \partial_\mu \xi^\dagger\right)$. Assuming that only kaons are present, we may write

$$U = exp\left(\frac{2i}{f}\pi\right) \tag{3.3}$$

with

$$\pi = \frac{1}{\sqrt{2}} \begin{pmatrix} 0 & 0 & K^+ \\ 0 & 0 & 0 \\ K^- & 0 & 0 \end{pmatrix} \tag{3.4}$$

and K^+ and K^- the positive and negative kaon fields. Plugging this ansatz into the Lagrangian above gives the leading order effective theory for charged kaons in a background of baryons. It contains kaon-nucleon interaction terms

$$\mathcal{L}_{KN} = \frac{3i}{8f_\pi^2} n(K^+\partial_0 K^- - K^-\partial_0 K^+) + \frac{\Sigma^{KN}}{f_\pi^2} n^{(s)} K^+ K^- \tag{3.5}$$

where

$$\Sigma^{KN} = -\frac{1}{2}(a_1 + 2a_2 + 4a_3)m_s. \tag{3.6}$$

The factors n and $n^{(s)}$ refer to the baryon number density ($\bar{B}\gamma^0 B$) and scalar density ($\bar{B}B$) respectively. The factor $(a_1 + a_2)m_s$ is known from the observed mass splittings of the baryons in the octet; $a_3 m_s$ is related to the strangeness content of the proton $< p|\bar{s}s|p >$ but is poorly known: $a_3 m_s = -(220 \pm 40) MeV$ [46].

At low densities, $n \sim n^{(s)}$ and we can model the attraction represented by Eq. 3.5 with a single term of the form

$$H_{int} = -m_K^2 |K|^2 n/n_{crit} \tag{3.7}$$

where n_{crit} is a constant which depends on the value of Σ^{KN} characterizing the strength of the interaction and m_K^2, in terms of the parameters of the chiral Lagrangian, is given to leading order by $m_K^2 = 2Cm_s/f^2$. Eq. 3.7 clearly shows that a large baryon density reduces

the effective mass of the kaons, and vice versa: the presence of kaons reduces the effective mass of the baryons. This suggests that at sufficiently high density (near n_{crit}) the energy of a a uniform system of baryonic matter can be lowered via the appearance of a nonzero condensate of charged kaons, $< |K|^2 > \neq 0$. Early calculations [45] suggested a value of $n_{crit} \sim 3n_0$ (where n_0 is nuclear matter density), implying that kaons are likely to condense in the cores of neutron stars. (See Appendix B for a discussion of why kaons, and not their lighter pseudoscalar cousins the pions, are thought to be the most like candidate for meson condensation.)

So far we have assumed that the density of the kaon condensate increases smoothly (starting from zero) as the baryon density is increased from zero through n_{crit} — i.e., we have assumed that the transition is second order. But this need not be the case; indeed, a first order transition is both favored by some experiments (see below), and is also far more interesting from a neutron star phenomenology point of view. As mentioned in Chapter 2, a generic feature of first order phase transitions in neutron star matter is that a mixed phase region, where the nuclear phase coexists with a denser and energetically favorable new phase, is mechanically stable and can thereby occupy a significant spatial region in the interior of a neutron star [47]. The best studied example of a first order transition at high baryon density is the quark-hadron phase transition, where model calculations indicate that the mixed phase is favored for a wide range of pressure and consequently can occupy a large spatial extent (several km in radius) in the neutron star interior [42, 48].

In a recent article, Glendenning and Schaffner-Bielich studied a model for kaon condensation, where the transition to the kaon condensed phase is first order [49]. Thus, unlike earlier studies of kaon condensation [45, 52], where the transition was second order, the model due to Glendenning and Schaffner predicts exactly this kind of mixed phase where the kaon phase coexists with a nuclear phase throughout a potentially large region of the neutron star. Physically, the coexisting phases form the "pasta" structure mentioned in the previous chapter: coming in from the outer (low density) regions of the NS, one first begins to encounter negatively-charged droplets of the kaon phase immersed in (slightly positively-charged) nuclear matter. At higher densities (deeper inside the star) droplets merge to form rods and then slabs, etc. This naturally leads to the question of how surface and Coulomb

effects will influence the extent and structure of the mixed phase. Earlier studies, in the context of a quark-hadron phase transition, showed that surface and Coulomb effects are important [108]. It was found that the range of pressures over which the mixed phase is favored depended sensitively on the (poorly known) surface tension between the nuclear and quark phase. Glendenning's first-order kaon condensate model is especially appropriate for studying these effects since, unlike the case of the deconfinement transition, both the low- and high-density phases can be treated within the same theoretical model. Hence, one can study the boundaries between phases explicitly, and hence develop some confidence that surface effects are treated both realistically and self-consistently.

In the following sections, we calculate surface and Coulomb contributions (including the effects of Debye screening) to the thermodynamic potential in a mixed phase containing kaons. We identify their importance in the determination of the equation of state, the size and dimensionality of spatial structures, and the critical density for the onset of the mixed phase.

3.2 First Order Kaon Condensation

In this section we briefly review the model proposed by Glendenning and Schaffner [49] which predicts a first order transition from the nuclear to the kaon condensed phase. The nuclear phase is described by a relativistic, Walecka type, field theoretical model including the isovector meson ρ as well as cubic and quadratic self-interactions of the scalar meson [35, 3]. The Lagrangian for the nucleon sector is given by

$$\begin{aligned}
\mathcal{L}_N &= \overline{\Psi}_N\left(i\gamma^\mu\partial_\mu - m_N^* - g_{\omega N}\gamma^\mu V_\mu - g_{\rho N}\gamma^\mu\vec{\tau}_N\cdot\vec{R}_\mu\right)\Psi_N \\
&\quad + \frac{1}{2}\partial_\mu\sigma\partial^\mu\sigma - \frac{1}{2}m_\sigma^2\sigma^2 - U(\sigma) - \frac{1}{4}V_{\mu\nu}V^{\mu\nu} \\
&\quad + \frac{1}{2}m_\omega^2 V_\mu V^\mu - \frac{1}{4}\vec{R}_{\mu\nu}\cdot\vec{R}^{\mu\nu} + \frac{1}{2}m_\rho^2\vec{R}_\mu\cdot\vec{R}^\mu,
\end{aligned} \tag{3.8}$$

where $m_N^* = m_N - g_{\sigma N}\sigma$ is the nucleon effective mass, which is reduced compared to the free nucleon mass due to the scalar field σ. The vector fields corresponding to the omega and rho mesons are given by $V_{\mu\nu} = \partial_\mu V_\nu - \partial_\nu V_\mu$, and $\vec{R}_{\mu\nu} = \partial_\mu\vec{R}_\nu - \partial_\nu\vec{R}_\mu$ respectively. The

scalar self-interaction term is given by $U(\sigma) = (1/3)bm_N(g_{\sigma N}\sigma)^3 + (1/4)c(g_{\sigma N}\sigma)^4$, where b and c are dimensionless coupling constants. Ψ_N is the nucleon field operator with $\vec{\tau}_N$ the nucleon isospin operator. The five coupling constant, $g_{\sigma N}$, $g_{\omega N}$, $g_{\rho N}$, b, and c, are chosen to reproduce the empirical properties of nuclear matter at saturation density [35].

Kaons are included in the model in the same fashion as the nucleons, by coupling to the σ, ω and ρ meson fields. (See Appendix B for some discussion of the appropriateness of this general form of kaon-nucleon coupling.) There exist in the literature several meson-exchange Lagrangians which attempt to describe kaon-nucleon interactions. A detailed discussion of these models and their relation to the chiral Lagrangian proposed by Kaplan and Nelson [45] can be found in Pons, et al. [51]. In the present paper we employ the Lagrangian proposed by Glendenning and Schaffner. The Lagrangian for the kaon sector is given by

$$\mathcal{L}_K = \mathcal{D}^*_\mu K^* \mathcal{D}^\mu K - m_K^{*2} K^* K, \tag{3.9}$$

where K denotes the isospin doublet kaon field. The covariant derivative $\mathcal{D}_\mu = \partial_\mu + ig_{\omega K}V_\mu + ig_{\rho K}\vec{\tau}_K \cdot \vec{R}_\mu$ couples the kaon field to the vector mesons and the kaon effective mass term $m^*_K = m_K - g_{\sigma K}\sigma$ describes its coupling to the scalar meson. $\vec{\tau}_K$ is the kaon isospin operator. The vector coupling constants are determined by isospin and quark counting rules [49], and are given by $g_{\omega K} = g_{\omega N}/3$ and $g_{\rho K} = g_{\rho N}$. (These can be understood as the leading-order approximation in the $1/N_C$ expansion [66], where N_C is the number of colors.)

The scalar coupling is fixed by fitting to an empirically determined kaon optical potential in nuclear matter. Albeit poorly known, the real part of the optical potential in nuclear matter as deduced from kaonic atoms indicates that 80 MeV $< U_K(n_o) <$180 MeV [53, 54]. Here, we choose $U_K(n_o) = 120$ MeV to fix $g_{\sigma K}$.[1] Lower values of the optical potential favor

[1]Note, however, that direct coupled-channel calculations of the K^- self energy in nuclear matter generally result in significantly lower predictions, near $40-60MeV$, for the optical potential. It has also been shown that these small values may adequately reproduce the data from kaonic atoms, though this is still contested. Two different methods for fitting the kaon optical potential to data from kaonic atom studies give two dramatically different results, one in the $40-60MeV$ range favored by calculations, the other near the upper end of the $80-180MeV$ range quoted in the text. Information about the kaon optical potential can also be extracted from kaon production rates in heavy ion collisions, though the extrapolation from high-temperature, high-density back to zero-temperature nuclear matter density is strongly model-dependent. See, *e.g.*, [55, 56, 57] for a discussion. Pending resolution of this issue, we obviously cannot be certain when or even if kaons will condense in neutron stars. Nevertheless, it remains extremely interesting to study the effects kaon condensation may have on observable NS phenomenology, if it is in fact realized in nature.

a second order transition (and one which occurs only at higher overall densities), while higher values make the first order transition stronger. For the purpose of this study, we require that the phase transition be first order but the qualitative features of the results found here are independent of its precise value.

In the mean-field approximation only the time component of the vector fields and the isospin 3-component of the isovector field can have nonzero mean values. The equations of motion (EOM) for the non-strange meson fields can be derived from the above Lagrangians and are given by

$$-\nabla^2\sigma + m_\sigma^2\sigma = -\frac{dU}{d\sigma} + g_{\sigma B}(\rho_n^s + \rho_p^s) + g_{\sigma k} f_\pi^2 \theta^2 m_K^* \,. \tag{3.10}$$

$$-\nabla^2\omega + m_\omega^2\omega = g_\omega(\rho_n + \rho_p) - g_{\omega K} f_\pi^2 \theta^2 (\mu_K + X) \,. \tag{3.11}$$

$$-\nabla^2 r + m_\rho^2 r = g_\rho(\rho_p - \rho_n) - g_{\rho K} f_\pi^2 \theta^2 (\mu_K + X) \,. \tag{3.12}$$

where the meson fields σ, ω, r now represent the appropriate mean values, $X = g_{\omega K}\omega + g_{\rho K} r$, and $\rho_{(n,p)}^{(s)}$ are the (scalar) densities of neutrons and protons, Eq.2.31. The ansatz $K = f_K\theta/\sqrt{2}$ has been made, where f_K is the kaon decay constant and θ is a dimensionless kaon field strength parameter.

In the bulk approximation, the gradient terms are omitted and the EOM become non-linear algebraic equations to be solved self-consistently for the meson fields. The EOM for the kaon is

$$\left(\mathcal{D}_\mu \mathcal{D}^\mu + m_K^{*2}\right) K = 0. \tag{3.13}$$

where $m_K{}^* = m_K - g_{\sigma K}\sigma$ is the kaon effective mass and $\mu_K{}^* = \mu_e + X$. In terms of θ, the kaon EOM is re-expressed as

$$\nabla^2\theta = \left(m_K{}^{*2} - \mu_K{}^{*2}\right)\theta. \tag{3.14}$$

In the bulk mean field calculation, the solution to Eq.(3.14) and the other meson field equations are obtained with the gradient terms set equal to zero. This determines the condensate amplitude and the expectation values of the other meson fields [49] and completely specifies the ground state of matter at the mean field level. However, surface effects are ignored since the gradient terms in the EOM are neglected. In this work we explicitly retain the

gradient term and solve Eq.3.14 for the kaon condensate in the Wigner-Seitz approximation using spherical, cylindrical, or planar geometry as appropriate. This is described in detail in Section 3.3.

The energy density of the nuclear phase is

$$\begin{aligned}\epsilon_N &= \int_0^{k_F^{(n)}} \frac{\mathrm{d}^3k}{(2\pi)^3}\sqrt{k^2+{m_N}^{*2}} + \int_0^{k_F^{(p)}} \frac{\mathrm{d}^3k}{(2\pi)^3}\sqrt{k^2+{m_N}^{*2}} + \frac{\mu_e^4}{4\pi^2} \\ &+ \frac{1}{2}\left((\nabla\sigma)^2+{m_\sigma}^2\sigma^2\right) + \frac{1}{2}\left((\nabla\omega)^2+{m_\omega}^2\omega^2\right) \\ &+ \frac{1}{2}\left((\nabla r)^2+{m_\rho}^2r^2\right) + U(\sigma) \end{aligned} \tag{3.15}$$

where ${k_F}^{(n,p)}$ are the neutron and proton Fermi momenta and σ, ω and ρ are the expectation values of the meson fields in the absence of kaons (note the gradient terms are zero in the bulk calculation and are included here for completeness). In the phase containing kaons, the meson field equations are modified and consequently their expectation values will change. Therefore, the energy density in the kaon phase due to the nucleon is given by Eq. (3.15), but with different expectation values for σ, ω and ρ meson fields. The contribution to the energy density from the kaon field itself is

$$\epsilon_{\text{kaon}} = \frac{1}{2}f_K^2\left[(\nabla\theta)^2+(m_K^*)^2\theta^2\right] . \tag{3.16}$$

In the absence of gradient terms the kaons do not directly contribute to the pressure as they form an s-wave condensate. However, the attractive interaction between nucleons and kaons lowers the nuclear contribution to the pressure, which is given by

$$\begin{aligned}P &= \frac{1}{3\pi^2}\int_0^{k_F^{(n)}} \frac{k^4\mathrm{d}k}{\sqrt{k^2+{m_N}^{*2}}} + \frac{1}{3\pi^2}\int_0^{k_F^{(p)}} \frac{k^4\mathrm{d}k}{\sqrt{k^2+{m_N}^{*2}}} + \frac{\mu_e^4}{12\pi^2} \\ &+ \frac{1}{2}\left((m_\omega\omega)^2+(m_\rho\rho)^2-(m_\sigma\sigma)^2\right) - U(\sigma) \end{aligned} \tag{3.17}$$

where the meson mean field values (and thus also the nucleon effective mass m_N^*) are affected by the presence of a non-zero θ.

3.3 Surface and Coulomb Effects in the Mixed Phase

A complete description of the mixed phase should include surface and Coulomb contributions to the energy density. The Coulomb energy arises because each of the two phases is electrically charged. If the electric charge densities were small, the size of energetically favored structures would be very large, and the contribution of the surface tension to the overall energy density would become vanishingly small. In our case, however, the electric charge densities are large (comparable to the baryon number densities), resulting in small structures (5-7 fm) for which the surface to volume ratio is large. Consequently the surface tension makes an important contribution to the total energy density.

Unlike in the quark-hadron transition, where the surface tension is poorly known, the surface tension between the kaon and nucleon phases can be calculated within the purview of the model described earlier because the two phases (and hence also boundary region between them) are considered within the same theoretical framework. Before detailing the procedure we adopt in this work, we will briefly review the standard methodology often employed in describing charge-separated mixed phases and calculating surface and Coulomb contributions to the thermodynamics.

3.3.1 Critique of the Bulk Calculation

The bulk calculation of mixed phase thermodynamics, especially in the context of the mixed phase containing nuclei and dripped neutrons, is described in detail in several earlier works [78, 59]. In a recent work, Christiansen, *et al.* [60] have studied the kaon-nucleon mixed phase using similar methods. The basic approach is to impose Gibbs coexistence conditions on the two phases. Diffusive equilibrium across boundaries implies equality of chemical potentials

$$\mu_i^I = \mu_i^{II} \tag{3.18}$$

where the labels I and II simply refer to the two phaes. The subscript i runs through the complete set of conserved charges, e.g., baryon number and electric charge. (A neutrino chemical potential could also be included if one were interested in early-time evolution of the proto-neutron star when lepton number is conserved over short time scales.) Similarly,

thermal equilibrium implies

$$T^I = T^{II} \tag{3.19}$$

although in the present chapter we always assume $T = 0$ so this condition is satisfied automatically. Finally, mechanical equilibrium requires that the pressures on two sides of a boundary are equal:

$$P^I = P^{II}. \tag{3.20}$$

The bulk calculation thus proceeds as follows: At a given baryon chemical potential, the electron chemical potential is adjusted so as to obtain equal pressures in the two phases. This determines the composition of each phase, allowing one to calculate the volume fraction of each phase based on the requirement of global electric charge neutrality. That is, we define the volume fraction of the kaon phase by

$$\chi = \frac{\rho_Q^N}{\rho_Q^N + \rho_Q^K} \tag{3.21}$$

where $\rho_Q^{K,N}$ are the electric charge densities of the kaon and nuclear phases with equal pressure. The various thermodynamic quantities are then determined by volume-fraction-weighted averaging; for example, the energy density can be written as

$$\epsilon = \chi\epsilon_K + (1-\chi)\epsilon_N \tag{3.22}$$

where $\epsilon_{K,N}$ are the total bulk energy densities of the two phases.

In order to account for finite size effects, the bulk energy density (Eq. 3.22) can be supplemented with the inclusion of surface and Coulomb terms. The surface tension coefficient σ_0 is estimated by computing the interface energy between two semi-infinite slabs by explicitly including the gradient terms, as was done for the nuclear-kaon phase boundary in Ref. [60]. Once the surface tension is known, the surface contribution to the energy density for a structure of size R and Wigner-Seitz radius R_{WS} can be approximated by

$$\epsilon_{Surface} = \frac{\chi\sigma_0 d}{R} \tag{3.23}$$

where $\chi = (R/R_{WS})^d$ is the volume fraction of the kaon phase and d is the dimensionality ($d = 3$ for droplets, $d = 2$ for cylinders, and $d = 1$ for slabs). R_{WS} is defined as the radius

which contains zero net electric charge. In the Wigner-Seitz approximation, we calculate thermodynamic properties by averaging over such charge-neutral cells; it is assumed that we can then fill space with such charge neutral cells which, by construction, do not interact. This of course introduces small "edge" errors for the case of spherical or cylindrical cells, since one cannot fill space with these shapes. Such errors, however, are expected to be negligible.

The Coulomb energy is

$$\epsilon_{Coulomb} = 2\pi(\Delta\rho)^2 r^2 \chi f_d(\chi) \tag{3.24}$$

where

$$f_d(\chi) = \frac{2/(d-2)(1-\frac{1}{2}d\chi^{1-2/d})+\chi}{d+2}\,, \tag{3.25}$$

$\Delta\rho = \rho_Q^N - \rho_Q^K$ is the difference in electric charge densities of the two phases [78].

The total energy density is then given by

$$\epsilon = \chi\epsilon_K + (1-\chi)\epsilon_N + \epsilon_{Surface} + \epsilon_{Coulomb}. \tag{3.26}$$

The stable size for geometrical structures is found by minimizing this energy density with respect to variations in the size R. In the usual method, this procedure assumes that the two bulk energy densities ϵ_N and ϵ_K do not vary with R, so that the minimization amounts to making the sum of surface and Coulomb contributions as small as possible. As is well-known, this calculation establishes that the favored size is that which permits $E_{Surface} = 2E_{Coulomb}$ independent of the dimension [78].

The bulk calculation is premised on: (1) pressure equilibrium between the two phases; (2) constancy of the bulk energy densities (and surface tension) as the structure size varies; (3) the neglect of the finite thickness of the phase boundary; and (4) the neglect of modifications to the charged particle distributions due to electrostatic forces (Debye screening). In what follows we address each of these assumptions and show that none of them are valid for the case in study.

First, the assumption of pressure equality cannot hold in general. To see this, assume we have a system that has separated into two phases, with the total energy given by $E = E_1 + E_2 + E_{Surface}$, where $E_{1(2)}$ refers to the energy in phase 1(2). If the surface tension is

not a strong function of the shape of the phase boundary, the surface energy will be given by $E_{Surface} = \sigma_0 A$ where A is the area of the boundary. In equilibrium, the total energy will be minimized with respect to the volume occupied by phase 1, V_1. (The boundary will move and thereby change the volumes occupied by the two phases until the total energy is minimized.) Differentiating the expression for the total energy with respect to V_1 and setting the result to zero gives

$$p_1 - p_2 = \sigma \frac{dA}{dV_1}, \tag{3.27}$$

where $p_1 = -\partial E_1/\partial V_1$ and $p_2 = -\partial E_2/\partial V_2$ are the pressures in the two phases, which are seen to differ by an amount proportional to the surface tension and the derivative of the boundary area with respect to the volume of the rare phase. For the case of slabs, the indicated derivative is zero since the boundary can move back and forth without changing its area. For the case of spherical droplets and cylindrical rods, however, the derivative is proportional to R^{-1} and the pressure difference between the two phases may become large for small structures. The pressure, however, is tied to the other thermodynamic quantities through the usual (zero temperature) relation $\Omega/V = \epsilon - \sum_i \mu_i n_i = -p$. Consequently, the bulk energy density, baryon number density and the chemical potentials cannot remain constant; they change as the size is varied due to changes in the pressure of the kaon phase. Note that a change in the bulk properties of the kaon phase for small structures also necessitates a change in the surface tension, which depends on the integrated gradients between the two phases.

For small structures the finite thickness of the surface region also plays an important role. The thickness of the boundary layer between the two phases is of order 5 fm (as one can see by skipping ahead to Figure 3.2). For structures of about this size, only a very small region at the center obtains the bulk value of the kaon field, that is, the gradient terms in the meson fields are non-zero nearly everywhere in the kaon structure. Thus, for small structures, the assumption of zero boundary thickness overestimates the extent of the bulk kaon region. Any attempt to produce a structure with a radius *smaller* than this thickness will result in dramatic changes to the bulk properties of the rare phase, since the fields don't have room to achieve their usual bulk values at the center of the droplet. Therefore, the

bulk approximation completely breaks down for structures smaller than this size.

Thus assumptions (1-3) of the bulk calculation can only be trusted in the limit of relatively large structures. In order to quantify this statement, we have constructed a sequence of kaon-condensate droplets. by explicitly solving the kaon EOM, having different radii and at a fixed external pressure. Various thermodynamic quantities are then calculated and compared to results obtained in the bulk calculation.

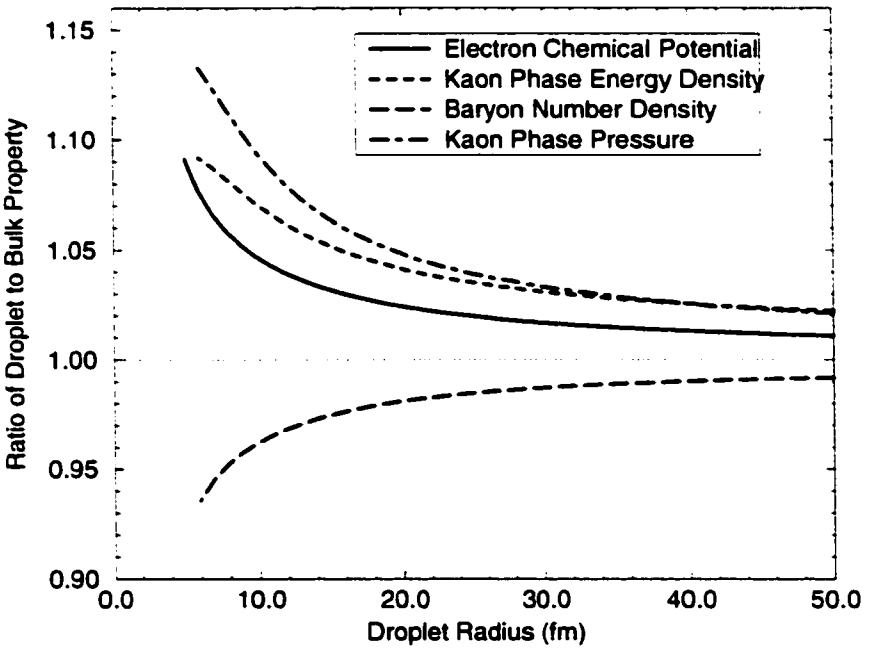

Figure 3.1: Ratio of droplet properties to corresponding bulk properties as a function of droplet radius. The droplets are constructed with the external pressure (pressure in the nuclear phase) held fixed at a value $p = .35\text{fm}^{-4}$.

Fig. 3.1 shows the ratio of droplet properties to bulk-calculation properties as a function of droplet size. As expected, the quantities asymptote to their bulk values in the limit of large droplets, but differ from their bulk values at the 10% level for droplets with radii below about 10 fm. This behavior is typical of small structures, being more pronounced for droplets, less so for rods and is absent for slabs (for the pressure equilibrium reasons

discussed previously). These finite size effects are therefore likely to play an important role in the vicinity of the critical density associated with onset of the mixed phase where the favored structures are droplets. Here, it is important to note that finite size corrections tend to increase the kaon phase energy density and decrease the baryon number density with decreasing radius. This is significant because both of these effects tend to make small droplets energetically less favorable than predicted by the bulk calculation. Also, the increase of the electron chemical potential for small structures near the critical density acts to make the electric charge density of the nuclear phase negative, making it impossible to satisfy the charge neutrality condition, except in the case of unreasonably large structures. Both of these effects suggest that the critical pressure for the transition may be increased from its naive bulk value. This is indeed what we find.

Thus, the first three assumptions above are valid only in the limit of large structures. Assumption (4), however, is known to be valid only for structures smaller than the smallest Debye screening length. (Note that in the previous analysis we neglected screening.) The typical Debye screening length of electrons at the density of interest here is 7-10 fm [108]. For larger droplets the charged particle distributions will readjust to screen the droplet charge. To demonstrate this, we show the particle density profiles for a droplet with fixed total number of kaons, for the two cases: with and without screening included in the equations of motion. To include this effect, we use a relaxation procedure in which we start with an initial guess for the shape of the electric potential in the Wigner-Seitz cell, solve for the kaon EOM to obtain the charged particle profiles, and then recalculate the electric potential using the new profiles. This is then repeated until convergence.

The effect of the electrostatic forces on the particle density profiles is shown in Fig. 3.2. The large negative potential at the center of the droplet tends to push the negatively charged kaons toward the surface region, and the electrons out beyond the surface. The proton distribution follows more closely the changes in the kaon distribution since the strong interaction between the kaons and protons overwhelms the Coulomb effect. Screening becomes more pronounced for droplet radii larger than typical Debye screening length, which in the present case appears to be about 5 fm. Droplets larger than this size are greatly deformed, with the kaons residing mainly on the surface.

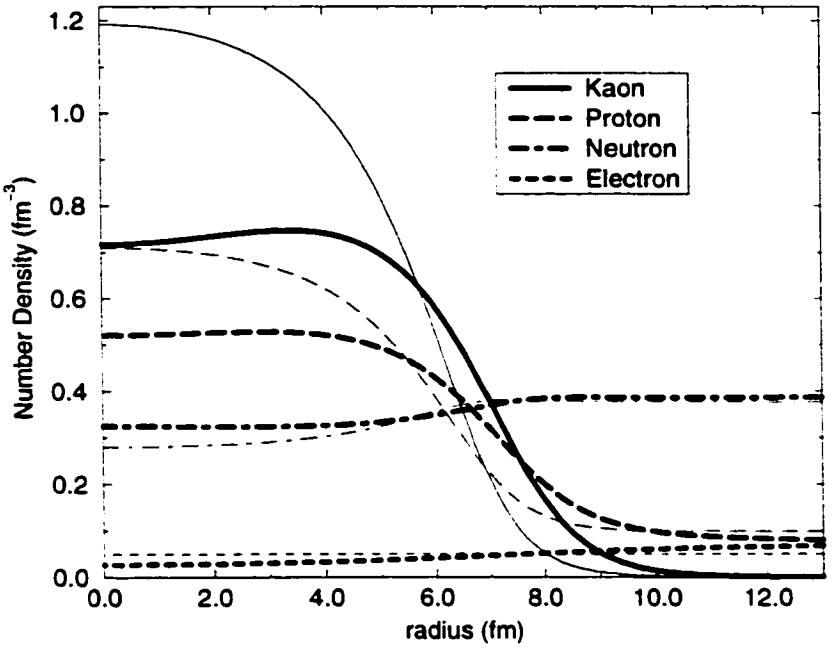

Figure 3.2: Comparison of droplet profiles with and without electron Debye screening. The screened droplet (thick lines) and the unscreened droplet (thin lines) each contain a total kaon number of 1100. The effect of screening is to push many of the kaons near the surface of the droplet and thus greatly reduce the central kaon number density. A similar effect occurs for electrons, although the overall densities are lower. The neutron profile is changed only slightly by screening, while the proton density closely follows the changes in the kaon distribution.

Although this deformation increases the energy density associated with the strong interactions by forcing the fields to take on less than ideal values in the central regions, the overall effect is to significantly reduce the Coulomb energy of the structures. This is essentially as expected. After all, allowing the fields to rearrange themselves in accordance with the electric potential is tantamount to adding a degree of freedom to the system; so it is no surprise that the net effect is for the system to find a way to lower its total energy.

While the deformation due to Debye screening indeed becomes less important for smaller structures, it appears to never become negligible. This is also expected, since the screening

length is approximately the same size as the boundary thickness and it is not possible for structures to become smaller than this thickness without being greatly deformed. The quantitative effects of screening on the energetics and geometry of structures will be discussed further in §4. For now, suffice it to say that one cannot expect *a priori* the effects of Debye screening to be small compared to other finite size effects.

To summarize, the assumptions of the bulk calculation are inconsistent. Some are valid only in the limit of very large structures, while the neglect of screening is plausible only in the opposite limit. Consequently, a description of the mixed phase calls for a more careful treatment. This is main goal of this work. In the what follows we describe the procedure we adopt to calculate the thermodynamics of the mixed phase.

3.3.2 Energy Minimization and Results

Our task here is to determine the ground state configuration of a local region of a neutron star interior at a specified pressure. Consequently, the appropriate thermodynamic potential is $G = E + pV$, the Gibbs potential. With conservation of baryon number, the ground state will minimize the Gibbs potential per baryon:

$$g = \frac{G}{N_B} = \frac{E + pV}{N_B} = \frac{\epsilon + p}{n_B}. \tag{3.28}$$

Here ϵ is the energy density, p is the pressure, and n_B is the baryon number density. Global electrical neutrality is imposed by considering the energy density and baryon number density averaged across a Wigner-Seitz cell containing zero net charge.

The Gibbs free energy per baryon in the kaon mixed phase, computed in the bulk approximation is shown in Fig.3.3. The results shown do not include the the surface and Coulomb contributions. The Gibbs energy of the homogeneous phase containing only nucleons is also shown (solid line). The critical pressure for the onset of the mixed phase is determined by the requirement that the pressure in the two phases be equal, phases be oppositely charged and the Gibbs energy be lower than that of the homogeneous nucleon phase. From the figure we see that this occurs at a pressure $p = 0.28$ fm^{-4}, corresponding to a baryon number density of $n_B = 0.43$ fm^{-3}.

The goal of the present work is to identify the changes that result to this simple picture when finite-size effects are correctly incorporated. In order to include surface and Coulomb contributions, we solve the kaon EOM. We begin with a small value of the kaon field at a finite radius, and then integrate back toward the origin. The chemical potentials are then adjusted until the desired pressure is reached and the kaon field attains zero slope at the origin. The different geometries (spheres vs. cylinders vs. slabs) are implemented by using the appropriate form of the Laplacian operator for that geometry. We omit the effect of Debye screening in what follows; it will be discussed in detail in the next section. The Wigner-Seitz cell size is determined as usual by the requirement of overall charge neutrality.

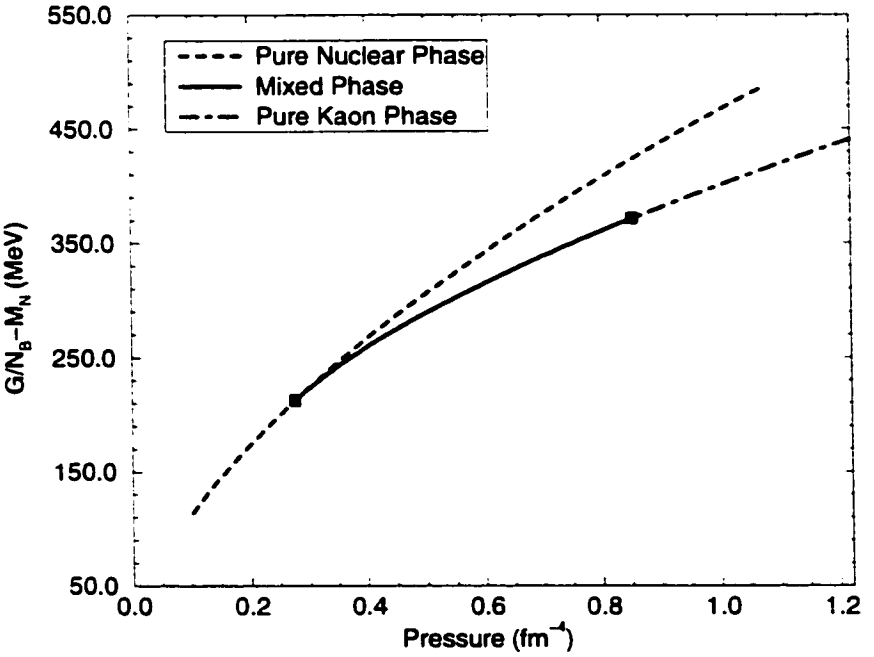

Figure 3.3: Gibbs energy per baryon as a function of pressure for the pure nucleon phase and the kaon mixed phase. The mixed phase is clearly energetically favored over the entire pressure range of its existence, indicated by the two squares. However, the values shown here ignore surface and Coulomb contributions to the energy as well as Debye screening.

The energy density is calculated as in Eq. 3.15 with the gradient terms included. This

allows for exact treatment of the energy associated with the surface and obviates the need to compute the surface tension and curvature coefficients. The Coulomb energy density is $\epsilon_{Coulomb} = \frac{\epsilon_0}{2}|E(r)|^2$ where E is the electric field determined from Gauss' law for the relevant geometry by explicitly integrating the electric charge density up to a given radius. We construct a sequence of droplets/rods/slabs of varying size and study how G/N_B varies with R at fixed pressure. The results are qualitatively as expected. For large structures, the Coulomb energy dominates, while for very small structures the surface energy dominates. At intermediate sizes there is a trade-off which results in a minimum of G/N_B vs. R. This minimum determines the ground state at a given pressure.

Some details of this minimization deserve mention. Because of the variation of the electron chemical potential with structure size (shown in Fig. 3.1), the nucleonic matter outside of the kaon-condensate structure sometimes becomes negatively charged for small structures. This occurs for pressures just above the bulk critical pressure, where the bulk approximation predicts a nucleonic phase with small positive charge. If both phases become negatively charged, however, no Wigner-Seitz cell can be defined, and the structure in question is ruled out. Thus the requirement of overall electric charge neutrality (and the imposition of correct mechanical equilibrium) forbids the existence of reasonably-sized structures at pressures just above the bulk critical pressure.

The Gibbs energy per baryon is plotted as a function of pressure for the three different geometries in Fig. 3.4. Note that the values are shown relative to the Gibbs energy of the pure nuclear phase. As expected, there is a smooth transition between the relative favorability of drops (which are preferred at lower pressures) to rods and slabs as the pressure is increased. Although we do not construct them explicitly here, this sequence is expected to continue in the usual way through anti-rods and anti-drops in which the nuclear phase becomes the rare phase. The significant feature of our result is the comparison of the structures to the Gibbs energy per baryon of electrically neutral pure nucleon matter. Just above the critical pressure, where droplets are the favored geometry and therefore will be present according to the bulk calculation, we find that the Gibbs energy is lower in the nucleonic phase than in the mixed phase. This remains the case over a wide range of pressures, until droplets finally become favorable relative to pure nuclear matter at a

pressure about 50% higher than the bulk calculation value of the critical pressure, nearly .40 fm^{-4} instead of .28 fm^{-4}. At a slightly higher pressure, rods and subsequently slabs take over as the energetically favored geometry.

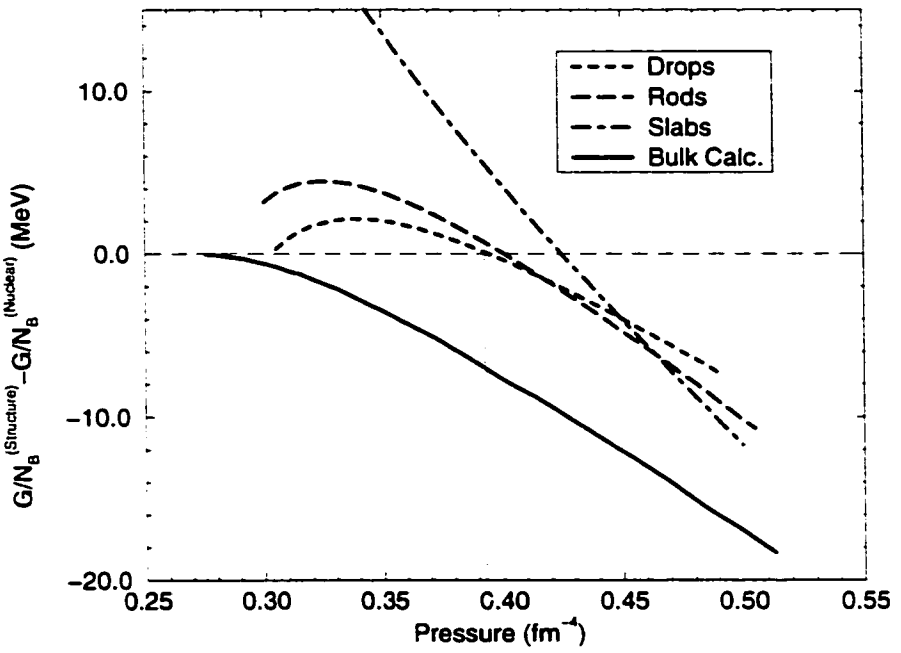

Figure 3.4: Gibbs energy per baryon as a function of pressure for droplets, rods, and slabs. The energy is measured relative to the Gibbs energy per baryon of pure nuclear matter at the same pressure; hence, a given geometric structure is favored only when it lies below zero. The bulk calculation (neglecting surface and Coulomb effects) is included for comparison. Note the change in value of the critical pressure (i.e., the pressure marking the onset of a mixed phase), indicated here by two vertical lines for the old and new values. Note also that these results omit the effects of Debye screening, which will be discussed shortly.

The reason for the curvature in the droplet and rod energy at low pressures involves electric charge neutrality, as discussed previously. At these low pressures, the variation of the structure size necessitates a change in the electro-chemical potential. This change then results in the nucleonic matter outside the kaon region becoming less and less positively charged. At some minimum size, the matter outside becomes uncharged, and the Wigner-

Seitz radius becomes infinite and the kaon filling fraction goes to zero. In general, as the structure size is reduced at constant pressure, the kaon phase volume fraction approaches zero, and the Gibbs energy approaches (from above) its value for pure electrically neutral nucleonic matter at the same pressure. So although the mixed phase energy appears to come close to the pure nucleon phase values near the bulk critical pressure, a mixed phase is never in fact favored at these low pressures.

The striking result that we find here is the significant increase in the critical pressure at which the mixed phase becomes favorable. Qualitatively, this increase in the critical pressure should be expected since the bulk calculation neglected the surface and Coulomb energies. An increase in the critical pressure will make the equation of state stiffer over this range and correspondingly the maximum mass of the neutron star will increase. In addition, the radial extent of the mixed phase in the interior will be significantly reduced.

3.4 Debye Screening

The qualitative effect of Debye screening on the radial dependence of the particle densities was shown in Fig. 3.2. Charged particle profiles had to readjust quite significantly to lower the coulomb energy. Clearly, the effect of the deformation of particle profiles caused by screening is to increase the hadronic part of the energy density associated with the structure. This must occur because the fields no longer take on their optimal values over a sizable region of the structure. The net effect of screening, however, is to lower the total energy, since the reduction in the Coulomb energy due to screening is larger than the cost in hadronic energy associated with the deformation.

The quantitative effect of screening on the Gibbs energy are shown in Fig. 3.5. The results illustrate the importance of the Coulomb energy relative to other contributions. For example, the differences in Gibbs energies among unscreened droplets of different sizes are small compared to the differences between unscreened droplets and screened droplets of any size. Screening also results in a qualitative change in the radius dependence of the Gibbs free energy. The Gibbs free energy of the screened droplets decreases with increasing radius for small to intermediate size droplets.

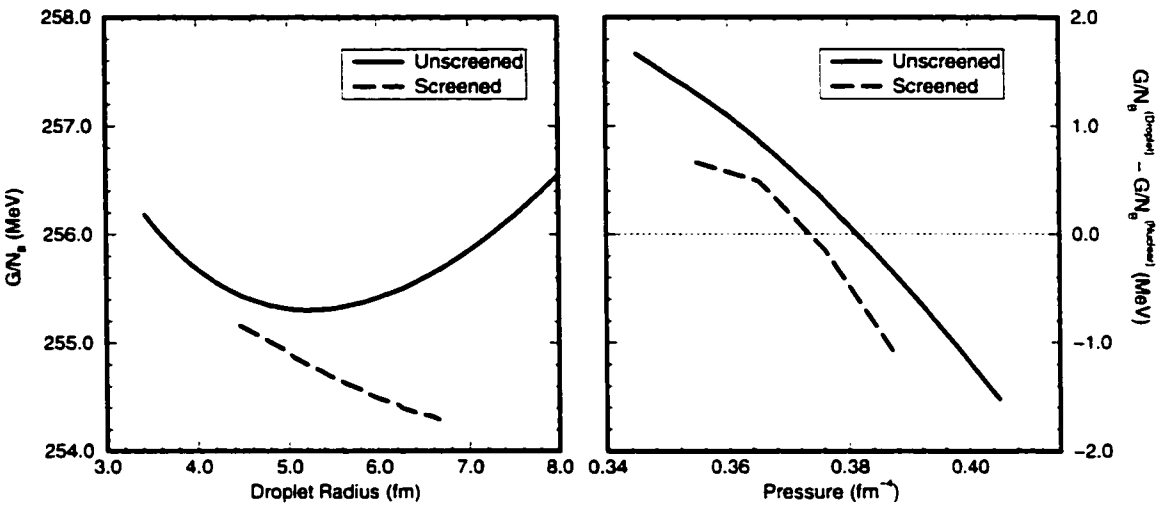

Figure 3.5: Gibbs energy per baryon as a function of droplet radius, for different amounts of screening. The screening is controlled by shifting the electrochemical potential at each radius by a fraction of the true electric potential. By turning on the screening slowly, one clearly sees the qualitative effect of the overall energy per baryon being lowered due to the reduction in Coulomb energy.

How are the results of the previous section affected by screening? To answer this, we must first point out another qualitative effect of screening which again involves electrical charge neutrality. As shown in Fig. 3.2, Coulomb forces tend to repel the negatively charged electrons away from the kaon droplet. Whenever the Wigner-Seitz radius is large (which can happen either when the kaon structure itself is large, or when the kaon filling fraction is low) this repulsion results in an over-abundance of electrons in the region outside of the kaon structure. But as before, once the electric charge density of the nucleonic phase becomes negative, it is no longer possible to define a Wigner-Seitz cell, and the structure under consideration is forbidden.

We find that precisely this problem occurs for all droplets below a pressure of about $P \sim .35 fm^{-4}$. The previous analysis (including other finite size effects but ignoring screening) allowed Gibbs conditions to be satisfied in this pressure range; the mixed phase was simply not energetically favored. The inclusion of screening effects shows that no equilibrium structures can exist at all in this pressure range. Above $P \sim .35 fm^{-4}$, where it is possible

to construct a fully screened globally electrically neutral droplet, the Gibbs energy per baryon is indeed lowered somewhat from the values plotted in Fig.3.4. This results in the critical pressure decreasing slightly from the new value quoted earlier, but the change here is small. The first fully screened structure we can produce with Gibbs energy per baryon below that of the pure nucleonic phase occurs at a pressure of .375 fm^{-4} (compare this with the critical pressure $\sim$ 0.385 fm^{-4} when Debye screening was ignored). Thus, while the Debye screening can have large effects on the particle density profiles, it has a relatively small effect on the free energy density (less than one MeV per baryon), as can be seen in the right panel of Fig. 3.5. Consequently the results of the previous section remain qualitatively unchanged: the inclusion of finite-size effects significantly increases the critical pressure for transition to a mixed phase.

Because the changes in Coulomb energy associated with screening are large compared to the energy differences between various geometries at a given pressure, screening will also play a dominant role in the determination of structures that are preferred at a given pressure. The qualitative feature of droplets being replaced by rods (and subsequently slabs) as the pressure is increased is expected to remain. But the particular pressures at which the transition from one geometry to the next occurs may vary from the picture of Fig.3.4. Thus, if one is only interested in the long wavelength thermodynamic properties of the system, it is safe to ignore Debye screening. However, to describe the mixed phase in more detail, i.e. specify the particle profiles and the geometries that are favored at a given pressure, Debye screening must be accounted for.

3.5 Neutron Star Properties

The equation of state determines the neutron star structure through the Tolman-Oppenheimer-Volkov (TOV) equation:

$$\frac{dp}{dr} = -\frac{[p(r) + \epsilon(r)][M(r) + 4\pi r^3 p(r)]}{r(r - 2M(r))} \tag{3.29}$$

where p is the pressure, ϵ is the energy density, and

$$M(r) = 4\pi \int_0^r \epsilon(r) r^2 \mathrm{d}r \tag{3.30}$$

is the total mass enclosed at radius r. The solution to the TOV equation are shown in Fig. 3.6 for three cases: pure nuclear matter, the bulk calculation of the mixed phase, and a calculation of the mixed phase as described in this work which properly accounts for surface and coulomb energy. The left panel of the figure shows the variation of the total gravitational mass as a function of the central pressure. We find that the maximum neutron star mass is increased by about $0.1 M_{\odot}$ relative to the bulk calculation of the mixed phase. This is as expected since the critical pressure for the transition was shown to increase due to the finite size effects. The distribution of mass and internal composition of the star for a given value of the central pressure are shown in the right panel. The dashed lines show results for the case where finite size effects are included; this is to be contrasted with the results obtained in the bulk approximation shown by the solid curve. The spatial extent of the mixed phase region is also influenced by finite size effects. The extent of the mixed phase region in the inner core is shown for both cases and indicates that the finite size effects cause the mixed phase region to shrink. It must however be noted that we are comparing the structure of stars with different gravitational mass but the same central pressure.

Transport properties in a mixed phase can differ greatly from those of uniform matter since the mixed phase allows for new processes that cannot occur in a translationally invariant system. Finite size effects play a central role in the determination of the transport characteristics of a heterogenous phase since they depend sensitively on the composition, size and geometry of the structures present. In what follows we briefly discuss a few examples of transport process which are strongly influenced by the finite size effects.

In a recent article, it was shown that low energy neutrinos couple coherently to the droplet structures and consequently the neutrino mean free path in a mixed phase was greatly reduced [61]. The neutrino scattering rate depends on the total weak charge (assuming the droplet size is small compared to the wavelength $1/k_{\nu}$ of the neutrino), and on the filing fraction. The cross section for the coherent neutrino-droplet scattering varies as the square of the total weak charge. Thus, the neglect of screening effects alone, which could overestimate the weak charge in a droplet by as much as $30-50$ % (see Fig.3.5), could result in a mean free path estimate that was smaller by $50-75$ %. Furthermore, coulomb correlations between droplets decreases the net neutrino scattering rate when the $E_{\nu} < 1/d$,

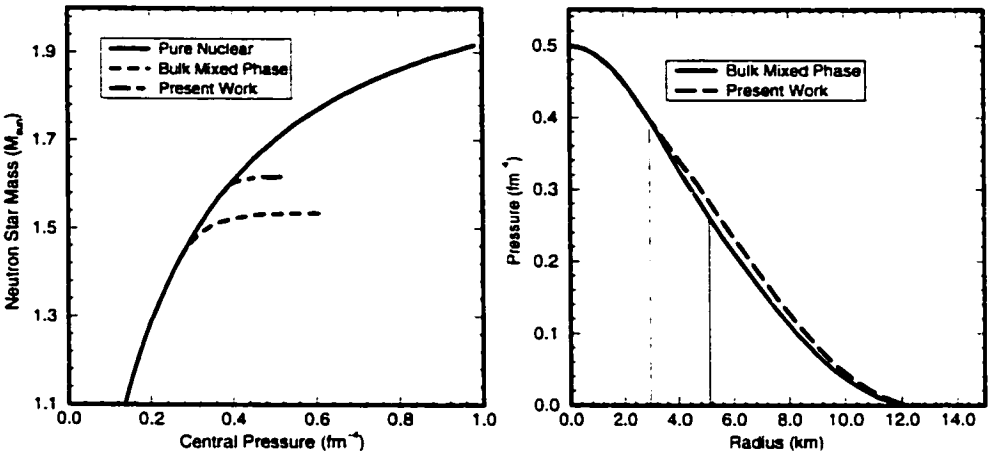

Figure 3.6: Mass as a function of the central pressure for a pure nuclear equation of state, the bulk mixed calculation without finite-size effects, and the realistic calculation of the present work. A correct treatment of surface and Coulomb energies increases the critical pressure for the realization of the mixed phase, and the neutron star maximum mass by $\sim 0.1 M_{\odot}$. The right panel compares the internal structure of a star with and without finite size corrections included in a description of the mixed phase. The vertical lines indicate the outer edge of the mixed phase for the two descriptions.

where $d = 2R_{WS}$ is the inter-droplet spacing. Again, an accurate description of finite size and Debye screening effects is required to calculate the neutrino mean free path in the mixed phase [61]. The filling fraction of the kaon phase, denoted by χ, at a pressure $p = 0.40$ fm^{-4} in the bulk approximation is $\chi_{bulk} = 0.23$ while the more detailed treatment yields $\chi = 0.13$. Again, this substantial change is due to the increase of the electron chemical potential for small droplets.

The results of this work will also influence calculations of the melting temperature of the lattice of droplets. This becomes obvious when we note that the electric charge distributions are strongly modified. In addition, our findings here affect the location and the nature of the interface between the solid-mixed phase and the liquid-nuclear phase. The physics of this interface has been shown to play an important role in damping r-mode instabilities in cold and rapidly rotating neutron stars [62]. In general, since the transport characteristics depend primarily on the size and distance between structures, this calls for a detailed description of the mixed phase wherein screening and finite surface effects are incorporated.

In particular, studies of the early evolution of neutron stars [63], where neutrino transport plays an important will be strongly influenced by finite size effects discussed here.

3.6 Discussion

The earliest papers on first-order kaon condensation in neutron stars ignored finite size effects such as surface and Coulomb energies. Since then, these effects have been introduced into calculations by assuming that certain quantities remain fixed as the physical size of geometric structures is varied. By explicitly constructing these structures, however, we have shown these assumptions to be unwarranted. In particular, the energy densities, number densities, and chemical potentials vary at the 10% level as the size is reduced toward the boundary thickness. These changes in the bulk properties of the two phases preclude the possibility of determining the most stable structures by minimizing only the surface and Coulomb contributions to the energy. By including these effects correctly, we find that the critical pressure for the onset of the mixed phase is increased dramatically, with the further consequence that the maximum neutron star mass is increased back toward its value for the pure nuclear equation of state.

Clearly, we have not accounted for all finite size effects that arise in the mixed phase. We examine some assumptions of our work here and comment on corrections omitted. The calculations presented here were based on the Thomas-Fermi approximation for the nucleon fields, which we expect to be valid based on our observation that the average nucleon density is large compared to the size of the density gradients [64]. The Wigner-Seitz approximation could in principle introduces corrections to the filling fraction. However, we expect these corrections to be most important at large filling fraction where the Wigner-Seitz description is accurate because the favored geometry is planar. In addition a careful treatment of the nucleon fields would introduce shell effects that may be important for small structures. These effects have been neglected here since we expect their contributions to the Gibbs potential to be small (typically, we expect that $\delta E_{shell} \sim A^{1/6}$ compared to A^1 or $A^{2/3}$ dependence of volume and surface contributions, where A is the total baryon number of the droplet).

The increase in the critical pressure will also reduce the radial extent of the mixed phase. This will potentially affect our pictures of neutrino transport, glitches, r-mode instabilities, and other issues involved in neutron star structure and viscosity calculations. Additionally, as pointed out by Heiselberg, Pethick and Staubo [108], the mixed phase may not be realized in practice if the nucleation time is too large, even if the mixed phase is energetically favored. Our work here gives a hint in that direction: correct inclusion of surface and Coulomb energies dramatically reduces the energetic favorability of the mixed phase over a wide range of pressures. This increase in energy, however, necessarily applies not only to the stable structures of $5-6$ fm, but also to the smaller transitional structures which must be passed through in the process of nucleation. In short, our work suggests that the energy barrier to nucleation may be somewhat higher than previously thought, resulting in an increase of the expected time required for the phase transition to occur.

The apparent experimental observation of relatively high-mass neutron stars (as discussed in Chapter 1) has been cited as evidence that kaon condensation does not occur in neutron stars. We hypothesize a different interpretation which appears to be consistent with these high-mass observations. A sufficiently heavy proto-neutron star (PNS) may undergo a kaon-condensate phase transition due to thermal nucleation while it is still relatively hot. This will of course soften the equation of state and perhaps lead to gravitational collapse of a massive PNS to a black hole [65]. In contrast, a PNS which is insufficiently massive, on the other hand, will not achieve the critical density for kaon-condensation and will therefore cool in the standard way. If it subsequently acquires mass through accretion the low temperature may preclude the possibility of forming a kaon-condensed mixed phase, even if the central pressure exceeds the critical pressure for the transition. The energy barrier to nucleation via quantum tunneling would simply be too high, and the neutron star could exist in a metastable state for a long time. This (for now hypothetical) scenario would explain how the observation of high-mass neutron stars (in excess of the maximum mass allowed by the kaon mixed-phase equation of state) may not contradict the existence of kaon condensation; these high-mass stars would need only to have acquired a part of their mass through accretion after cooling, which appears in fact to be likely. In any case, further examination of the time scale for nucleation of kaon-condensate droplets is clearly interesting;

it will be studied in some detail in the following chapter.

Finally, it should be pointed out that the relevance of these issues is not restricted to the case of kaon condensation only. Any first-order phase transition that occurs in neutron stars will share the same qualitative properties. Hence, it is reasonable to suggest that a correct inclusion of finite size effects in the deconfinement transition will have similar results to the ones we have shown here, i.e., an increase in the critical pressure and a possible increase in the nucleation time allowing for metastability.

In Appendix A, we develop some formal technology for understanding the rate at which droplets of kaon-condensed matter might begin to appear once the critical density for the onset of the phase transition is exceeded. In Chapter 4, we will apply this technology to the model discussed here, and thus address the issue of whether, when, and how fast the kaon-condensed phase appears during the formation of a neutron star.

Chapter 4

STRANGENESS NUCLEATION IN NEUTRON STAR MATTER

In this chapter,[1] we study the transition from npe-type nuclear matter (consisting of neutrons, protons, and electrons) to matter containing strangeness, using a Walecka-type model predicting a first-order kaon-condensate phase transition. We examine the free energy of droplets of K-matter as the density, temperature, and neutrino fraction are varied. The nucleation rate theory developed in Chapter 4 is then used to approximate the rate at which critical droplets of the new phase are produced by thermal fluctuations, thus giving an estimate of the time required for the new (mixed) phase to appear at various densities and various times in the cooling history of the proto-neutron star. We also discuss the famous difficulty of "simultaneous weak interactions" [40] which we connect to the literature on non-topological solitons. Finally, we discuss the implications of our results to several phenomenological issues involving neutron star phase transitions.

4.1 Introduction

A 'hot' topic recently in nuclear physics has been the attempt to understand the production of strangeness in the expanding plasma thought to be created in relativistic collisions of heavy ions. There are several aspects to this complex and difficult problem, including: how (and, indeed, whether) a 3-flavor deconfined quark-gluon plasma is produced by the initial collision; how this strange matter equilibrates, expands, and cools; and how it eventually re-hadronizes, hopefully giving rise to a unique observable signal. The goal of these studies is to better understand the phase structure of QCD in the low-density, high-temperature region of the phase diagram.

A different but complementary problem involves the study of nuclear matter at high-

[1]The reader unfamiliar with the general topics of nucleation and metastable state decay is referred to Appendix A for an overview.

density and low temperature, such as that existing in neutron star interiors. Here, matter consisting of neutrons, protons, and electrons (npe matter) is crushed during the gravitational collapse of the parent star. (Actually, what we call npe matter in this paper may also include muons and neutrinos.) As the star collapses, weak interactions convert electrons and protons into neutrons, with electron neutrinos produced copiously as a by-product. Additionally, neutrinos of all flavors are created through brehmstrahlung-type collisions among the warm nucleons. As the neutrinos diffuse outward and radiate away, the proto-neutron star cools from an initial temperature of several tens of MeVs, and eventually settles into the familiar ground state of a neutron star with central density several times nuclear matter density.

It is now understood that at sufficiently high density, a phase transition will occur in which the neutrons and protons of npe matter are replaced by deconfined quarks (including strange quarks) [39, 40, 71]. A related mechanism for the appearance of strangeness in neutron star matter is kaon condensation, which may become possible at densities somewhat lower than the density required for the deconfining transition described above. The possibility of kaon condensation was first pointed out by Kaplan and Nelson, who were motivated by the chiral Lagrangian prediction of an attractive interaction between K^- and nuclear matter [45].

Intuitively, one can understand the phenomenon of kaon condensation in the following way. As the density of npe matter is increased, and assuming that all particle species are in equilibrium with respect to the weak interactions, the electron chemical potential increases. Simultaneously, the effective mass of an in-medium K^- will decrease, due to the attractive interaction mentioned above. Therefore, at some critical density, the electron chemical potential becomes greater than the effective mass of the K^-. It then becomes energetically favorable for the high-energy electrons to decay according to

$$e^- \rightarrow \nu_e + K^- \tag{4.1}$$

at which point a condensate of K^- will form.

This picture is somewhat over-simplified, as the production of kaons does not proceed exclusively by the decay of energetic electrons, but may also occur via fully-hadronic weak

couplings, e.g., $n \rightarrow p + K^-$. Also, the notion of a uniform condensate of kaons is probably wrong. As pointed out by Glendenning [47], the presence of two separate conserved charges in neutron star matter (namely, baryon number and electric charge) gives rise to the possibility of a mixed phase of N-matter and K-matter existing over a wide range of densities and pressures in the star. (By "N-matter" we mean matter not containing kaons, but without the restriction of charge neutrality implied by "npe matter".) This mixed phase will have the form of a Coulomb lattice – the now standard "pasta" structure consisting of droplets of the new phase immersed in a background of N-matter (at low densities), with rods and slabs replacing droplets as the density is increased, and finally with the role of the two phases interchanging in the transition toward homogenous K-matter as the density is increased still further [49].

In this chapter, we again assume a model which predicts just this kind of first-order phase transition to kaon-condensed matter. For the description of nuclear matter, we use a Walecka-type model in which the interactions of strongly-interacting particles are mediated by σ, ω, and ρ mesons, treated in the mean-field approximation. Kaons are included in the model on the same footing as the nucleons, as described in the next section.

Our goal is, however, not to study the structure of the ground state predicted by this model (and its subsequent effect on the global neutron star properties such as the mass-radius relation), but rather to study the *nucleation* of kaons, that is, the process by which the initial proto-neutron star matter with zero strangeness acquires strangeness through the spontaneous appearance of K-matter droplets. We will begin this study by using the theory of homogenous nucleation due originally to Langer [67] and reviewed in the previous chapter. Here one assumes that at a given temperature, there are constant fluctuations producing small short-lived droplets of the new phase. Below a certain critical size, the surface energy cost of these droplets wins out over the volume term and the droplets shrink away. For some critical size, however, the free energy gained from the production of a large volume of the new (energetically favored) phase is just large enough to cancel the cost of surface energy, and the droplet will spontaneously grow. In the case studied here, because the two phases have non-zero electric charge densities, there is also a Coulomb term in the free energy, which becomes large for large droplets. Hence, a super-critical droplet will not

grow forever, but will reach a stable size at which the energy gain between the volume and surface energies just balances the energy cost of the Coulomb energy.

As we saw in the previous chapter, the expected time needed for this kind of phase transition to proceed depended on the probability of a critical droplet being produced by thermal fluctuations, and also on the growth rate of such a critical droplet along the unstable direction in configuration space. Assuming a thermal distribution of these fluctuations, the nucleation rate per unit volume can be written

$$\Gamma \sim I_0 e^{-\Delta F(R_{crit})/T} \tag{4.2}$$

where $\Delta F(R_{crit})$ is the excess free energy of a critical droplet, T is the temperature, and I_0 (the "prefactor") is a microscopic fluctuation rate related to the growth rate of a super-critical droplet, the thermal conductivity of the medium, and other properties [67, 68, 72]. The prefactor is often approximated by dimensional analysis as simply $I_0 \sim T^4$. We will discuss this approximation later. Our goal is to apply this nucleation rate theory to the case of cooling proto-neutron star matter in order to better understand exactly when, where, and how the transition from npe-type matter to the kaon-condensed phase occurs.

Our work generally follows previous work on the nucleation of quark matter droplets in neutron star matter, which has been studied extensively [70, 73, 74, 75]. The case of kaon condensation is physically unique, however, since it is the only realistic proposed example of a direct first order transition from npe-type neutron star matter to matter containing strangeness. In the case of the deconfinement transition mentioned above, for example, and even at densities, temperatures, and pressures for which 3-flavor quark matter is energetically favored, the transition is likely indirect in the following sense: an intermediate stage of 2-flavor quark matter will be produced first, with strange quarks then slowly appearing during a smooth crossover or second-order transition to the 3-flavor ground state. This latter transition is, of course, slow due to the weakness of the weak interactions. In this scenario, however, the original nucleation events which take one from npe matter to deconfined quark matter, need not involve the weak interactions at all.

The case of kaon condensation is radically different, since here there is no intermediate zero-strangeness state which might allow for fast nucleation followed by a slow but smooth

growth of the strangeness-containing fields. Instead, the thermal fluctuations responsible for nucleation events must directly involve the weak-interaction processes which produce kaons. The difficulties posed by the widely varying timescales involved in these two sorts of processes (thermal fluctuations and weak interactions) will form the theme of our discussion.

The outline of the rest of the chapter is as follows. In Section 4.2 we present the details of the nuclear mean field theory used for the subsequent discussion. (This is somewhat repetitive of material in Chapter 3; it is left in here to preserve the autonomy of the chapters, and also because a few details are treated differently in the present discussion.) In Section 4.3 we use this model to extract information about the free energy of K-matter droplets of different sizes, as the background baryon number density and temperature are varied. This allows us to use Eq. 4.2 to estimate the nucleation rate for the kaon-condensate phase transition. In Section 4.4 we discuss in more detail the underlying mechanism for the fluctuations which produce the nucleation, and thereby analyze the trustworthiness of the estimates. Here we also make contact with the literature on Q-balls and argue that the problem of direct strangeness nucleation in neutron star matter may be profitably considered as an instance of Q-ball nucleation. Finally, in Section 4.5 we summarize the findings, discuss the relevance of our results to phenomenological issues in neutron star physics, and indicate some proposals for future investigation.

4.2 Mean-Field Theory Description of Kaon Condensation

In this section we briefly review the model proposed by Glendenning and Schaffner-Bielich [49] which predicts a first-order transition from nuclear matter to the kaon-condensed phase. The model begins with a relativistic Walecka-type Lagrangian describing the neutron and proton fields, as well as the σ, ω, and ρ mesons which mediate their interactions:

$$\begin{aligned}\mathcal{L}_N &= \overline{\Psi}_N\Big(i\gamma^\mu\partial_\mu - m_N^* - g_{\omega N}\gamma^\mu V_\mu - g_{\tau N}\gamma^\mu\vec{\tau}_N\cdot\vec{R}_\mu\Big)\Psi_N \\ &\quad + \frac{1}{2}\partial_\mu\sigma\partial^\mu\sigma - \frac{1}{2}m_\sigma^2\sigma^2 - U(\sigma) - \frac{1}{4}V_{\mu\nu}V^{\mu\nu} \\ &\quad + \frac{1}{2}m_\omega^2 V_\mu V^\mu - \frac{1}{4}\vec{R}_{\mu\nu}\cdot\vec{R}^{\mu\nu} + \frac{1}{2}m_\tau^2\vec{R}_\mu\cdot\vec{R}^\mu, \qquad (4.3)\end{aligned}$$

where $m_N^* = m_N - g_{\sigma N}\sigma$ is the nucleon effective mass, which is reduced compared to the free nucleon mass due to the scalar field σ. The vector fields corresponding to the omega and rho mesons are given by $V_{\mu\nu} = \partial_\mu V_\nu - \partial_\nu V_\mu$, and $\vec{R}_{\mu\nu} = \partial_\mu \vec{R}_\nu - \partial_\nu \vec{R}_\mu$ respectively. Ψ_N is the nucleon field operator with $\vec{\tau}_N$ the nucleon isospin operator.

In addition to the usual kinetic, mass, and interaction terms for the nucleon and meson fields, the model also includes cubic and quartic self-interactions of the σ field:

$$U(\sigma) = \frac{1}{3} b m_N (g_{\sigma N}\sigma)^3 + \frac{1}{4} c (g_{\sigma N}\sigma)^4 \tag{4.4}$$

where b and c are dimensionless coupling constants. These coupling constants (as well as the three nucleon-meson couplings: $g_{\sigma N}$, $g_{\omega N}$, and $g_{\tau N}$) are chosen to reproduce the empirical properties of nuclear matter at saturation density. [35, 3]

Kaons are included in the model as in the previous chapter, by introducing a kaon Lagrangian:

$$\mathcal{L}_K = (\mathcal{D}_\mu K)^\dagger (\mathcal{D}^\mu K) - m_K^{*2} K^\dagger K \tag{4.5}$$

where K denotes the isospin doublet kaon field. As before, we fix the kaon-sigma coupling constant by imposing $U_K(n_0) = 120MeV$. While the physics discussed in this chapter relies on the existence of a first-order transition, the qualitative conclusions are generally independent of the specific value of the coupling. So long as the transition is first-order, the main effect of changing $U_K(n_o)$ will be to change the critical density for the onset of the mixed phase, without severely affecting our discussion of the nucleation properties near this critical density.

The model as presented so far is a complicated, strongly interacting field theory which cannot be solved in any reasonable way. It is therefore standard to make a mean-field approximation, in which the meson field operators are replaced by their expectation values. Because of rotational invariance only the time-component of the vector fields V_μ and $\vec{R}_\mu$ can have a non-zero expectation value. Likewise, only the isospin 3-component of the isovector field $\vec{R}_\mu$ can be non-zero. The equations of motion for the meson (mean-) fields can be simply derived from the above Lagrangians and are given by:

$$m_\sigma^2 \sigma = -\frac{dU}{d\sigma} + g_{\sigma B}(n_n^{(s)} + n_p^{(s)}) + g_{\sigma k} m_K^* f_K^2 \theta^2 \tag{4.6}$$

$$m_\omega^2 \omega = g_{\omega N}(n_n + n_p) - g_{\omega K} f_K^2 \theta^2 (\mu_K + g_{\omega K}\omega + g_{\tau K}\tau) \quad (4.7)$$

$$m_\tau^2 \tau = g_{\tau N}(n_p - n_n) - g_{\tau K} f_K^2 \theta^2 (\mu_K + g_{\omega K}\omega + g_{\tau K}\tau) \quad (4.8)$$

where the meson fields σ, ω, τ now represent the appropriate mean values. Here n_n and n_p represent the neutron and proton number densities, respectively, while $n_n^{(s)}$ and $n_p^{(s)}$ are the corresponding scalar densities. We have substituted $K = (0, K^-)$ and $K^- = \frac{1}{\sqrt{2}} f_K \theta e^{-i\mu_K t}$, where f_K is the kaon decay constant and θ is a dimensionless kaon field strength parameter. We have neglected to write down the additional small contributions to the kaon-coupling terms due to finite temperature effects, though these are included in our code. (See Ref. [76] for a more explicit presentation of the details of this model for finite temperature.) We will be working in the bulk approximation (in which the meson fields do not vary with position) and so have set to zero the gradient terms which would otherwise appear in the equations of motion.

The equation of motion for the kaon field (in terms of θ) is

$$0 = \left((m_K{}^*)^2 - (\mu_K{}^*)^2 \right) \theta \quad (4.9)$$

which indicates that the kaon effective mass $m_K^* = m_K - g_{\sigma K}\sigma$ and the effective chemical potential $\mu_K^* = \mu_K + X$ must be equal in order for the kaon field to take on a non-zero value. Here $X = g_{\omega K}\omega + g_{\tau K}\tau$ is the vector field contribution to the K^- energy. We also include a Langrangian describing non-interacting spin-$\frac{1}{2}$ particles to account for the presence of electrons, muons, and neutrinos.

The thermodynamic potential per unit volume for the nucleon sector is

$$\begin{aligned} \frac{\Omega_N}{V} &= \frac{1}{2} m_\sigma^2 \sigma^2 + U(\sigma) - \frac{1}{2} m_\omega^2 \omega^2 - \frac{1}{2} m_\tau^2 \tau^2 \\ &\quad -2T \sum_{i=n,p} \int \frac{\mathrm{d}^3 k}{(2\pi)^3} \ln \left(1 + e^{(E(k) - \nu_i)/T} \right) \end{aligned} \quad (4.10)$$

where the nucleon energy $E(k) = \sqrt{k^2 + m_N^{*2}}$. The chemical potentials are given by $\mu_p = \nu_p + g_{\omega N}\omega + \frac{1}{2} g_{\tau N}\tau$ and $\mu_n = \nu_n + g_{\omega N}\omega - \frac{1}{2} g_{\tau N}\tau$.

The other thermodynamic quantities can be calculated from Ω_N in the standard way. The nucleonic contribution to the pressure, for example, is $P_N = -\Omega_N / V$, while the number

densities and entropy densities are given by

$$\begin{aligned} n_{n,p} &= -\frac{\partial \Omega_N/V}{\partial \mu_{n,p}} \\ &= 2\int \frac{\mathrm{d}^3k}{(2\pi)^3} f_F(E(k)-\nu_{n,p}) \end{aligned} \tag{4.11}$$

$$s_{nuclear} = -\frac{\partial \Omega_N/V}{\partial T} \tag{4.12}$$

$$\tag{4.13}$$

where $f_F(\epsilon) = \left(e^{-\epsilon/T}+1\right)^{-1}$ is the Fermi-Dirac distribution function. The neutron and proton scalar densities which enter in the equation of motion for the σ field are given by

$$n^{(s)}_{n,p} = 2\int \frac{d^3k}{(2\pi)^3}\frac{m^*_N}{E(k)} f_F(E(k)-\nu_{n,p}) \tag{4.14}$$

The energy density is determined through the usual relation $Ts_N = \epsilon_N + P_N - \sum_i \mu_i n_i$ to be

$$\begin{aligned} \epsilon_N &= \frac{1}{2}m_\sigma^2\sigma^2 + U(\sigma) - \frac{1}{2}m_\omega^2\omega^2 - \frac{1}{2}m_r^2 r^2 \\ &\quad +2\sum_{i=n,p}\int \frac{\mathrm{d}^3k}{(2\pi)^3} E(k) f_F(E(k)-\nu_i) \\ &\quad + \sum_{i=n,p} n_i(\mu_i - \nu_i). \end{aligned} \tag{4.15}$$

The thermodynamic potential for the lepton species present (electrons, muons, and neutrinos) is given by

$$\frac{\Omega_L}{V} = -\sum_l T g_l \int \frac{\mathrm{d}^3k}{(2\pi)^3}\left[\ln\left(1+e^{-(E_l(k)-\mu_l)/T}\right) + \ln\left(1+e^{-(E_l(k)+\mu_l)/T}\right)\right] \tag{4.16}$$

where μ_l denotes the chemical potential for lepton species l, and g_l are the spin-degeneracies: $g = 2$ for electrons and muons, $g = 1$ for neutrinos. β-equilibrium requires the following constraints on the chemical potentials:

$$\mu_K = \mu_e - \mu_{\nu_e} = \mu_n - \mu_p = \mu_\mu - \mu_{\nu_\mu} \tag{4.17}$$

The lepton contributions to the pressure, energy density, and entropy are determined from Eq. 4.16 in the usual way.

Finally, the thermodynamic potential for the kaons is given by

$$\begin{aligned}\frac{\Omega_K}{V} &= \frac{1}{2}f_K^2\theta^2\left[(m_K^*)^2-(\mu_K+X)^2\right] \\ &\quad + T\int\frac{d^3p}{(2\pi)^3}ln\left(1-e^{-(\omega^-(p)-\mu_K)/T}\right)\end{aligned} \tag{4.18}$$

where $\omega^-(p) = \sqrt{p^2+(m_K^*)^2} - X$ is the in-medium energy of a K^- with momentum p. Again, the kaon contribution to the other thermodynamic quantities can be found by differentiation. For a detailed derivation and presentation of the thermodynamics of this model, see Ref. [76]. For discussions of similar studies involving mixed-phases in mean-field-theories in several different physical contexts see, e.g., [77, 78, 108, 80].

Our goal here is to study the rate at which K-matter nucleates in a background of npe-matter at various temperatures and densities. As discussed previously, this involves calculating the free energy of droplets of various sizes, in particular, the free energy of the critical droplet configuration. The first step toward this end is to produce a description of a droplet of K-matter of arbitrary radius. This involves solving the meson field equations of motion subject to various constraints.

Generally, one solves simultaneously two versions of the meson field equations above: one with $\theta = 0$ describing the N-matter component of the mixed phase, the other with $\theta \neq 0$ (with the specific value of θ determined self-consistently through Eq. (4.9)) describing the K-matter. One requires chemical equilibrium between the two phases, i.e., that the relevant chemical potentials in the two phases match. Additionally, the requirement of overall electric charge neutrality means that the electric charge densities in the two phases must be of opposite sign. One then uses the respective charge densities to calculate $f = -q^{(N)}/(q^{(K)}-q^{(N)})$, the volume fraction of the K-matter phase. (Here $q^{(N)}$ and $q^{(K)}$ are the charge densities of the K-matter and N-matter, respectively.) Because we are concerned with droplets of small radius, it is also crucial to include correct mechanical equilibrium between the two phases. In Ref. [81] this requirement was shown to affect rather dramatically the bulk properties of the two phases. (See also [82].) For a spherical droplet of K-matter in a background of N-matter, this constraint reads:

$$P_K - P_N = 2\sigma/R \tag{4.19}$$

where σ is the surface tension between the two phases, and R is the radius of the droplet.

Finally, it should be noted that we work at constant baryon number density. That is, in constructing a sequence of droplets of varying radii, we require that the overall baryon density $n_B = f n_B^{(K)} + (1-f) n_B^{(N)}$ be held fixed at some specified value. Here $n_B^{(N,K)}$ are the baryon number densities of the N- and K-phases.

Once the equations of motion are solved self-consistently subject to these constraints, it is possible to calculate the free energy of a given droplet. The total bulk energy density of a given droplet configuration is defined analogously to the overall baryon number density:

$$\epsilon_{bulk} = f\epsilon^{(K)} + (1-f)\epsilon^{(N)} \tag{4.20}$$

where the energy density in each phase includes the contributions from the nucleons, leptons, and kaons, as appropriate. The total bulk energy is then found by multiplying this energy density by the total volume of a Wigner-Seitz cell (defined as the spherical region including one droplet and containing zero total electric charge), V_{WS}. This energy is then supplemented by the surface and Coulomb contributions:

$$E(R) = \epsilon_{bulk} V_{WS}(R) + 4\pi R^2 \sigma + E_{Coul} \tag{4.21}$$

where E_{Coul} is found by integrating the electric field energy density $\epsilon_{Coul}(r) = \frac{1}{2}|E(r)|^2$ throughout the Wigner-Seitz cell. (Here $|E(r)|$ is the magnitude of the electric field determined by Gauss' law.) The total entropy of a droplet configuration is calculated in the same way as the baryon and energy densities: volume-fraction-weighted averaging of the individual phase entropy densities, then multiplying by the volume of the Wigner-Seitz cell. Thus, the total free energy of a droplet can be calculated as:

$$F(R) = E(R) - TS(R). \tag{4.22}$$

Only the R-dependence has been indicated explicitly, but, of course, the energy and entropy both depend strongly on the fixed baryon number density, the temperature, neutrino fraction, *etc.*

We are interested, however, not merely in the free energy of a given configuration, but, rather, the change in free energy required to produce various droplets. Hence, we also solve

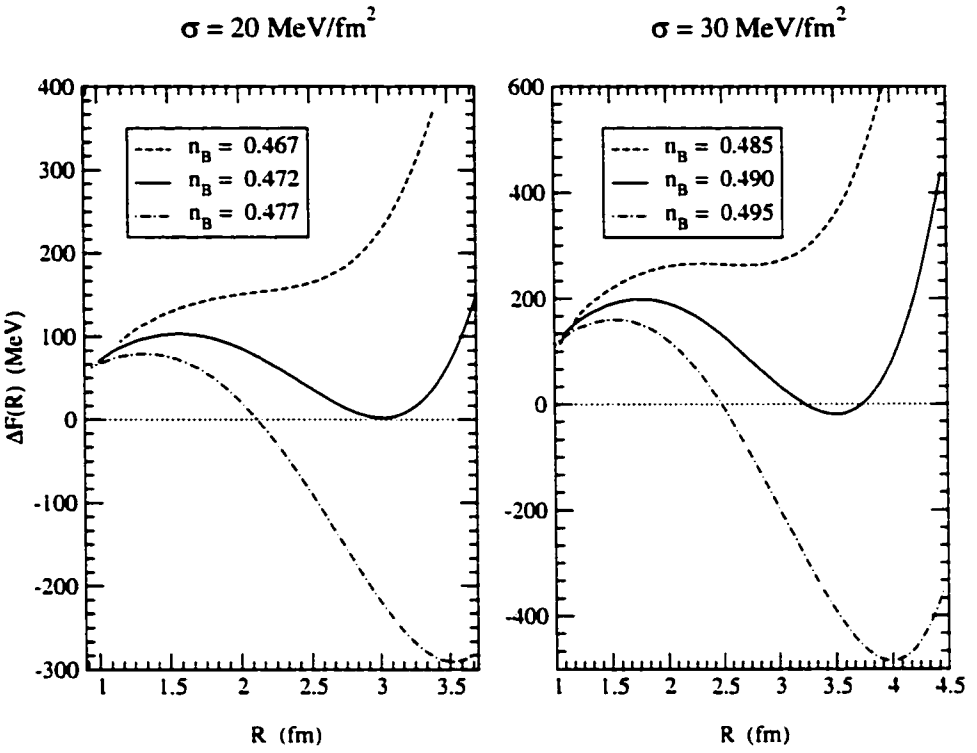

Figure 4.1: Free Energy cost of kaon droplets (as a function of the radius) for two different values of the surface tension, σ. Each plot is shown near the critical density for the transition (which is slightly different for the two values of σ), with additional curves drawn just above and just below the critical density, showing the development of an energetically favored droplet structure as the density is increased past the critical density.

for pure, charge neutral npe matter at a given baryon density and calculate its free energy density, $f_{npe} = \epsilon - Ts$. We are then led to define

$$\Delta F(R) = F(R) - f_{npe} V_{WS}. \tag{4.23}$$

which represents the free energy cost of a transition from electrically neutral npe matter (the initial state of an evolving proto-neutron star) to a single droplet of kaon-condensed matter of radius R. Fig. 4.1 shows $\Delta F(R)$ as a function of R near the critical density for the transition, for two different values of the surface tension, $\sigma = 20 MeV/fm^2$ and $\sigma = 30 MeV/fm^2$.

We have shown the free energy curves for two values of σ in order to illustrate the role

this quantity plays. As expected, smaller values of σ reduce both the size and free energy cost of a critical droplet. In what follows, we will simply pick the value $\sigma = 30 MeV/fm^2$, a value suggested by Glendenning's study of the boundary between the two phases [83], as well as by our own earlier work on this model [81].

In the following section we will use this type of curve to acquire information about the free energy cost of a critical droplet under various conditions of temperature, density, and neutrino fraction.

4.3 Droplet Free Energy and Nucleation Rates

As mentioned in the introduction, one can understand the production of kaons in the neutron star matter as being due to the weak decay of an electron (or, equivalently, the change of a neutron into a proton plus a kaon). By definition, above the critical density this transition is energetically favorable, i.e., exothermic. So we may schematically write

$$e^- \rightleftharpoons \nu_e + K^- + \text{Heat}. \tag{4.24}$$

The excess heat generated by the production of kaons will eventually be radiated away in the form of photons and neutrinos as the neutron star cools, but that is not our interest here. Rather, our goal is to understand how the free energy of droplet configurations depends on the temperature. Qualitatively, one can guess the correct answer by applying LeChatelier's principle to the equilibrium indicated in Eq.(4.24): raising the temperature will tend to push the equilibrium back toward the left. That is, raising the temperature should lower the energetic favorability of kaon droplets.

This prediction is borne out by our calculations, as illustrated in Fig. 4.2. As the temperature is increased from zero, the free energy of kaon droplet configurations increases relative to that of neutral npe matter at the same density and temperature. This increase (which is as large as several hundred MeV for typical droplets) means that, at a density where the mixed phase would be the ground state at $T = 0$, the mixed phase is no longer favored at higher temperature. In other words, turning up the temperature increases (slightly) the critical density for the transition.

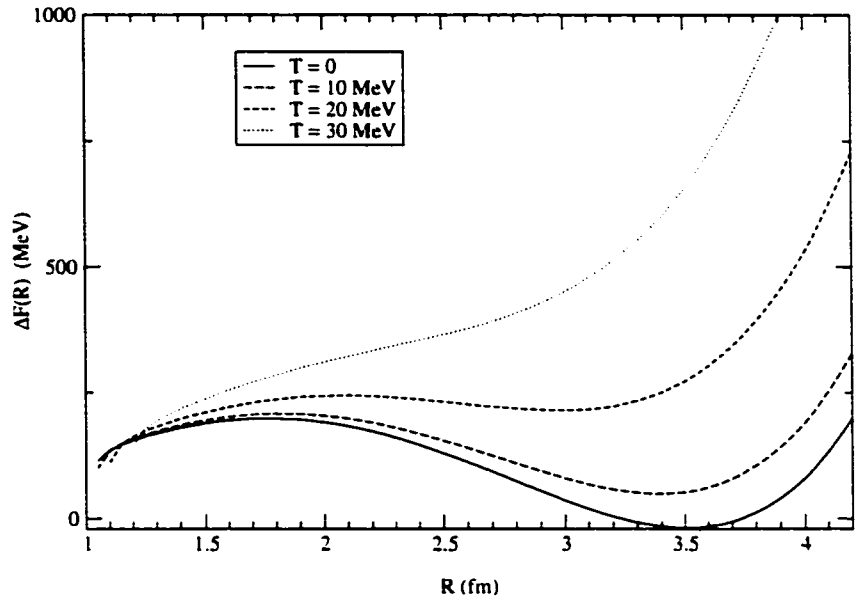

Figure 4.2: Free energy of droplets (relative to neutral npe matter with the same baryon number density) as a function of radius at temperatures varying between zero and 30 MeV. As expected, increasing the temperature decreases the energetic favorability of the kaon phase.

However, because the kaon phase droplets must be produced by thermal fluctuations, we expect the thermal nucleation rate of the kaon phase to be much larger at higher temperatures. In order to estimate the speed with which droplets of the kaon phase are produced, we use the Langer nucleation rate theory discussed in the introduction. The nucleation rate per unit volume is estimated as:

$$\Gamma \sim T^4 e^{-\Delta F(R_{crit})/T} \tag{4.25}$$

where T is the temperature and R_{crit} is the critical droplet radius (at a given temperature and baryon density). The free energy cost of this critical droplet configuration (i.e., the height of the barrier which must be crossed to produce a stable droplet of the new phase) can be easily read off of graphs like the ones already shown. One may then plug directly into Eq. (4.25) to give the nucleation rate per unit volume. In order to convert this rate into an intuitively meaningful quantity, we calculate the expected time for a single nucleation

event in a single typical Wigner-Seitz cell of volume $V_{WS} = 10^3 fm^3$. This time is given by

$$\tau = \frac{1}{\Gamma V_{WS}} = \frac{e^{\Delta F(R_{crit})/T}}{V_{WS} T^4} \tag{4.26}$$

In Fig. 4.3 we show this nucleation time as a function of density for several different temperatures. (Note the log scale!) As expected, the nucleation time is a very strong function of the temperature. At a temperature of 0.1 MeV, the expected nucleation time is many, many times longer than the age of the universe across the entire density range of the mixed phase. At $T = 1.0$ MeV the nucleation time is prohibitively long at the lower end of the mixed phase density regime, but is less than one second at densities above about $n_B \sim 0.55 fm^{-3}$, which is something like $\frac{1}{2} n_o$ above the critical density. At higher temperatures, the nucleation proceeds almost immediately across the entire density range.

Naively, this leads to the conclusion that the neutron star settles into its ground state without any delay as it cools down from an initial temperature of several tens of MeV. In the initial, hot conditions, thermal fluctuations are sufficiently fast and sufficiently numerous to seed K-matter droplets wherever those droplets are energetically favored. The sizes and distances between adjacent kaon structures may undergo tiny changes as the matter cools, and perhaps the outer edge of the mixed phase extends outward somewhat as the critical density decreases, but generally the neutron star includes the full mixed phase from birth.

This picture is complicated by at least two factors which have not been discussed explicitly until now. The first of these is the presence, in the early stages of proto-neutron star cooling, of a significant neutrino fraction. The second question is whether or not we should believe the rate estimates just given, since the nucleation rate prefactor (estimated above as T^4) describes the rate of microscopic fluctuations, which, in the present case, consist of *weak* interaction processes. These processes are, after all, weak, so one might doubt that the naive estimate based simply on dimensional analysis is appropriate. This issue will be discussed in a subsequent section; for now, we will turn to the question of the effects of neutrinos on the nucleation of K-matter. (For a related discussion see Ref.[84])

Returning to Eq. 4.24 and again applying LeChetalier's principle, we guess that the presence of a non-zero density of electron neutrinos will (like high temperature) suppress the appearance of K-matter. This guess turns out to be correct, but for slightly complicated

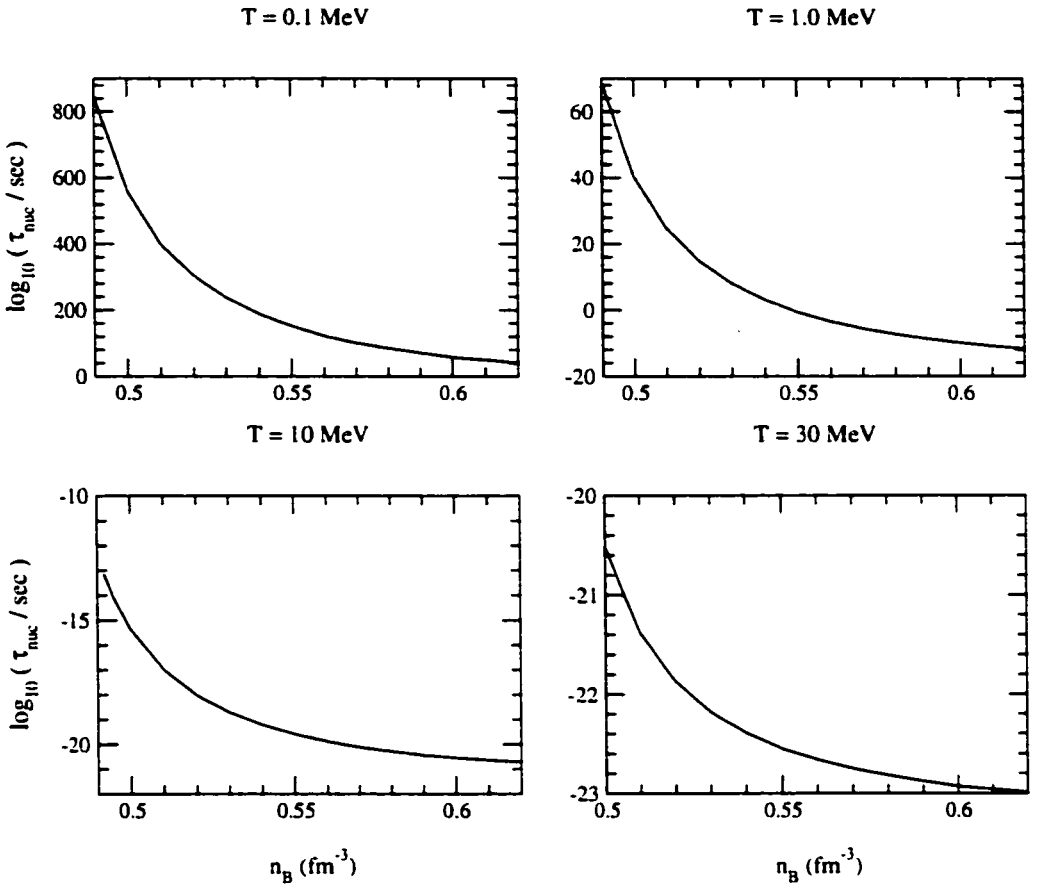

Figure 4.3: Expected time for the nucleation of a single K-matter droplet in a typical Wigner-Seitz volume. Shown is the log_{10} of the nucleation time in seconds as a function of baryon number density, at several different temperatures.

reasons. Turning on a non-zero electron neutrino fraction

$$Y_{\nu_e} = \frac{n_{\nu_e}}{n_B} \tag{4.27}$$

forces the chemical potentials for electrons, kaons, and the baryons to adjust according to the constraint of constant n_B and β-equilibrium, Eq. 4.17. Surprisingly, doing this actually lowers the free energy cost of kaon droplets, as indicated in Fig. 4.4.

The reason for this can be understood as follows. The main effect of turning on a chemical potential for neutrinos, is to increase as well the chemical potential for electrons since the constraint of fixed baryon number density doesn't allow μ_n and μ_p much freedom

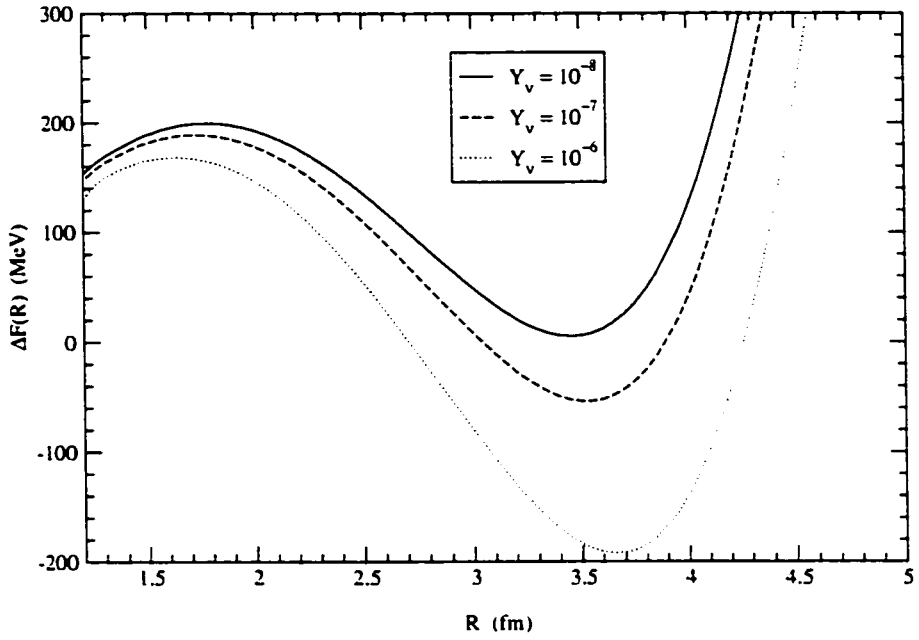

Figure 4.4: Free energy of droplets (relative to neutral npe matter with the same baryon number density) as a function of radius for various small neutrino densities.

to adjust. But increasing the number density of electrons decreases the (positive) electric charge density of the N-matter outside a kaon droplet. Hence, more of this matter is needed to cancel the negative charge of the droplet itself, and the volume fraction of K-matter, f, decreases. But the overall free energy density depends on f through Eq. 4.20. Finally, since the energy density of K-matter is somewhat larger than that for electrically neutral npe matter (due not only to the presence of kaons, but also to the higher local baryon density) while that of the surrounding N-matter is somewhat lower than neutral npe matter (due to the correspondingly lower baryon number density here), the overall energy density of the mixed phase is actually decreased by the decrease in f coming from the non-zero neutrino density.

However, because of the requirement of overall electric charge neutrality and the fact that the K-matter is always negatively charged, the N-matter component outside of the droplet must have a positive electric charge density. As we have just seen, the presence of even a small non-zero chemical potential for electron neutrinos also increases the density

of electrons, and thereby reduces the positive charge in this region. As expected, a larger neutrino fraction will decrease the electric charge density here even more, and eventually a point is reached at which the charge density ceases to be positive. Then it is no longer possible to define a Wigner-Seitz cell, *i.e.*, no longer possible to satisfy the requirement of electric charge neutrality.

Actually, this point is reached for very moderate values of the neutrino fraction, especially at low densities (near the critical density for the transition) where, by definition, the electric charge density in the N-matter phase is positive, but small. We find that the pressure equilibrium condition Eq. 4.19 also has a comparable effect on the electric charge densities via the electron chemical potential. (This issue was discussed in Ref.[81].) In particular, larger structures at a given baryon density have lower electron chemical potentials; hence it is possible to elude the effect of non-zero Y_ν by producing larger K-matter droplets. Thus, at a given Y_ν and a given baryon density, there will be a minimum size R_{min} consistent with charge neutrality, and such structures are therefore not allowed. Electron Debye screening will also play a role in forbidding structures with large radii, so the region of $n_B - Y_\nu$ parameter space in which no mixed phase can exist is even somewhat larger than suggested here.

We show in Fig. 4.5 this minimum radius as a function of baryon density, for several different values of the electron neutrino fraction, Y_ν. At a given Y_ν, the minimum radius allowed by global charge neutrality begins to diverge as one comes down in density. The density at which this quantity diverges (or, if we were to consider also the effects of Debye screening, the density at which this quantity exceeds 5-10 fm) acts as an effective critical density for the onset of the mixed phase. Hence, early in the evolution of the proto-neutron star (PNS), when the neutrino fraction is (at least) a few percent, no mixed phase will be produced at densities less than $0.60 - 0.65 fm^{-3}$. This is to be compared to the critical density at zero temperature and zero neutrino fraction, $0.49 fm^{-3}$. Actually, the electron neutrino fraction in the first seconds of PNS evolution may be closer to ten percent, in which case the effective critical density below which no stable kaon mixed phases exists will be pushed upward to around $0.80 fm^{-3}$, several factors of n_0 above the nominal ($T = 0$, $Y_\nu = 0$) critical density. The upshot is that, in the neutrino-rich conditions of the early PNS

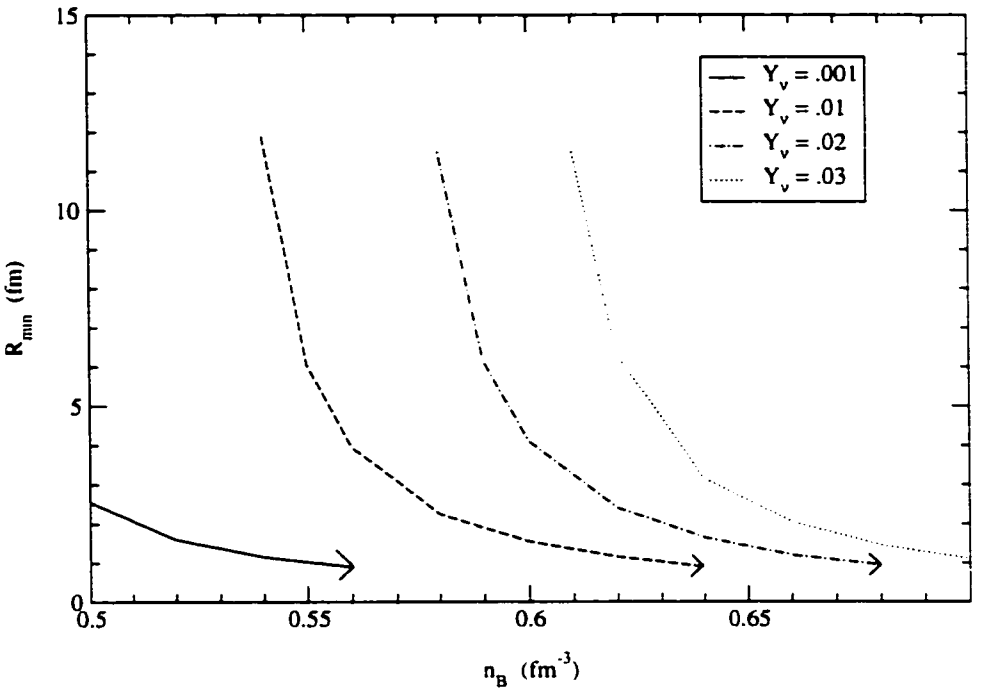

Figure 4.5: Minimum droplet radius consistent with overall electric charge neutrality, as a function of baryon number density, for several different values of the neutrino fraction Y_ν. Here the temperature is fixed at $T = 0$.

evolution, the critical density for the onset of the kaon mixed phase is increased significantly compared to the nominal critical density. To see this more directly, we have shown in Fig. 4.6 the phase diagram in the $n_B - Y_\nu$ plane. The finite-size-energy-correction line represents the requirement that the minimum allowed droplet radius (discussed above) be less than the electron Debye screening length $\lambda_D \sim 5fm$.

This obviously modifies the naive inference from Fig. 4.3 that the mixed phase will be produced quickly during the earliest times of the PNS evolution. Because the neutrino fraction is initially large, there is a wide range of densities over which no mixed phase can be formed at these early times. Hence, due to the suppression of K-matter by neutrinos, a PNS with central density not too far above the nominal critical density for the onset of the mixed phase may fail to produce any K-matter during its cooling, at least until the neutrino fraction Y_ν drops to very nearly zero. The temperature is still expected to be of

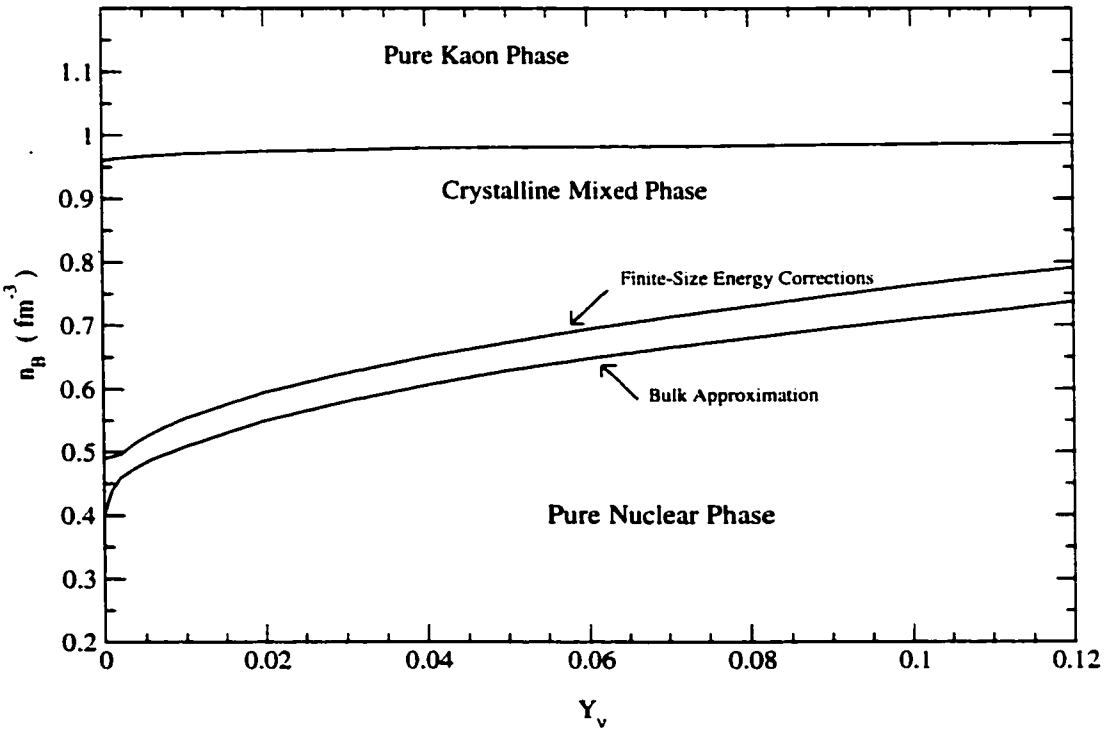

Figure 4.6: Phase diagram for the kaon condensate model discussed in the text showing the relatively steeply sloping boundary for the onset of the kaon mixed phase as the electron neutrino fraction is increased.

order $10MeV$ when this occurs, however, so one again expects the mixed phase to form relatively fast (referring back to Fig. 4.3) once the neutron star core crosses into the mixed phase region of the phase diagram (Fig. 4.6). As we will see, however, even this expectation may need to be modified.

4.4 Fluctuations and the Problem of Simultaneous Weak Interactions

Up to this point we have estimated the nucleation rate prefactor I_0 as simply T^4. This factor, however, is proportional to the growth rate of droplets near the critical size. (See Ref. [85] for a detailed discussion.) For the case at hand the growth of droplets along the unstable direction in configuration space necessarily involves the production of strangeness. Hence, the relevant growth rate must involve a factor $G_F^2 \sin^2\theta_C$ where θ_C is the Cabbibo angle and G_F is the Fermi weak-interaction constant. Forcing this factor into our dimensional analysis estimate yields the new estimate

$$I_0 \sim G_F^2 \sin^2\theta_C T^8. \tag{4.28}$$

Comparing to the results of Fig. 4.3, this new estimate increases the expected nucleation times at a temperature of $T = 10MeV$ by 15-20 orders of magnitude, implying that what was previously guessed to be a nearly instantaneous nucleation process may in fact barely occur during the relevant cooling timescales of approximately $1 - 10sec$. At higher temperatures and at densities higher than about $n = 0.6fm^{-3}$ the new phase still appears likely to nucleate quickly, however. But for $T \lesssim 10MeV$ and for densities not too far above the critical density for the onset of the mixed phase (recall that a standard $1.4M_\odot$ neutron star has a central density near the critical density of $0.5fm^{-3}$) it appears possible that the star might cool before the mixed phase has time to nucleate, leaving the star in a metastable configuration. The reliability of this interesting hypothesis, however, should be checked by searching for other (perhaps faster) mechanisms by which the system might surmount the energy barrier $\Delta F(R_{crit})$.

As a first guess, one might suppose that the nucleation of K-matter droplets could be driven by thermal fluctuations in the local number density of baryons. At a sufficiently high baryon number density, the phase transition to the kaon condensed phase becomes second

order, and the kaon field may grow smoothly without having to overcome an energy barrier. Hence, one might suppose that the first-order transition could occur by this same mechanism operating locally: a thermal fluctuation produces a baryon overdensity in a local region of radius $1-2fm$. The kaon field then spontaneously "fills in" this region, producing a stable droplet of K-matter which could then grow to the stable size. In this picture, the nucleation rate would be governed by the frequency of sufficiently over-dense and sufficiently large baryon number fluctuations, rather than the (slow) spontaneous production of strangeness assumed above.

However, there is an immediate and fatal problem with this basic picture. Sufficient fluctuations in baryon density are no-doubt plentiful. A typical $1-2fm$ region contains of order ten baryons, so assuming simple $\sqrt{N}$ fluctuations, a factor of two overdensity is only three standard deviations away from the mean. But the lifetime of such a fluctuation is limited to strong interaction timescales. Indeed, in nuclear matter at these densities, the speed of sound is a sizable fraction of the speed of light, c. Hence, the lifetime of a baryon number density fluctuation is of order $\tau \sim R/c \sim 10^{-23} sec.$ As is well-known from studies of a second-order kaon condensate phase transition, however, the time-scales needed for the development of an appreciable value of the kaon field are $10-15$ orders of magnitude longer than this. [86] Similar conclusions are found for the appearance of strange quark matter from an initial state of 2-flavor quark matter in neutron stars. [87, 88] That is, not surprisingly, the time-scale for the development of the kaon field is typical of the weak interactions.

The production of K-matter droplets, therefore, cannot be driven by density fluctuations in the background of baryons. The microscopic kaon-production rate is simply too slow to keep up with the strong interaction timescales that govern such fluctuations, so long before any appreciable value for the kaon field in the fluctuation has developed, the fluctuation has disappeared.

We conclude that the nucleation rate must be goverened by thermal fluctuations producing fluctuations in the local kaon number density itself (as we assumed from the beginning). However, the droplet growth rate need not necessarily involve the local production of new kaons, but, rather, may involve the capture of the required particles from the diffuse thermal

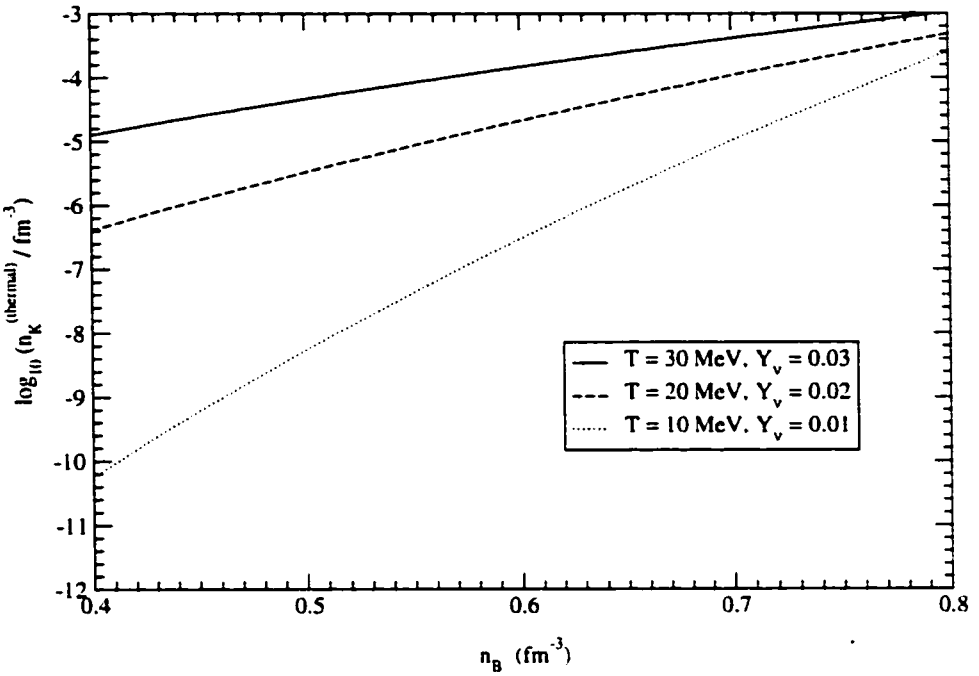

Figure 4.7: Number density of thermal kaons in npe-matter as a function of baryon number density. The three curves correspond (very) approximately to three times during the cooling history of the proto-neutron star. As the star cools, the density of thermal kaons drops substantially and is effectively zero in the context of the probability of seed-production considered below.

background kaon density. This thermal kaon density is given by

$$n_K^{(thermal)} = \int \frac{d^3p}{(2\pi)^3} f_B(\omega^-(p) - \mu_K) \tag{4.29}$$

where f_B is the Bose-Einstein occupation probability and $\omega^-(p)$ was defined in Sect.4.2. We have shown in Fig.4.7 this thermal kaon number density for several values of the temperature and neutrino fraction in npe-type neutron star matter as a function of density.

It is then simple to estimate the probability of a sufficient "seed" of kaons appearing. This calculation is reminiscent of the standard undergraduate statistical mechanics problem of calculating the probability that all of the atoms in a box of gas are found to be in a certain small region of the box. Here, we must calculate the probability that a certain number N of the kaons in a kaon gas of density $n_K^{(thermal)}$ spontaneously appear in some small region

of space with volume V.

For definiteness, consider a large box of volume V_0 and total kaon number N_0, with $N_0/V_0 = n_K^{(thermal)}$. If we treat the kaons as classical particles, then the probability of N kaons being found in a small sub-region V of V_0 is given by the binomial theorem:

$$P(N) = \frac{N_0!}{N!(N_0 - N)!} \left(\frac{V}{V_0}\right)^N \left(1 - \frac{V}{V_0}\right)^{(N_0 - N)} \tag{4.30}$$

Assuming $V \ll V_0$ and $N \ll N_0$, we may approximate $N_0! \sim (N_0 - N)! N_0^N$ and neglect N in the exponent $(N_0 - N)$. This gives

$$P(N) \sim \frac{1}{N!} \left(\frac{N_0 V}{V_0}\right)^N \left(1 - \frac{V}{V_0}\right)^{N_0}. \tag{4.31}$$

But $N_0 V/V_0 =< N >$, where $< N >= V n_K^{(thermal)}$ is the average number of thermal kaons in the volume V. Using $< N > /V = N_0/V_0$ we have finally

$$\begin{aligned} P(N) &\sim \frac{< N >^N}{N!} \left(1 - \frac{< N >}{N_0}\right)^{N_0} \\ &\sim \frac{< N >^N}{N!} e^{-<N>}. \end{aligned} \tag{4.32}$$

(In practice, $n_K^{(thermal)} \ll 1 fm^{-3}$ so the exponential in the last line above can be ignored.)

The number of kaons in a critical droplet varies somewhat with density. Near the critical density (at zero temperature and zero neutrino fraction) the radius of a critical droplet is a few fm, for a critical kaon number of order 100. At higher densities, the critical radius drops to only $1 - 2 fm$, and the corresponding critical kaon number drops to only a few. In Fig. 4.8 we plot the time needed to form such a critical seed (for various N) as a function of thermal kaon number density. To estimate the seed-production time from the probability considered above, we multiply each probability by the maximum possible number of discrete seeding locations within a typical Wigner-Seitz cell. This is of order $V_{WS} n_B \sim 1000 fm^3 \times 0.5/fm^3 \sim 500$. We then assume that the arrangement of thermal kaons is "reshuffled" on the fastest possible time-scale, say $\tau \sim 10^{-23} sec$. (Note that this assumption is extremely generous. The actual reshuffling time must be at least several orders of magnitude greater than this, but here a generous upper limit on the seed-production rate will suffice.) Then the typical time needed for a seed of N kaons to be produced by this

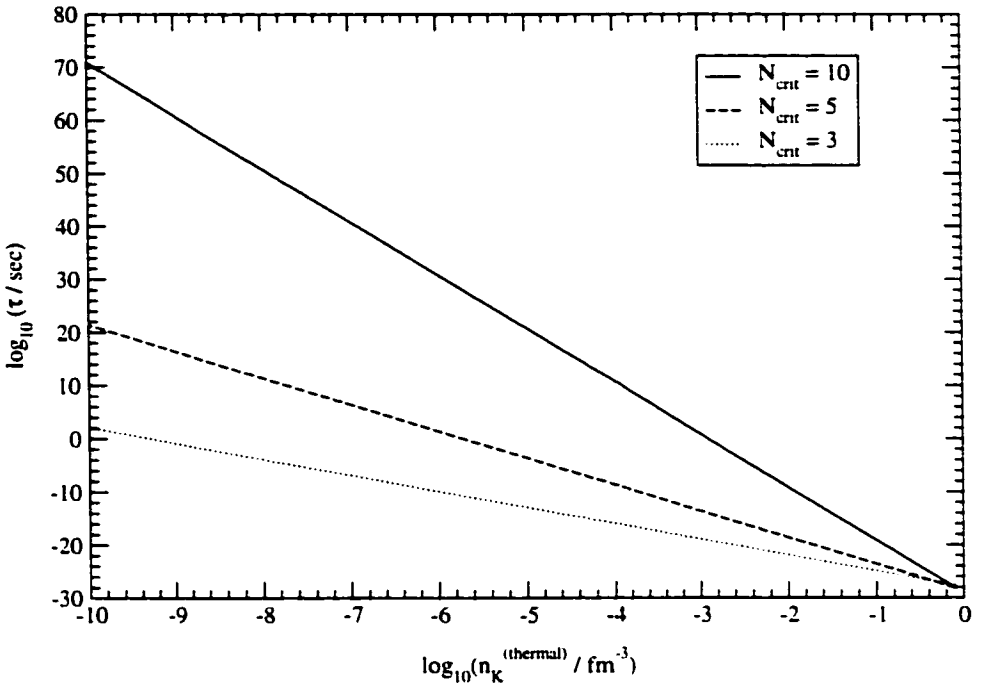

Figure 4.8: Expected time for a critical droplet of N kaons to form out of a spontaneous density fluctuation of kaons with average density $n_K^{(thermal)}$.

method is given by

$$\tau(N) \sim \frac{10^{-23} sec}{500 \cdot P(N)} \tag{4.33}$$

with P(N) given as a function of $n_K^{(thermal)}$ above. Actually, we should replace $P(N)$ here with $\sum_{n \geq N} P(n)$ but in practice each term in the sum is negligible compared to the one previous, so the difference will not affect the result.

We see that the number $N_{critical}$ is indeed critical to the determination of the rate. If ten (or more) kaons are needed to produce a critical droplet, the probability of a sufficient number all showing up in the same place at the same time is extremely small, and one must wait prohibitively long for a seed to ever be produced, especially at lower temperatures where $n_K^{(thermal)}$ is extremely small. At higher densities where N_{crit} is lower, of order 3-5, the probability is much higher the time needed for a seed to be produced by random reshuffling may be of order seconds or less for reasonable values of the temperature.

At the temperatures and densities discussed above (namely $T \lesssim 10MeV$ and $n \lesssim 0.6fm^{-3}$) the time required to accrete a critical number of thermal kaons is many orders of magnitude longer than the corresponding nucleation times estimated previously. This implies that the accretion mechanism for barrier penetration does not contribute significantly to the nucleation speed, and therefore will not help the system avoid ending up in a metastable configuration as the star cools.

It is interesting to note that the crude estimates made here for seed production in a homogenous but fluctuating background of thermal kaons are similar to the estimates in [89, 90, 91] of the growth process for sub-critical Q-balls in a scalar field with a conserved charge. [2] These authors assume a thermal distribution of sub-critical Q-balls with relatively large N, and then consider the rate at which additional charge is accreted to (and released by) the Q-ball via a random-walk process in order to estimate the rate at which critical droplets are produced. In our case, the number of kaons in a critical droplet is not much greater than unity, so we use the Poisson statistics of Eq. (4.32) rather than a Gaussian distribution with $\sqrt{N}$ fluctuations.

Actually, there is an exact analogy between the physics of kaon nucleation and the problem of Q-ball nucleation, *i.e.*, the decay of metastable field configurations in the presence of a conserved charge [92, 93, 94, 95]. The effective potential for the kaon field in our model will be precisely the potential of a complex scalar which supports non-topological solitons, i.e., stable droplets of K-matter. In the limit of infinitely slow weak interactions, this effective theory will contain a global $U(1)$ flavor symmetry corresponding to the conservation of strangeness. In this limit, the seeding of K-matter droplets will occur via a process formally identical to that described in Ref. [95], namely, a small uniform initial charge density (in our case, the background of thermal kaons) producing the required "bounce" configuration by flowing toward a seeding center. As discussed in [95], the $4-D$ Euclidean action associated with this configuration will be significantly greater than the corresponding

[2] Q-balls are non-topological solitons which are supported by theories of charged scalar fields with appropriate self-interactions among the particles. Physically, Q-ball solutions represent spatially-localized droplets of charge which minimize the energy within the sector of fixed charge — that is, the droplet has lower energy per unit charge than the configuration with homogenous charge distribution. See Ref. [92] for a discussion.

case for a real scalar which carries no conserved charge. In the case of quantum tunneling through the energy barrier, then, (which is relevant should the star fail to nucleate the kaon mixed phase during the early, hot epoch) the typical nucleation rates in the case of a charged scalar will thus be exponentially slowed, due to the need for a global redistribution of charge.

Even at low temperatures where quantum tunneling (rather than thermal activation) dominates the nucleation rates, however, the weak interactions are not infinitely slow. In the effective theory of the kaon field described above, inclusion of strangeness-changing weak reactions will correspond to the addition of a small symmetry-breaking term in the effective potential. e.g.,

$$U_{eff}(|K|) \rightarrow U_{eff}(|K|) + \lambda K \tag{4.34}$$

where λ is a strongly temperature-dependent constant that characterizes the rate at which kaons can be produced/absorbed by background scattering processes involving nucleons and leptons.

The actual rate of K-matter nucleation by quantum tunneling will depend on both types of symmetry breaking, that is (1) the initial background thermal kaon density and (2) the dynamical production of new kaons, though it is not obvious which mechanism will dominate the nucleation. In order to treat this problem reliably, one must construct realistic bounce configurations in the kaon effective theory as the initial background density and dynamical breaking parameter λ are varied with temperature, impose imaginary-time periodicity corresponding to the (inverse) temperature, and calculate the action of the bounce. One certainly expects, however, that the nucleation rates will decrease monotonically with temperature, this being the case in particular at the cross-over temperature from thermal-activation-dominated nucleation to quantum-tunneling-dominated nucleation. Therefore, one expects that should the star fail to find its way into the kaonic mixed phase ground state while the core temperature is relatively hot, it will never do so and will remain indefinitely in a metastable configuration.

4.5 Discussion

We have, then, an intriguing possible scenario in which the PNS manages to settle into its ground state without forming the kaon-condensate mixed phase which is the true ground state of the system. At high initial temperatures, the nucleation of K-matter droplets is suppressed by the presence of neutrinos, even though at these high temperatures the seeding of droplets is in principle fast. Over a wide range of densities kaon droplets are produced copiously by thermal fluctuations, but, if produced, they simply decay as the mixed phase is not energetically favored until the neutrino fraction nearly vanishes. As the star cools, the restriction coming from the presence of neutrinos is relaxed, but the intrinsic fluctuation rate drops.

For an initial PNS core density that is not too far above the nominal ($T = 0$) critical density for the formation of a K-matter mixed phase, therefore, it is likely that the star will cool not into the true ground state, but, rather, into a meta-stable state consisting of electrically neutral npe matter. This scenario may be relevant to understanding various phenomenological issues.

For example, the apparent existence of anomalously heavy neutron stars with masses $M \sim 2M_{\odot}$ [15, 18, 19, 20] might be explained by the anomalously stiff equation of state of npe-type matter relative to matter with a kaon condensate. Generally, if the various possible phase transitions thought to occur in neutron star matter can be avoided by the impossibility (or, equivalently, extreme slowness) of nucleation of the new phase, a relatively stiff equation of state may sometimes be maintained over a more extended range of density than would be expected naively. Hence, the existence of such heavy stars may not be sufficient evidence to rule out the existence of kaon-condensation at $3 - 5n_0$, especially if these stars were born with smaller masses and only subsequently (that is, once cold) acquired larger masses via accretion from companion stars.

Additionally, metastability of the sort introduced above may potentially be useful in understanding the properties of GRB's or other poorly-understood explosive events. A relatively light PNS, as we have argued, may cool and deleptonize without the K-matter mixed phase forming, even when the star's core density exceeds the critical density for

the transition. As is evident from Fig. 4.7, however, the thermal kaon density increases monotonically and steeply with density, so that, even at the very low temperatures $T \ll 1$ MeV eventually attained in the neutron star, there is some density at which seeding may become possible in a reasonable time. At very least, with increasing density, one eventually encounters the second-order point at which the kaon field may be produced smoothly with no need for seeding. Hence, if an initially metastable neutron star begins to accrete matter from a companion binary (or, additionally, if an initially rotating metastable neutron star gets spun down via accretion) the central density may increase sufficiently for K-matter to begin to appear.

Once the kaon matter appears, however, there will be a feedback effect, due to the softening of the equation of state. The production of a small quantity of K-matter in the core would allow the star to contract slightly, thus increasing the density in the core, and increasing the size of the region in which kaonic matter can appear. Further kaon production leads to further collapse, and vice versa. Thus if mass accretion and/or spin down results in the critical density for the onset of a second-order kaon-condensate transition being reached in the neutron star core (or, equivalently, if one reaches the low-temperature effective critical density at which a mixed phase can be nucleated spontaneously with sufficient speed) one would expect an explosive event in which the star contracts significantly, resulting in the release of a tremendous amount of energy (of order tenths of M_{sun}). Cheng and Dai have discussed a similar proposal in which accretion-induced conversion to strange quark matter is suggested as a possible explanation for Gamma-Ray Bursters [96].

One especially interesting aspect of such a collapse is its potentially turbulent nature. The picture is of a pure K-matter core seeding the mixed phase through several kilometers of material above it. In effect, the K-matter boils off of the outer edge of the second-order core and floats upward to form the mixed phase throughout the entire region of the mixed phase's energetic favorability. This implies an upward and downward transfer of matter that closely resembles turbulent convection, but in which strangeness rather than heat is the substance being convected.

As mentioned at the end of the previous section, more reliable calculations need to be performed in order to better understand how the slowness of the weak interactions affect

the original nucleation rate estimates based on Equation 4.2, and also to study the interesting (though likely not physically relevant) case of kaon droplet nucleation by quantum tunneling. We have argued that the correct framework for these future calculations involves the formalism of quantum tunneling (or thermal activation) in a theory with a (nearly) conserved global charge representing strangeness. It is also worth mentioning that the scenario outlined here is the most realistic potential application of the Q-ball nucleation formalism developed in [94, 95]; theorists up to now have relied on supersymmetric models to find possible theories containing charged scalars supporting non-topological solitons.

Chapter 5

MIXED KAON CONDENSATION IN CFL MATTER

Up to this point, we have been concerned mainly with the condensation of negative kaons in dense hadronic matter. Qualitatively, this phase transition is favored due to the paucity of strange quarks in the system — at high densities, the chemical potentials for up and down quarks (within hadronic matter) exceed the strange quark mass and the system can lower its energy by allowing weak interactions to spread the quarks over three (rather than two) quark Fermi seas. In the language of hadronic degrees of freedom, this strangeness content will manifest itself through the appearance of hyperons, negative kaons, and/or deconfined 3-flavor quark matter.

At asymptotically high densities, however, we know that the hadronic degrees of freedom are inappropriate: quarks are weakly coupled due to the asymptotic freedom of QCD and we should describe matter in terms of the fundamental quark & gluon degrees of freedom of the QCD Lagrangian. As we will discuss below, at these asymptotically high densities, it has been argued that the ground state of matter consists of a unique color-super-conducting phase in which quarks of different flavors and colors undergo BCS pairing. The ground state energy is minimized for a particular configuration in which the color and flavor degrees of freedom of the BCS pairs are locked to one another — this configuration is thus called the Color-Flavor Locked (CFL) phase.

At more realistic densities, however, the strange quark mass lifts the strangeness chemical potential above the chemical potentials for the two other flavors of quarks, assuming for the moment that the number densities of all three flavors are equal (as required in the CFL configuration). This means that unlike the case of negative kaon condensation in hadronic matter, CFL matter at realistic densities suffers from an *excess* of strangeness: the system would like to relax (that is, to lower its energy) by either destroying some of its strange quarks through the weak interactions or, equivalently, producing a condensate of particles

carrying anti-strangeness. As we will see below, the second alternative is favored at realistic densities.

The goal of the present chapter is to apply some of the technology developed previously to this new case. We will thus study the role of finite size effects in determining whether the system favors a uniform, electrically neutral anti-strangeness condensate — or, as we saw before, a non-uniform, charge-separated mixed phase containing the by-now expected "pasta" structure.

5.1 Introduction to CFL Matter

It is now understood that at asymptotically large densities, the ground state of 3-flavor, massless QCD is the Color-Flavor Locked (CFL) configuration [97, 98, 99]. In this phase, quarks of all three flavors near the (shared) Fermi surface undergo BCS-like pairing due to the attractive one gluon exchange potential. The resulting condensate breaks the $U(1)_B$ symmetry associated with conserved baryon number, and also breaks the original $SU(3)_{color} \times SU(3)_L \times SU(3)_R$ symmetry down to the diagonal subgroup, $SU(3)_{C+L+R}$, causing the gauge bosons of the original $SU(3)_{color}$ group to become massive. However, a linear combination of the eighth gluon and the gauge boson of the $U(1)_Q$ symmetry (the photon) remains massless; this unbroken gauge symmetry will be referred to as $U(1)_{\tilde{Q}}$, denoting physically a "rotated" electromagnetism.

It was originally suggested that due to the large value of the gap the number densities of the three quark flavors would remain equal even when perturbations (non-zero quark masses and charge chemical potential) were included, since the energy cost of breaking pairs exceeded the energy gained by allowing the Fermi spheres for different flavors to relax past one another [100, 101]. It was soon realized, however, that there exists an energetically cheaper mechanism by which the CFL phase could relax under the influence of stresses: meson condensation [102, 103]. For example, turning on a realistic mass for the strange quark encourages the system to reduce the strangeness density relative to the density of up- and down-type quarks. Kaon condensation allows the strangeness density to be decreased without the costly breaking of pairs in the CFL background.

The phase diagram for CFL + meson condensates was explored in detail in Ref. [104]. It was found there that the symmetric CFL phase was favored only when the chemical potential for electric charge satisfied $|\mu_Q| \lesssim 10MeV$ and the quark chemical potential was many orders of magnitude greater than that expected in neutron star cores. At realistic densities, the ground state at zero lepton chemical potential (μ_ν) involves a condensate of K^0 while at very high μ_ν it is the positively charged kaon K^+ which condenses. This ensures overall electric charge neutrality in the presence of a dense background of electrons.

At intermediate μ_ν it was found that a homogeneous mixed phase consisting of both K^0 and K^+ condensates was most effective in lowering the free energy. This mixture sits at a free energy saddle point in the hadronic sector configuration space, but this saddle point becomes a global minimum when one includes the free energy contribution of leptons and imposes local electric charge neutrality.

One may expect, however, that this homogeneous mixed phase could be unstable toward the formation of a heterogenous mixed phase in which the meson condensate rotates toward the K^0 condensed phase in certain regions of space, and toward the K^+ phase in others. This would violate the original assumption of *local* electric charge neutrality, since the K^+ regions would become positively charged and the K^0 regions would become negatively charged. This is allowed so long as the volume fractions of the two phases are such as to conserve charge globally. The question of stability is then the question of whether the cost associated with surface and Coulomb energies can be made less than the energy gained by allowing the meson fields to slide down from the saddle point to regions of lower potential.

This is the issue addressed in this chapter, which is organized as follows. After a quick review of the chiral Lagrangian formalism used to describe mesonic excitations above the symmetric CFL ground state, we argue that the standard approach to studying possible mixed phases (involving some version of the thin wall approximation) will not be appropriate in this case. We then present the results of a small-fluctuation stability analysis of the homogeneous K^0/K^+ mixed phase to derive the dispersion relations for the low-lying excitations and discuss their implications to neutron star cooling and other possible phenomenological issues.

5.2 *Meson Condensation in CFL Matter*

Because of the identity between the symmetry breaking pattern in the vacuum structure of QCD and the symmetry breaking pattern in the CFL phase at high density, it is appropriate to use the same chiral Lagrangian description one uses to parametrize small excitations about the QCD vacuum to parametrize small fluctuations about the $SU(3)$-symmetric CFL phase.

These low energy excitations are parametrized by $\Sigma = e^{2i\pi/f_\pi + \eta'/f_A}$ and $B = e^{\beta/f_B}$ (with $\pi = \pi^a T^a$) where π_a's are the pseudo-scalar octet of Goldstone bosons which arise from the breaking of chiral symmetry and T_a's are Gell-Mann matrices. η' and β are Goldstone bosons due to breaking of the $U(1)_A$ (assumed to be a valid symmetry of the theory at high density due to suppression of instantons [97]) and $U(1)_B$ symmetries, respectively. The decay constants f_A and f_π have been computed in Ref. [102]. Under the original symmetry of $SU(3)_L \times SU(3)_R \times U(1)_B \times U(1)_A$ the Σ field transforms as $(3, \bar{3})_{0,-4}$.

The quark mass matrix $M = \mathrm{diag}(m_u, m_d, m_s)$ induces mass differences between the members of the octet and transforms as $(3, \bar{3})_{0,2}$. Due to $U(1)_A$ charges only even powers of M are present in the effective Lagrangian. To the leading order, only the combination $\tilde{M} = |M|M^{-1} = \mathrm{diag}(m_d m_s, m_u m_s, m_u m_d)$ that transforms as $(\bar{3}, 3)_{0,4}$ contributes to explicit mass terms via the operator $\mathrm{Tr}\Sigma\tilde{M}$. The operator $X = -M^\dagger M/2\mu$ acts as a chemical potential for flavor symmetries [103]. Here μ represents the quark chemical potential. The leading order chiral Lagrangian for the octet is then:

$$\mathcal{L} = f_\pi^2 \left[\frac{1}{4}\mathrm{Tr}\left(D_0\Sigma D_0\Sigma^\dagger - v^2 \mathrm{Tr}\vec{\nabla}\Sigma \cdot \vec{\nabla}\Sigma \right) + \frac{a}{2}\mathrm{Tr}\tilde{M}(\Sigma + \Sigma^\dagger) + \frac{b}{2}\mathrm{Tr}Q\Sigma Q\Sigma^\dagger \right] \tag{5.1}$$

where $v^2 = 1/3$ is the (squared) in-medium meson velocity. The covariant derivative is given by

$$D_0\Sigma = \partial_0\Sigma - i[\tilde{\mu}, \Sigma] \tag{5.2}$$

where $\tilde{\mu} = \mu_Q Q + X$ and μ_Q is the chemical potential for electric charge and $Q = \mathrm{diag}(2/3, -1/3, -1/3)$. The coefficient a has been computed in Ref. [102, 105] and is given by $a = \frac{3\Delta^2}{\pi^2 f_\pi^2}$. The coefficient b, which accounts for charge-dependent differences in the meson masses, has been previously estimated by dimensional analysis to be of order

$b \sim \frac{\alpha\Delta^2}{4\pi}$ where α is the fine structure constant corresponding to the unbroken $U(1)_{\tilde{Q}}$ in the CFL phase [104, 106]. The parameter Δ denotes the value of the gap, which is expected to be of order $\Delta \sim 100MeV$ for $\mu \sim 400 - 500MeV$ [97], though the exact value and scale dependence are not yet well understood [105]. For the following, we will simply take $\Delta = 100MeV$; values of the gap differing from this guess by as much as a factor of two do not change our main qualitative conclusion. It should also be noted that we will generally work in the physically interesting range $\mu \sim 400 - 500MeV$, even though the strong coupling constant at this scale is not much smaller than unity. Our conclusions, then, should be interpreted as only a first approximation to the phase structure of neutron star cores should CFL matter be realized therein. In principle the calculations performed here could be more reliably done for asymptotically larger values of μ; however, this case is not believed to be realized physically in neutron star cores or elsewhere.

The free energy density arising from Eq.5.1 relative to the free energy energy density of the symmetric CFL phase is:

$$\Omega = \frac{f_\pi^2}{4}\left[\mathrm{Tr}[\tilde{\mu},\Sigma][\tilde{\mu},\Sigma^\dagger] + v^2\mathrm{Tr}\vec{\nabla}\Sigma\cdot\vec{\nabla}\Sigma - 2a\mathrm{Tr}\tilde{M}(\Sigma+\Sigma^\dagger-2) - b\mathrm{Tr}[Q,\Sigma][Q,\Sigma^\dagger]\right] \quad (5.3)$$

where Σ is an $SU(3)$ matrix characterizing the direction of the condensate in internal space. As shown in Ref. [104] all stationary points of the free energy for spatially homogeneous configurations will satisfy the matrix equation

$$0 = \left[\tilde{\mu}\Sigma^\dagger\tilde{\mu}\Sigma - a\tilde{M}\Sigma - bQ\Sigma^\dagger Q\Sigma\right] - h.c. \quad (5.4)$$

This equation has two solutions corresponding to minima of Eq. 5.3. The first such minimum corresponds to a K^0 condensate and is parametrized by

$$\Sigma = \exp\left[i\theta_{K^0}\begin{pmatrix}0&0&0\\0&0&1\\0&1&0\end{pmatrix}\right] \quad (5.5)$$

where θ_{K^0} is given by

$$\cos\theta_{K^0} = \frac{M_{K^0}^2}{\tilde{\mu}_{K^0}^2}. \quad (5.6)$$

Where $M_{K^0}^2 = \mathrm{a}(m_d + m_s)m_u$ and $\tilde{\mu}_{K^0}^2 = (m_s^2 - m_d^2)/2\mu$ [104]. (The minimum exists whenever this angle is real.) Similarly, there exists a local minimum of the free energy corresponding to a pure K^+ condensate:

$$\Sigma = \exp\left[i\theta_{K^+} \begin{pmatrix} 0 & 0 & 1 \\ 0 & 0 & 0 \\ 1 & 0 & 0 \end{pmatrix} \right] \tag{5.7}$$

where θ_{K^+} is given by

$$\cos\theta_{K^+} = \frac{M_{K^+}^2 - b}{\tilde{\mu}_{K^+}^2 - b} \tag{5.8}$$

where $M_{K^+}^2 = \mathrm{a}(m_u + m_s)m_d$ and $\tilde{\mu}_{K^+}^2 = \mu_Q + (m_s^2 - m_u^2)/2\mu$ and again the solution only exists when θ_{K^+} is real.

Between the two minima just mentioned, there exists a free energy saddle point configuration involving a mixed condensate of K^0 and K^+. Parameterizing the condensate by

$$\Sigma = \exp\left[i\theta_{SP} \begin{pmatrix} 0 & 0 & \sin\phi \\ 0 & 0 & \cos\phi \\ \sin\phi & \cos\phi & 0 \end{pmatrix} \right] \tag{5.9}$$

one finds a solution to Eq. (5.4) with angles satisfying:

$$\cos\theta_{SP} = \frac{M_{K^0}^2}{\tilde{\mu}_{K^0}^2} + \frac{\tilde{\mu}_{K^+}(\tilde{\mu}_{K^+} - \tilde{\mu}_{K^0})}{b\tilde{\mu}_{K^0}} \left[\left(\frac{M_{K^+}^2 - \tilde{\mu}_{K^+}^2}{\tilde{\mu}_{K^+}} \right) - \left(\frac{M_{K^0}^2 - \tilde{\mu}_{K^0}^2}{\tilde{\mu}_{K^0}} \right) \right] \tag{5.10}$$

and

$$\sin^2\phi = \frac{\left(\frac{M_{K^0}^2}{\tilde{\mu}_{K^0}^2} - \cos\theta_{SP} \right)}{\left(1 - \frac{\tilde{\mu}_{K^+}}{\tilde{\mu}_{K^0}} \right)(1 - \cos\theta_{SP})} \tag{5.11}$$

where as usual the solution is only a stationary point of the free energy if the angles θ_{SP} and ϕ are real.

It was found in Ref. [104] that this saddle point configuration becomes the true minimum of the free energy when one includes leptonic contributions to the free energy and imposes local electric charge neutrality (*i.e.*, homogeneity) on the system. In practice, this means that for a given quark chemical potential μ and lepton chemical potential μ_ν, the chemical

potential for electric charge is determined by the constraint that the electron number density equal the number density of K^+ in the meson condensate:

$$\frac{(\mu_\nu - \mu_Q)^3}{3\pi^2} = -\frac{\partial \Omega_{meson}}{\partial \mu_Q} \tag{5.12}$$

where Ω_{meson} is given by Eq. (5.3).

5.3 *Heterogenous Meson Condensation*

As we have seen several times in previous chapters, the imposition of local electric charge neutrality is often unwarranted, and may hide a lower-energy configuration in which overall charge neutrality results from the cancellation of charge among regions of non-zero local charge density [107]. If this occurs, the resulting crystalline mixed phase may dramatically affect both the equation of state and various transport properties of the neutron star [108].

It is natural to wonder whether the assumption of local charge neutrality mentioned in the previous section was overly restrictive. We begin our analysis of this question by assuming that an inhomogeneous mixed phase of K^0 and K^+ condensed regions is indeed favored, and studying the nature of the boundary layer between two adjacent regions. For now we ignore electrostatic energy contributions and Coulomb screening effects. Following the approach of Ref. [83] we consider a planar boundary and fix the condensates to point in the K^0 and K^+ directions at $\pm\infty$ respectively. We then implement a relaxation procedure which allows the fields to interpolate between the two fixed boundaries in a way that minimizes the total free energy of the surface. Pressure equilibrium across the boundary imposes a constraint which fixes the value of μ_Q. The resulting boundary profile, parametrized by the angles θ and ϕ of Eq. 5.9, for a quark chemical potential $\mu = 400MeV$ is shown in Fig. 5.1.

The notable feature is the large thickness of the energetically favored boundary. One can understand it by comparing the two terms contributing to the excess free energy of the boundary: the gradient terms associated with spatial changes in the field configurations, and the "bulk" terms which tally the cost of being away from a free energy minimum while one traverses the boundary. Since the height of the free energy barrier between the two minima is very small (of order $10^3 MeV^4$), a very thick boundary is required in order to make the two

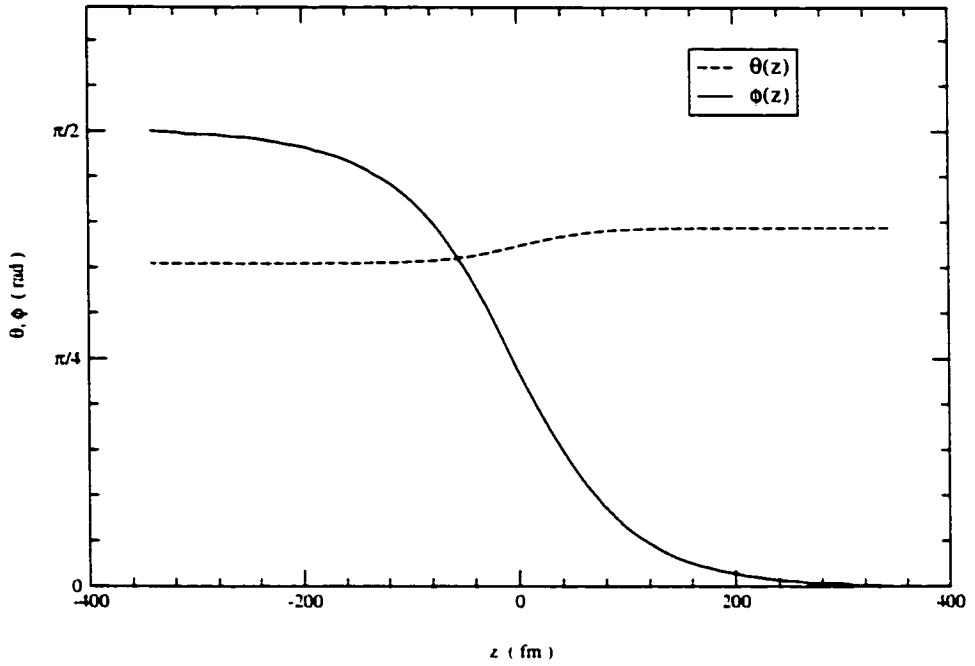

Figure 5.1: Minimal-surface-tension boundary profile between regions of pure K^0 condensed matter and pure K^+ condensed matter at a quark chemical potential $\mu = 400MeV$. The bulk phases on either side of the boundary are at equal pressures. The effects of static Coulomb screening are here ignored. The surface tension found by integrating the excess free energy density across the boundary is $\sigma = 0.082MeV/fm^2$.

contributions comparable, and hence to minimize the overall surface tension. In the example shown, the surface tension turns out to be the quite small value $\sigma = 0.082MeV/fm^2$.

However, a boundary layer between K^0 and K^+ regions with thickness of several hundred fm is not allowed physically, since the Debye screening length of all charged species is much smaller than this length scale. Any structure of this enormous size would be warped out of existence as charge flowed in response to the large electric fields. We can estimate the role of screening by considering the energetics of a single charged droplet of the charged, lower-energy-density phase immersed in a background of the original phase. Ignoring for the moment the Coulomb contribution to the energy, we find

$$E(R) \sim \frac{4}{3}\pi\Delta\epsilon R^3 + 4\pi\sigma R^2 \tag{5.13}$$

where $\Delta\epsilon \leq 0$ is the bulk (free) energy density difference of the two phases. Any droplet larger than $R_{crit} \sim 3\sigma/|\Delta\epsilon|$ will be energetically favored compared to the homogeneous phase, and the volume and surface terms in the energy are of comparable size for droplets of radius near R_{crit}. In order for the droplet to be stable against charged particle flow (Debye screening), the Coulomb contribution to $E(R)$ must be a small correction to the terms already written. Estimating the Coulomb term by $E_C(R) \sim \alpha\rho_Q^2 R^5$ (where ρ_Q is the electric charge density of the droplet) then gives

$$\alpha \ll \frac{|\Delta\epsilon|^3}{\sigma^2\rho_Q^2} \tag{5.14}$$

as the condition for the existence of a charge-separated mixed phase. In the present case, the right hand side is of order 10^{-8} and a stable heterogenous mixed phase (in which each phase sits at one of the local minima of the free energy density) is clearly ruled out for the physical value $\alpha \sim 1/137$.

If a heterogenous mixed phase is formed, then, it will have to involve only smaller departures from the homogeneous saddle point configuration. The condensate may "slide down" toward the K^0 configuration in one region of space, and similarly "slide down" toward the K^+ configuration in an adjacent region, but it cannot slide all the way down to the free energy local minimum. And without any definite guess as to the bulk field configurations in each region, it is difficult to study the energetic favorability of possible mixed phases in the standard way – that is, by taking an ansatz for the mixed phase configuration, treating the boundary as "thin", varying with respect to appropriate parameters (droplet size, *etc.*), and comparing the total free energy to the free energy of the homogeneous phase.

We therefore take a somewhat different approach and study the stability of small perturbations to the homogeneous saddle point configuration. Any unstable modes will signal the instability of the homogeneous phase toward the production of some (largely unspecified) heterogenous mixed phase.

We present the full results of our analysis of the excitation spectrum in the next section; here we will simply quote those results which are relevant to the question of the stability of the homogeneous mixed phase. As we show in detail in Sec. 5.4 the kaonic excitations about the homogeneous, charge neutral configuration consist of two massive kaons, one

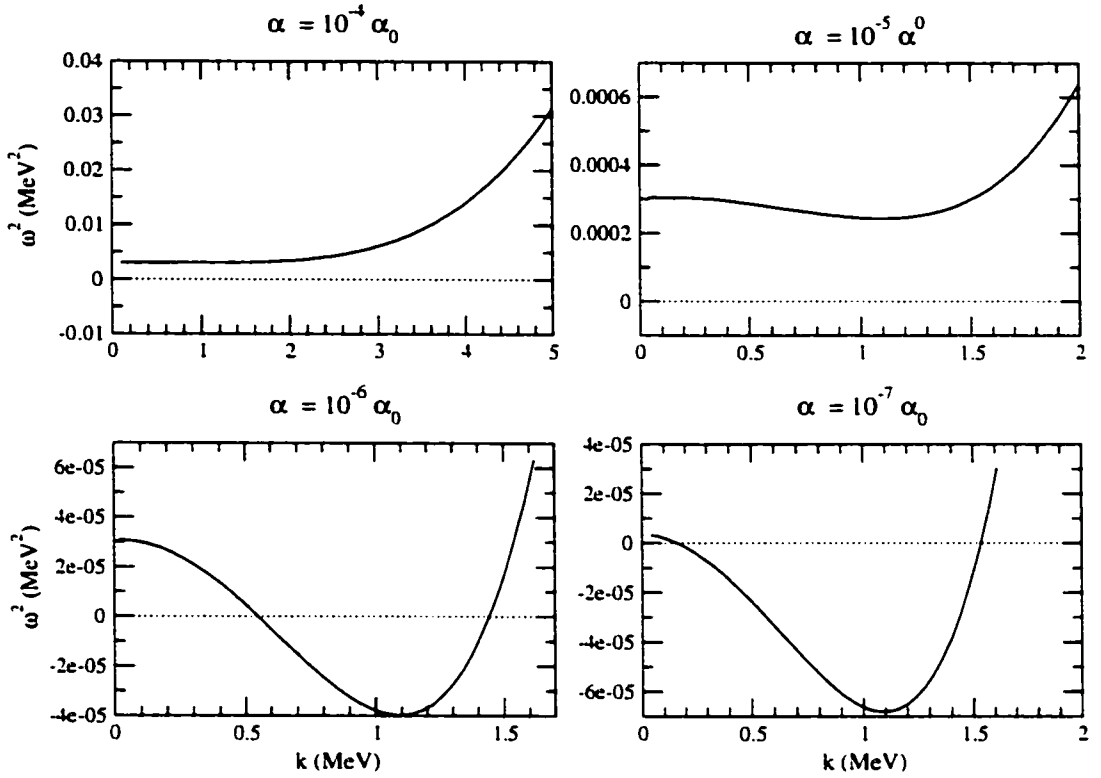

Figure 5.2: Dispersion curves for the longitudinal photon mode for several values of α. (α_0 represents the value 1/137.) The quark chemical potential is set to $\mu = 400MeV$ while $\mu_\nu = 100MeV$. For $\alpha \leq 10^{-6}\alpha_0$ the energy of the mode becomes pure imaginary (for a certain range of wavelengths), corresponding to an instability. Debye screening by electrons is included by giving the longitudinal photon an additional mass squared term equal to $k_D^2 = q^2\mu_e^2/(2\pi^2)$. Note also that the Higgs contribution to the photon mass is proportional to the electric charge q; hence the overall reduction in scale as α is reduced.

massless Goldstone boson arising from the breaking of $U(1)_Y$. and a massive in-medium longitudinal photon (which acquired a mass through the Higgs mechanism by eating one of the kaonic degrees of freedom). Plane-wave oscillations of this longitudinal photon degree of freedom represent longitudinal charge density waves - just the sort of excitations which will be unstable if the homogeneous phase can lower its energy by forming a charge-separated mixed phase.

In Fig. 5.2 we show the dispersion relation for this mode as the electric charge α is varied.

The longitudinal charge density wave is clearly a stable, massive mode until α is reduced many orders of magnitude below the physical value. Note that the critical value of α is not too far from the naive estimate made above based on consideration of macroscopic droplet properties. Also, the static plasma wave is most unstable for wave vectors $|\mathbf{k}| \sim 1MeV$ which corresponds to charged structures with a size of $D \sim 1/|\mathbf{k}| \sim 200fm$. This is again comparable to the size expected from the minimal-surface-tension boundary constructed above and shown in Fig. 5.1 - and is safely smaller than the charged particle Debye screening lengths for such tiny α. We conclude that in real high density matter where $\alpha \sim 1/137$ the homogeneous K^+/K^0 mixed phase is indeed stable against the production of a heterogenous, charge-separated configuration. The energetic cost of Coulomb and surface/gradient energy wins out over the energy savings associated with lowering the bulk energy densities.

5.4 Excitation Spectrum

Having established that the homogeneous K^+/K^0 mixed phase is indeed the true ground state of matter at high density and nonzero neutrino chemical potential, we are now interested in finding the normal modes and dispersion relations for excitations above the ground state. The homogeneous background condensate is given by

$$\Sigma_0 = \exp\left[i\theta_{SP} \begin{pmatrix} 0 & 0 & \sin\phi \\ 0 & 0 & \cos\phi \\ \sin\phi & \cos\phi & 0 \end{pmatrix} \right] \tag{5.15}$$

where the angles are given by Equations (5.10) and (5.11). In order to parameterize small fluctuations about this state, we write the condensate as

$$\Sigma = \xi_0 \hat{\Sigma} \xi_0 \tag{5.16}$$

where $\xi_0 = \Sigma_0^{1/2}$ and

$$\hat{\Sigma} = \exp(2i\hat{\pi}/f_\pi). \tag{5.17}$$

Here $\hat{\pi} = \hat{\pi}_a T_a$ characterizes small rotations away from the homogeneous saddle point configuration given by Σ_0. [1]

[1] This helpful parameterization was suggested by David Kaplan.

In order to account for the Coulomb energy associated with possible charge separation, we must include the coupling of our meson fields to the gauge field associated with the unbroken $U(1)_{\tilde{Q}}$. This is accomplished by promoting the electric charge chemical potential to the role of a space- and time-dependent field. (For the following analysis, we will work in the Coulomb gauge $\vec{\nabla}\cdot\mathbf{A}=0$ in which, to quadratic order in the Lagrangian, the transverse photon modes decouple from the hadronic excitations. Hence for our purposes we only need to keep track of the electrostatic potential. The transverse photon modes will acquire a mass via the Higgs mechanism in the standard way.) In particular, since we are concerned only with small perturbations about the homogeneous phase, we replace

$$\mu_Q \to \mu_Q + \delta A_0(\mathbf{x}, t) \tag{5.18}$$

where μ_Q is the constant value found by requiring the homogeneous phase to be electrically neutral, and δA_0 characterizes local fluctuations in the electrostatic potential. Note that from now on, we ignore the distinction between Q and $\tilde{Q}$ charges. This is expected to be physically accurate for accessible densities, where the mixing angle between the new and old electromagnetism is small [109].

Substituting Equations (5.16) and (5.18) into our Lagrangian, and keeping only terms bilinear in fields we arrive at:

$$\begin{aligned}
\mathcal{L} \;=\; & \mathrm{Tr}\left(\partial_t\hat{\pi}\partial_t\hat{\pi} - v^2(\vec{\nabla}\hat{\pi})^2\right) - i\mathrm{Tr}\partial_t\hat{\pi}\left([\mu_R,\hat{\pi}] + [\mu_L,\hat{\pi}]\right) \\
& + f_\pi q\delta A_0 \mathrm{Tr}\partial_t\hat{\pi}(Q_R - Q_L) - if_\pi q\delta A_0 \mathrm{Tr}\left([Q_R,\mu_L] - [Q_L,\mu_R]\right)\hat{\pi} \\
& - \frac{1}{2}f_\pi^2 q^2\delta A_0^2 \mathrm{Tr}(Q_R Q_L - Q^2) - \mathrm{Tr}[\mu_L,\hat{\pi}][\mu_R,\hat{\pi}] \\
& - a\mathrm{Tr}(M_L + M_R)\hat{\pi}^2 + b\mathrm{Tr}[Q_L,\hat{\pi}][Q_R,\hat{\pi}] \\
& + \frac{1}{2}(\vec{\nabla}\delta A_0)^2 - \frac{1}{2}\delta A_0^2 \Pi^{00}_{elec}(\omega,k)
\end{aligned} \tag{5.19}$$

where we have defined:

$$\begin{aligned}
\mu_R &= \xi_0\tilde{\mu}\xi_0^\dagger \\
\mu_L &= \xi_0^\dagger\tilde{\mu}\xi_0 \qquad (5.20) \\
M_R &= \xi_0^\dagger\tilde{M}\xi_0^\dagger \\
M_L &= \xi_0\tilde{M}\xi_0 \qquad (5.21)
\end{aligned}$$

$$Q_R = \xi_0 Q \xi_0^\dagger$$
$$Q_L = \xi_0^\dagger Q \xi_0. \tag{5.22}$$

(Note that the definitions of M_R and M_L differ from the other two cases.) In the last line of Eq. (5.19) the first term represents the electrostatic field energy, while the second accounts for the coupling of the background electron bath to the electric potential.

The factor $\Pi^{00}_{elec}(\omega, \mathbf{k})$ is the contribution to the temporal photon mass (squared) arising from the background electron gas. The leading-order (gauge-invariant) contribution to this quantity can be written down exactly for the case of a degenerate, relativistic electron gas [110, 111]. It is:

$$\Pi^{00}_{elec}(\omega, \mathbf{k}) = k_D^2 \left(\frac{\omega}{2|\mathbf{k}|} ln \left| \frac{\omega + |\mathbf{k}|}{\omega - |\mathbf{k}|} \right| - 1 \right) \tag{5.23}$$

where $k_D^2 = \frac{q^2 \mu_e^2}{2\pi^2}$ is the (squared) electron Debye screening length. We have omitted a possible imaginary part which describes Landau damping. We expect this damping to become important only for $|\mathbf{k}| \sim \mu_e$. Note that in the static limit $\omega \ll |\mathbf{k}|$ the electron Debye contribution to the photon mass squared becomes simply the constant k_D^2. This was the approximation used in the previous section when studying the stability of the homogeneous configuration. In the present section, we retain the full expression. The effect of the electrons for $|\mathbf{k}| \lesssim k_D$, it turns out, is merely to increase the effective mass of the temporal photon by $1 - 2MeV$ above the mass it gets via the Higgs mechanism.

It is now possible to use symmetries to determine the superselection rules, and make a separate (sparse) ansatz for $\hat{\pi}$ for each non-interacting group of excitations. The simplest such group is the charged pions, π^+ and π^-. We will show the details of this calculation for pedagogical purposes and omit them in the physically more interesting case of kaonic excitations, which we treat next. Writing the pion fields in terms of their real and imaginary parts we have:

$$\hat{\pi} = \frac{1}{\sqrt{2}} (\pi_1 T_1 + \pi_2 T_2) \tag{5.24}$$

where T_a are $SU(3)$ generators with $\mathrm{Tr}(T_a T_b) = (1/2)\delta_{ab}$. Inserting Eq. (5.24) into the Lagrangian Eq. (5.19) and taking appropriate derivatives yields three coupled Euler-Lagrange

equations for the fields $\pi_1^{\pm}$, $\pi_2^{\pm}$, and δA_0. Taking a plane wave ansatz for each field

$$\begin{pmatrix} \pi_1(\mathbf{x},t) \\ \pi_2(\mathbf{x},t) \\ \delta A_0(\mathbf{x},t) \end{pmatrix} \rightarrow \begin{pmatrix} \pi_1 \\ \pi_2 \\ \delta A_0 \end{pmatrix} e^{i(\mathbf{k}\cdot\mathbf{x}-\omega t)} \tag{5.25}$$

then gives a homogeneous linear system in the three field amplitudes. The solutions of this system represent the normal modes and dispersion relations. Since there is no term in the Lagrangian that depends on $\partial\delta A_0/\partial t$, the equation of motion for δA_0 - Poisson's equation - should be interpreted as a constraint. (We are working in Coulomb gauge, where this is standard.) Hence, the system of three linearized equations of motion will have only two normal modes. The dispersion curves for these two modes (which are almost pure π^- and π^+ respectively) are shown in Fig. 5.3.

Because we are expanding about a background condensate consisting of both K^0 and K^+, the neutral kaonic excitations may mix with the charged kaons. In order to find the normal modes and dispersion relations, we proceed as before, writing

$$\hat{\pi} = \frac{1}{\sqrt{2}}\left(K_1^0 T_6 + K_2^0 T_7 + K_1 T_4 + K_2 T_5\right) \tag{5.26}$$

and substituting this ansatz into the quadratic Lagrangian. Requiring harmonic dependence on x and t as before gives a coupled system of five equations of motion for the field amplitudes. The dispersion relations for the four normal modes are shown in Fig. 5.4.

There is one exactly massless mode which can be identified as the Goldstone boson arising from the fact that the K^0/K^+ condensate breaks the $U(1)_Y$ hypercharge symmetry of the original theory. (Weak interactions, however, will give a small mass to this particle [112].) This Goldstone boson corresponds to K_2^0 in our above ansatz, *i.e.*, it consists of harmonic fluctuations in the imaginary part of the neutral kaon fields (as expected). There are also two massive modes (with masses of about $32MeV$ and $48MeV$). The lighter of these is predominantly a K^0 with a small admixture of K_1^0 and K_1, while the heavier is mostly a K^- with a small admixture of K^0. Finally, the temporal photon mode (consisting, as expected, of the imaginary part of the charged kaon field plus a sizable electric field) weighs in with a mass of about $8MeV$. As discussed previously, this mode (which came from

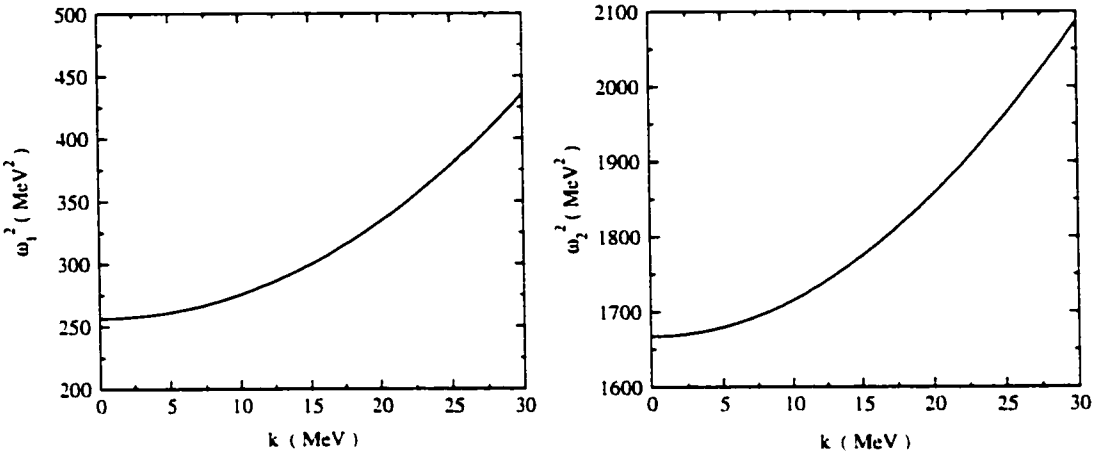

Figure 5.3: Dispersion curves for the two charged pion normal modes at $\mu = 400MeV$ and $\mu_\nu = 100MeV$. The first normal mode corresponds to an almost pure π^- state with a numerically tiny admixture of π^+: *vice versa* for the second mode. The in-medium masses of the two charged pions are approximately $15MeV$ (for the π^--like state) and $40MeV$ (for the π^+-like state). The large mass splitting between the differently charged states arises from the nonzero value of the charge chemical potential, μ_Q.

the photon eating the would-be-Goldstone-boson from the breaking of $U(1)_{\tilde{Q}}$) corresponds physically to a plane-wave plasma oscillation of the (rotated) electric charge density. Note again that the background condensate breaks the usual superselection rules and allows the excitations to be coherent mixtures of states with different hypercharges and (rotated) electric charges.

5.5 Discussion

We have shown that the homogeneous K^0/K^+ condensate in CFL matter at non-zero μ_ν is stable against the production of a heterogenous, charge-separated mixed phase. Due to the very short potential energy barrier between the pure K^0 and K^+ phases, the cost of surface and Coulomb energies is too large for charge separation to be energetically favorable.

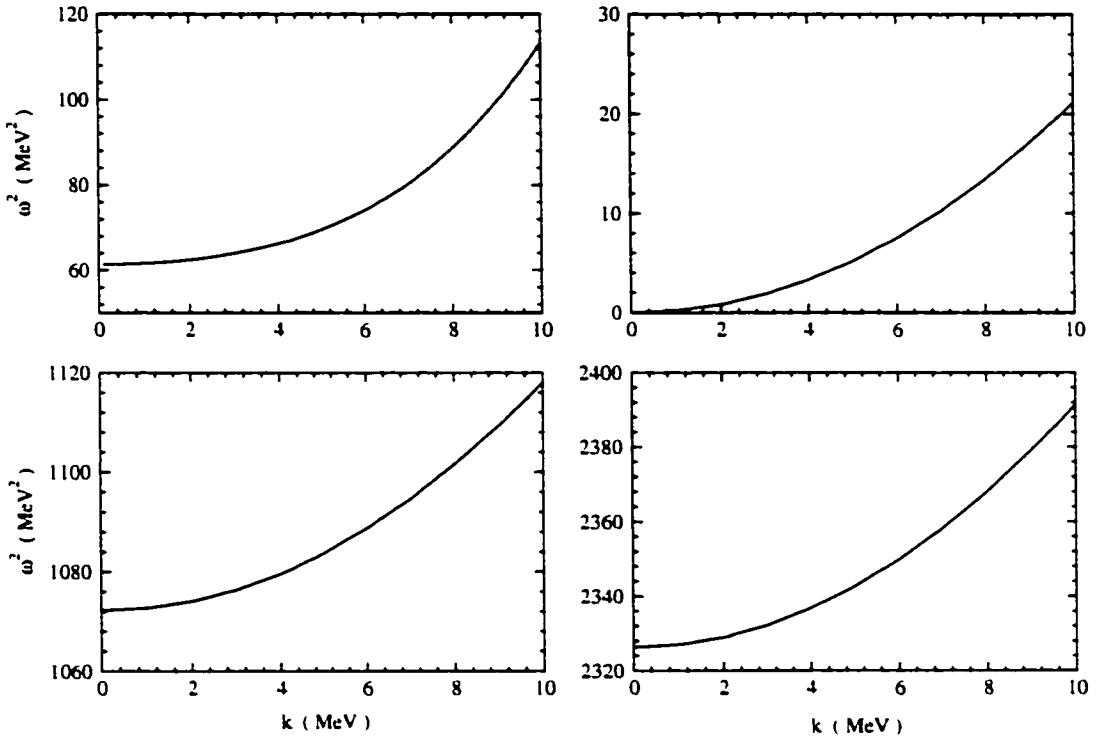

Figure 5.4: Dispersion curves for the four kaonic normal modes at $\mu = 400MeV$ and $\mu_\nu = 100MeV$. The upper-left figure shows the longitudinal photon mode, which we have also described as a longitudinal plasma oscillation. With the physical value of the fine structure constant, this mode is stable ($\omega^2 > 0$) and the homogeneous K^0/K^+ mixed phase is the true ground state of the system. There are also two massive kaon modes, and a single massless mode arising from the breaking of the $U(1)_Y$ hypercharge symmetry by the K^0 portion of the condensate.

Although we have focussed our discussion on a single point in the μ-μ_ν phase diagram, the stability of the homogeneous phase persists throughout the *CFL* K^0/K^+ region identified as the ground state in Ref. [104]. (As pointed out in Ref. [113], the Coleman-Weinberg mechanism [114] may produce a small additional incentive favoring the production of charge-separated domains. However, this incentive appears to be either absent or negligible for realistic densities relevant to neutron star cores.)

The normal modes and excitation spectra we discussed in the previous section may be relevant for future calculations of the neutrino scattering rates in the cooling neutron star.

Of special importance in this context is the relatively light ($m_\gamma \lesssim 10MeV$) photon mode. Since this excitation involves a spatially fluctuating density of electrons and charged and neutral kaons, one may expect large cross sections for neutrino scattering. The physics here is similar to that discussed in Ref. [115] where it is shown that coherent neutrino scattering from droplets of kaonic matter (whose weak charge density differs significantly from the hadronic background) will dramatically affect neutrino scattering rates and hence potentially observable neutrino light curves from supernovae. Equivalently in our problem, one expects that due to the spatial oscillation of the electron and kaon densities, the cross section for neutrino - photon scattering will be large and that the copious presence of such excitations for $T \gtrsim m_\gamma \sim 8MeV$ may significantly increase the time required for neutrinos to diffuse out of the proto-neutron star. One might hypothesize that only the relatively early-time neutrino light curve would be thereby stretched out in time since, if the dominant contribution to neutrino scattering rates indeed comes from these longitudinal photon excitations, there will be a relatively sudden change in the density of "targets" as the core temperature drops below m_γ.

Also, as discussed in Ref. [116], the breaking of various $U(1)$ symmetries (hypercharge and rotated electromagnetism) by the mixed kaon condensate will allow for the presence of global and/or gauged vortices and vortons. The present work, in determining the in-medium masses for the various kaonic excitations, thereby also fixes certain properties of kaonic vortices, *e.g.*, the distance scale over which a superconducting K^+ condensate at the center of a K^0 vortex will fall off with distance. The in-medium masses of the various components of the (rotated) photon will also be relevant for a detailed description of the spatial dependence of the electric and magnetic fields surrounding such vortices. These vortices may also affect the cooling history of young neutron star through their neutrino opacities and magnetic properties.

A more detailed treatment of the various particle-like and topological excitations above the homogeneous K^0/K^+ condensate, and especially their effects on neutrino scattering and diffusion, will be left for future work.

Chapter 6

CONCLUSIONS

In this thesis I have

- Reviewed the present state of the physics community's understanding of neutron stars including their formation in core-collapse supernovae, their properties (including masses, radii, spin-down and cooling rates), and the nature and structure of matter at different densities and thus different depths within the star.

- Discussed the possible existence of and conditions allowing for a heterogeneous, charge-separated mixed phase occupying a finite radial extent within the neutron star.

- Applied and explored the implications of these conditions on one proposed high-density phase transition (negative kaon condensation), including calculations of the crucial role played by so-called "finite size effects" including pressure differences between the two co-existing phases (due to the nonzero value of the surface tension) and Debye screening of charged particle profiles. Even if negative kaon condensation is found not to occur in real neutron star matter, this exercise remains potentially enlightening for alternative phase transitions (such as that resulting in deconfined quark matter) which may occur instead — one learns a tremendous amount about the coexistence of phases in the kaon condensation model treated here by virtue of the fact that both phases (and, crucially, the boundaries between them) can be treated within the purview of a single theoretical framework (which is not the case for, e.g., bag models of quark matter).

- Estimated the dynamical production (nucleation) rate for the appearance of a kaon-condensate mixed phase at various times in the early evolution of a neutron star. This

resulted in some preliminary evidence supporting the hypothesis that a newly-born neutron star (whose mass is not too far above the typical value of $1.4M_{\odot}$ may cool into a configuration which is not the true ground state of the system. The false ground state would be metastable: it was shown that should a neutron star fail to nucleate the favorable kaonic matter during the first few tens of seconds of its evolution, subsequent nucleation would be absolutely prohibited due to the extremely long seeding times at very low temperatures. An infinitely long time spent in the metastable configuration might be avoided, however, should an initially rotating metastable neutron star be spun down to a state in which (or should the neutron star accrete matter until) its central density exceeds the point at which the kaon condensate transition becomes second order. Then a turbulent delayed collapse may occur, potentially releasing a few tenths of a solar mass of energy in a dynamical (that is, short) timescale.

- Analyzed the phase structure of kaon condensates in Color-Flavor Locked quark matter at high densities and at nonzero values of the neutrino chemical potential, finding, in particular, that finite-size effects involving Coulomb and surface energies (and Debye screening) are so large as to prevent the formation of a heterogeneous mixed phase that would otherwise (that is, in the absense of finite-size effects) be the favored ground state of the system.

The above physics is relevant both to future work on the structure of matter at high density and to continuing attempts to understand the phenomenological implications of ever-improving neutron star and supernova observations. For example:

- As neutron star observations achieve increasingly accurate measurements of masses and radii, it becomes increasingly important to understand the role played by the various proposed phase transitions to "exotic" matter. As was shown in Chapter 3, accurate treatment of Coulomb and surface energies in the mixed phase will increase the critical density for the appearance of the new phase and thereby also increase the neutron star maximum mass by an amount of order $0.1M_{\odot}$. Such corrections are already large compared to the experimental uncertainties on several NS masses, so it

is clear that the kind of work presented here (as well as its extensions to alternative proposed phases) will become increasingly important in interperting the observational data as our understanding of the nuclear matter equation of state continues to improve.

- With the large neutrino detectors currently in place, a nearby (galactic) supernova would likely produce incredibly detailed light-curve information, including information about the flavor-specific light curves for ν_e, $\bar{\nu}_e$, and the heavy flavors ν_X. Several aspects of these light curves depend quite sensitively on the phase structure of matter at high densities. In particular, as was discussed in Chapter 2, neutrino opacities in NS matter can be significantly enhanced by coherent scattering from exotic phase droplets. It has been suggested in the literature, then, that a nearby supernova should be expected to yield detailed information about the size, radial extent, and particle content of droplets of exotic matter in the PNS core [61]. The nucleation rate calculations from Chapter 4 demonstrate, however, that (at least in the case of a first-order transition to kaon condensed matter) exotic mixed phase regions will not appear until, at the earliest, the end of the deleptonization phase of PNS evolution. By this time, much of the original neutrino content has been radiated away, so one is therefore not likely to see the imprint of exotic phases on (at least) the early part of the neutrino light curves.

- As the PNS temperature is still of order $10MeV$ when the electron neutrino fraction drops to zero, a strange mixed phase may leave a possibly observable imprint on the late-time neutrino cooling curve. The exact nature of this imprint will clearly depend sensitively on the exact time (and hence temperature) at which exotic phase droplets first appear. Quantitative estimates of the effects of various nucleation scenarios on observed neutrino light curves should be performed as an extension of the work presented here. In addition, the appearance of new phases of matter in neutron star interiors may potentially affect the long-time cooling rates — for example, the increased proton content of a kaon condensed star (recall that the reduction in symmetry energy is a major reason for the favorability of this phase) may allow the direct Urca

cooling processes (discussed in Chapter 2) to occur in regions of the star that would otherwise cool by slower mechanisms. It is thus possible that a post-deleptonization phase transition could leave an observable imprint on the neutron star surface temperature curve: for example, a sudden jump in the surface temperature cooling rate would signal a change in the star's internal composition. Again, the question of how such a signal might be distinguished from other effects, and the question of exactly when the new mixed phase forms under different evolution scenarios, are attractive areas for future work.

- In addition to the burst of neutrinos produced by a supernova, the explosion mechanism itself is quite sensitive to the structure of matter at high density. As supernova modelers continues to improve the quality of neutrino transport and hydrodynamic codes, and as the size and speed of available computers continue to increase, it is expected that at some point the dominant uncertainty will be due to our lack of knowledge of the equation of state of matter at super-nuclear densities. As mentioned before, for example, softer equations of state produce deeper and therefore more energetic bounces, while stiffer equations of state cause quicker and less energetic bounces. Thus, in addition to affecting the cold NS maximum mass, the possibly large changes to the critical densities for the appearance of new phases generated by finite-size effects in mixed phases may also affect the lingering question of how, exactly, supernova explosions occur. It should be noted, however, that the main result of Chapter 4 suggests that exotic phases are highly unlikely to be present during the bounce which produces the supernova shockwave, due to the large lepton content of matter at this time. Thus even if a phase transition to kaon-condensed matter softens the equation of state at $\sim$ 3 times nuclear matter density, this softening will not produce more energetic shockwaves as the softening phase will not be present until much later in the evolutino of the PNS.

- As discussed in Chapter 1, however, the "prompt" supernova mechanism is believed to fail. Instead, a delayed explosion mechanism is favored in which the shockwave stalls

but is re-energized by the tremendous flux of neutrinos escaping the core. As the appearance of kaonic mixed phases requires that the electron neutrino fraction nearly vanish, however, we see that there remains a hand-shaking between the supernova explosion mechanism and the existence of exotic phases in the PNS core. This suggests that ultimately supernova modelers will need to include detailed descriptions of phase transition dynamics (coupled to neutrino transport and hydrodynamics) in order to fully understand the core-collapse explosion mechanism. This is a daunting task, but one for which several significant first steps have been indicated in the work presented here.

We may summarize these various observations by noting that the effects of possible exotic phases of matter in neutron star cores will become increasingly important to understand in the coming years. Let me conclude, then, by simply restating what was asserted in Chapter 1: Much is now known, yet much also remains to be discovered. It is therefore an exciting time, one which appears to be uniquely auspicious for the prospect of profound improvements in our understanding of the structure of matter at super-nuclear densities.

BIBLIOGRAPHY

[1] Steven Weinberg, *Gravitation and Cosmology: Principles and Applications of the General Theory of Relativity*, John Wiley & Sons 1972.

[2] S. Chandrasekhar, Astrophys. J. **74** (1931) 81.

[3] N.K. Glendenning, *Compact Stars: Nuclear Physics, Particle Physics, and General Relativity*, Springer 1997

[4] H.A. Bethe and J.R. Wilson, Astrophys. Jl. **295**, (1985) 14-23

[5] A. Mezzacappa, astro-ph/0010580

[6] J.R. Oppenheimer and G.M. Volkoff, Phys. Rev., **55** (1939) 374 R.C. Tolman, Phys. Rev. **55** (1939) 364

[7] R.M. Bionta *et al.*, Phys. Rev. D **37** (1988) 3361

[8] K. Hirata *et al.*, Phys. Rev. D **38** (1988) 448

[9] A. Hewish, S.J. Bell, J.D.H. Pikington, P.F. Scott and R.A. Collins, Nature **217** (1968) 709

[10] D.C. Backer et al., Nature **300** (1982) 615

[11] R.A. Hulse and J.H. Taylor, Astrophys. J. (Letters) **191** (1974) L59

[12] S.E. Thorsett and D. Chakrabarty, Astrophysical Journal **512** (1999) 288

[13] J. Pons, F. Walter, J. Lattimer, M. Prakash, R. NeuHauser, and P. An, Astrophys. Jl. **564**, (2002) 981-1006

[14] F.M. Walter and J. Lattimer, astro-ph/0204199

[15] M.H. van Kerkwijk, astro-ph/0110336

[16] H. Heiselberg and M. Hjorth-Jensen, Phys. Rep. **328** (2000) 237-327

[17] H. Heiselberg, Int. J. Mod. Phys. **B 15** (2001) 1519-1534

[18] M.H. van Kerkwijk, Astronomy and Astrophysics **303** (1995) 497

[19] J.A. Orosz and E. Kuulkers, astro-ph/9901177

[20] W. Zhang, T.E. Strohmayer and J.H. Swank, Ap J Lett **482**(1997) L167
W. Zhang et al., Ap J Lett **500** (1998) L171

[21] P. Kaaret, E. Ford, and K. Chen, Ap J Lett **480** (1997) L27

[22] C.J. Pethick and D.G. Ravenhall, Ann. Rev. Nucl. Part. Sci. **45** (1995) 429

[23] G. Baym, H.A. Bethe and C.J. Pethick, Nucl. Phys. **A175**, (1971) 225-271

[24] E. Wigner and F. Seitz, Phys Rev **43** (1933) 804

[25] U. Weber and J.A. McGovern, Phys Rev C **57** (1998) 3376

[26] P. Magierski and P. Heenen, Phys Rev C **65** (2002) 045804

[27] V.G.J. Stoks *et al.*, Phys Rev C **49** (1994) 2950

[28] R.B. Wiringa *et al.*, Phys Rev C **51** (1995) 38

[29] R. Machleidt et al., Phys Rev C **53** (1996) R1483

[30] H. Heiselberg and V. Pandharipande, Ann. Rev. Nucl. Part. Sci. **50** (2000) 481-524

[31] B. Friedman and V.R. Pandharipande, Nucl. Phys. **A361**, (502) 1981

[32] A. Akmal, V.R. Pandharipande, and D.G. Ravenhall Phys. Rev. C **58**, (1998) 1804

[33] J.D. Walecka, Ann. Phys. (N.Y.) **83** (1974) 491

[34] R.J. Furnstahl and B.D. Serot, Comments Nucl. Part. Phys. **2** (2000) A23

[35] B. Serot and J. D. Walecka, *Advances in Nucl. Physics*, **16**, edited by J. W. Negele and E. Vogt (Plenum, New York, 1986)

[36] S. Balberg and S.L. Shapiro, astro-ph/0004317

[37] A.B. Migdal, Rev. Mod. Phys., Vol. 50 (1978) 107-172

[38] W.H. Dickhoff *et al.*, Nuc. Phys. A **405** (1983) 534

[39] J.C. Collins and M.J. Perry, Phys. Rev. Lett. **34**. (1975) 1353

[40] C.Alcock, E. Farhi, and A. Olinto, ApJ **310** (1986) 261-272

[41] N.A. Gentile et al., ApJ **414** (1993) 701-711

[42] A. Steiner, M. Prakash, J.M. Lattimer, Phys. Lett. **486B**, (2000) 239-248

[43] K. Huang, *Statistical Mechanics*, John Wiley & Sons, 1963

[44] N.K. Glendenning, J. Phys. G **23** (1997) 2013-2027

[45] D. Kaplan and A. Nelson, Phys. Lett. **175B**, (1986) 57

[46] M. Prakash *et al.*, Physics Reports 280 (1997) 1-77

[47] N. K. Glendenning, Phys. Rev. D **46**, (1992) 1274

[48] N.K. Glendenning and S. Pei, Phys. Rev. C **52**, (1995) 2250

[49] N. K. Glendenning, and J. Schaffner-Bielich, Phys. Rev. Lett. **81**, (1998) 4564
N. K. Glendenning, and J. Schaffner-Bielich, Phys. Rev. C **60**, (1999) 025803

[50] H. Heiselberg, C. J. Pethick, and E. F. Staubo, Phys. Rev. Lett. **70**, (1993) 1355

[51] J. A. Pons, S. Reddy, P. Ellis, M. Prakash, and J. M. Lattimer Phys. Rev. C **62**, (2000) 035803

[52] V. Thorsson, M. Prakash, and J. M. Lattimer, Nucl. Phys. **A572**, (1994) 693

[53] E. Friedman, A. Gal, and C. J. Batty, Nucl. Phys. **A579**, (1994) 578

[54] A. Ramos and E. Oset, Nucl. Phys. **A671**, (2000) 481

[55] A. Cieply, E. Friedman, A. Gal, and J. Mares, Nucl. Phys. A **696** (2001) 173-193

[56] E. Oset *et al.*, Acta Phys. Polon. **B 31** (2000) 2285
A. Ramos *et al.*, Nucl. Phys. A **691** (2001) 258

[57] F. Laue et al., Phys. Rev. Lett. **82** (1999) 1640

[58] D. G. Ravenhall, C. J. Pethick and J. R. Wilson Phys. Rev. Lett. **50**, (1983) 2066

[59] C. J. Pethick and D. G. Ravenhall, Annu. Rev. Nucl. Part. Sci. **45** (1995) 429

[60] M. Christiansen, N. K. Glendenning, and J. Schaffner-Bielich, Phys. Rev. C **62**, (2000) 025804

[61] S. Reddy, G. F. Bertsch, and M. Prakash, Phys. Lett. **475B**, (2000) 1

[62] L. Bildsten and G. Ushomirsky, Astrophys. Jl. **529**, (2000) L33

[63] J. A. Pons, J. A. Miralles, M. Prakash, and J. M. Lattimer, Astrophys. J. **553** (2001) 382

[64] W. D. Myers and W. J. Swiatecki, Ann. Phys. (NY) **55**, (1969) 395

[65] M. Prakash, I. Bombaci, M. Prakash, P. J. Ellis, P. J. Ellis, J. M. Lattimer and R. Knorren, Phys. Rep. **280**, (1997) 1

[66] S. Coleman, *Aspects of Symmetry*, Cambridge University Press, 1985

[67] J.S. Langer Ann. Phys. (NY) **54**, (1969) 258-275

[68] A.D. Linde Nucl. Phys. **B216**, (1983) 421-445

[69] E.M. Lifshitz and L.P. Pitaevskii *Physical Kinetics*, Pergamon Press, 1981

[70] K. Iida and K. Sato Prog. Theor. Phys. **98** (1997) 277-282

[71] N.A. Gentile, M.B. Aufderheide, G.J. Mathews, F.D. Swesty, G.M. Fuller Astrophys. Jl. **414**, (1993) 701-11

[72] S. Alamoudi *et al.* Phys. Rev. D **60**, (1999) 125003

[73] M.L. Olesen and J. Madsen Phys. Rev. D **49**, (1994) 2698-2702

[74] H. Heiselberg, hep-ph/9501374

[75] P. Shukla, A.K. Mohanty, and S.K. Gupta Phys. Rev. C **62**, (2000) 054904

[76] J. Pons et al., Phys. Rev. C **62**, (035803) 2000

[77] D.Q. Lamb *et al.* Nucl. Phys. **A411**, (1983) 449-473

[78] D.G. Ravenhall, C.J. Pethick, and J.R. Wilson Phys. Rev. Lett. **50**, (1983) 2066-9

[79] H. Heiselberg, C.J. Pethick, and E.F. Staubo Phys. Rev. Lett. **70**, (1993) 1355-9

[80] J. Lorenzana, C. Castellani, and C. DiCastro, cond-mat/0010092

[81] T. Norsen and S. Reddy Phys. Rev. C **63**, (2001) 065804

[82] M.B. Christiansen and N.K. Glendenning Phys. Rev. C **56**, (1997) 2858

[83] M. Christiansen, N.K. Glendenning, and J. Schaffner-Bielich Phys. Rev. C **62**, (2000) 025804

[84] J.A. Pons, J.A. Miralles, M. Prakash, and J.M. Lattimer Astrophys. Jl. **553**, (2001) 382-393

[85] G.D. Moore and K. Rummukainen, Phys. Rev. D **63** (2001) 045002

[86] T. Muto, T. Tatsumi, and N. Iwamoto Phys. Rev. D **61**, (2000) 063001
T. Muto, T. Tatsumi, and N. Iwamoto Phys. Rev. D **61**, (2000) 083002

[87] Z. Dai, T. Lu, and Q. Peng Phys. Lett. **319B**, (1993) 199-202

[88] S.K. Ghosh, S.C. Phatak, and P.K. Sahu Nucl. Phys. **A596**, (1996) 670-83

[89] K. Griest, E.W. Kolb, and A. Massarotti Phys. Rev. D **40**, (1989) 3529

[90] D. Metaxas Phys. Rev. D **63**, (2001) 083507

[91] M. Postma, Phys. Rev. D **65** (2002) 085035

[92] S. Coleman Nucl. Phys. **B262**, (1985) 263

[93] K.M. Benson and L.M. Widrow Nucl. Phys. **B353**, (1991) 187

[94] K. Lee Phys. Rev. Lett. **61**, (1988) 263

[95] K. Lee Phys. Rev. D **50**, (1994) 5333

[96] K.S. Cheng and Z.G. Dai Phys. Rev. Lett. **77**, (1996) 1210

[97] M.G. Alford, K. Rajagopal, and F. Wilczek, Phys. Lett. **422B**, (1998) 247

[98] R. Rapp, T. Schaefer, E.V. Shuryak, and M. Velkovsky, Phys. Rev. Lett. **81**, (1998) 53

[99] D.T. Son, Phys. Rev. D **59**, (1999) 094019

[100] K. Rajagopal and F. Wilczek, Phys. Rev. Lett. **86** (2001) 3492

[101] P. F. Bedaque, Nuc. Phys. A **697** (2002) 569

[102] D.T. Son and M. A. Stephanov, Phys. Rev. D **61**, (2000) 074012 erratum. *ibid.* Phys. Rev. D **62**, (059902) 2000

[103] P.F. Bedaque and T. Schaefer, Nuc. Phys. A **697** (2002) 802

[104] D. Kaplan and S. Reddy, Phys. Rev. D **65** (2002) 054042

[105] S.R. Beane, P.F. Bedaque and M.J. Savage, Phys. Lett. **483B**, (2000) 131

[106] C. Manuel and M.H. Tytgat, Phys. Lett. **501B**, (2001) 200

[107] N.K. Glendenning, Phys. Rev. D **46**, (1992) 1274

[108] D.Q. Lamb, J.M. Lattimer, C.J. Pethick, and D.G. Ravenhall, Nucl. Phys. **A411**, (1983) 449
H. Heiselberg, C.J. Pethick, and E.F. Staubo, Phys. Rev. Lett. **70**, (1993) 1355
N.A. Gentile, M.B. Aufderheide, G.J. Mathews, F.D. Swesty, and G.M. Fuller, Astrophys. Jl. **414**, (1993) 701
A. Steiner, M. Prakash, and J.M. Lattimer nucl-th/0003066
N.K. Glendenning and J. Schaffner-Bielich, Phys. Rev. C **60**, (1999) 025803

[109] M. Alford, K. Rajagopal, S. Reddy, F. Wilczek, Phys. Rev. D **64** (2001) 074017

[110] C. Manuel, Phys. Rev. D **53**, (1996) 5866

[111] E. Braaten, Can. J. Phys. **71** (1993) 215

[112] D. T. Son, hep-ph/0108260

[113] P. F. Bedaque, Phys. Lett. B **524** (2002) 137

[114] S. Coleman and E. Weinberg, Phys. Rev. D **7**, (1973) 1888

[115] S. Reddy, G. Bertsch, and M. Prakash Phys. Lett. **475B**, (2000) 1-8

[116] D.B. Kaplan and S. Reddy, Phys. Rev. Lett. **88** (2002) 132302

[117] J.F. Donoghue, E. Golowich, and B.R. Holstein, *Dynamics of the Standard Model.* Cambridge University Press, 1992.

[118] C. Caso *et al.* (Particle Data Group), European Phys. J. C **63** (19998) 1

[119] R.J. Furnstahl and B.D. Serot, Nuc. Phys. A **671** (2000) 447

[120] D. Montano, H.D. Politzer, and M.B. Wise, Nuc. Phys. B **375** (1992) 507

[121] N. Kaiser, S. Fritsch, and W. Weise, Nuc. Phys. A **697** (2002) 255

[122] D.J. Scalapino, Phys. Rev. Lett. **29** (1972) 386

[123] M. Rho, Phys. Rep. **240** (1994) 1

[124] D.P. Min, Y. Oh, B.Y. Park, and M. Rho, Int. J. Mod. Phys. E **4** (1995) 47

[125] G.E. Brown and M. Rho, Nuc. Phys. A, **596** (1996) 503

Appendix A

METASTABLE STATE DECAY

In Chapter 4, we explore the question of how, when, and if droplets of kaon-condensed matter nucleate (i.e., spontaneously appear) during the formation of a neutron star. Here, we will review the general physics involved in calculating the rate at which a metastable field configuration transitions (via either quantum tunneling or thermal activation) to the true ground state.

A.1 Quantum Tunneling and Metastability

Suppose that a particle of mass m finds itself near $x = 0$ and subject to the potential shown in Figure A.1. Assuming the particle's energy E is much less than the height of the barrier between $x = 0$ and $x = x_0$, we know that — according to classical mechanics — the particle will be trapped for all time near $x = 0$. According to quantum mechanics, however, the particle has a nonzero probability of tunneling through the barrier and thus reaching the region near $x = x_0$ where its energy will be as low as possible for this $V(x)$. The classically stable configuration in which the particle is located at $x = 0$, we say, has been rendered "metastable" by quantum mechanics. This means the classically stable configuration will decay away in time, but with a potentially very long timescale.

We can estimate the decay timescale using the WKB approximation. Physically, this amounts to breaking the barrier region between $x = 0$ and $x = x_0$ up into a number of narrow regions of width Δx and assuming that each region is made sufficiently narrow that the potential can be approximated by the first (constant) term in its Taylor expansion:

$$\begin{aligned} V(x) &= V(x_i) + (x - x_i)V'(x_i) + \frac{1}{2}(x - x_i)^2 V''(x_i) + \cdots \\ &\approx V(x_i) \end{aligned} \tag{A.1}$$

where x_i is the point in the center of the i'th region. We also assume that each region is wide

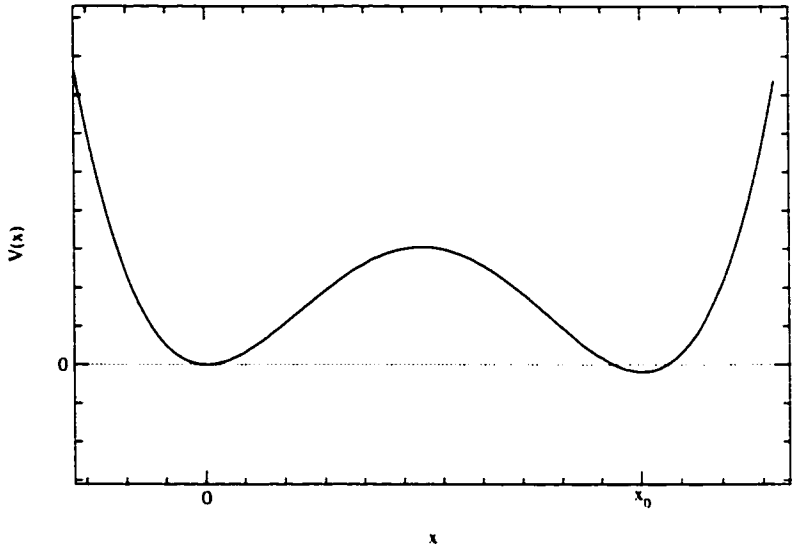

Figure A.1: Potential energy as a function of position for a 1-D quantum mechanical particle. The state localized near $x = 0$ is a local minimum of the potential, but not a global minimum. Hence the particle has a nonzero probability of tunneling through the barrier in order to reach the absolute ground state near $x = x_0$.

compared to the length scale over which the wave function fluctuates. These constraints, taken together, require that the potential be a slowly- and smoothly-varying function of x, i.e., one satisfying

$$\left|\frac{V'(x)}{V(x)}\right| \ll |k| \tag{A.2}$$

where $k = p/\hbar = \sqrt{2mE}/\hbar$ is the wave number of the particle. In the spatial region between x_i and x_{i+1} the wave function may then be treated as a dying exponential, $\psi(x) \sim \exp(-\kappa x)$ where $\kappa^2 = -p^2/\hbar^2$. (In the barrier region, $E < V$, so $p = \sqrt{2m(E-V)}$ is imaginary and hence κ is real.) If the particle's wave function begins on the left side of the barrier with amplitude A, it will thus be reduced by a factor $\exp\left[-\sqrt{2m\,(V(x_1) - E)}\Delta x/\hbar\right]$ in the first region surrounding x_1. The second region will reduce the amplitude by an identical factor evaluated at $x = x_2$, etc. By the time we reach the classical escape point near x_0 the wave function has been reduced to

$$\psi(x_0) \;\sim\; A \prod_i \exp\left(-\sqrt{2m(V(x_i) - E)}\Delta x/\hbar\right)$$

$$= A \exp\left\{-\frac{1}{\hbar}\int_0^{x_0} \mathrm{d}x[2m(V(x)-E)]^{1/2}\right\}. \qquad \text{(A.3)}$$

The barrier transmission amplitude in the WKB approximation is then simply given by the ratio of the wave function magnitude near $x = x_0$ to that near $x = 0$. That is,

$$|T(E)| = \exp\left\{-\frac{1}{\hbar}\int_0^{x_0} dx\ [2m(V(x)-E)]^{1/2}\right\} \qquad \text{(A.4)}$$

and the probability of tunneling through the barrier is given by $|T(E)|^2$.

In order to prepare for a discussion of the analogous metastable state decay process in quantum field theory, let us rederive this result using the path integral formalism. The starting point will be the usual expression for the amplitude of a particle to move from x_i to x_f in a time t:

$$< x_f|e^{-iHt/\hbar}|x_i > = C\int [Dx(t)]\ e^{-iS/\hbar} \qquad \text{(A.5)}$$

where $H = p^2/2m + V(x)$ is the Hamiltonian and $S = \int \mathrm{d}t(\frac{1}{2}m\dot{x}^2 - V(x))$ is the clasical action for the path $x(t)$. It will be useful to analytically continue to imaginary time, so let us write the above in terms of the imaginary time $\tau = it$:

$$< x_f|e^{-H\tau/\hbar}|x_i >= C\int [Dx(\tau)]e^{-S_E/\hbar} \qquad \text{(A.6)}$$

where now $S_E = \int \mathrm{d}\tau(\frac{1}{2}m\dot{x}^2 + V(x))$ is the Euclidean action and $\dot{x} = dx(\tau)/d\tau$ is the derivative with respect to imaginary time.

The left hand side of Equation A.6 is of interest because it can be used to learn something about the ground state energy of the system. Expanding in energy eigenstates $|n >$ we have

$$< x_f|e^{-HT/\hbar}|x_i >= \sum_n < x_f|n >< n|x_i > e^{-E_nT/\hbar}. \qquad \text{(A.7)}$$

Thus in the limit $T \to \infty$ the ground state energy E_0 can be read off from the leading term. To show how this works, let us use this method to calculate the energy of a particle localized near $x = 0$ in the potential of Figure A.1. We will thus consider the amplitude

$$< x = 0|e^{-HT/\hbar}|x = 0 >= C\int [Dx(\tau)]\exp\left\{-\frac{1}{\hbar}\int_0^T \frac{m}{2}(\dot{x}^2 + \omega^2x^2)d\tau\right\} \qquad \text{(A.8)}$$

where $\omega = V''(0)$ is the classical frequency of small-amplitude oscillations around $x = 0$. (Note that really the factor of $m\omega^2x^2$ in the integrand should be replaced by $V(x)$, a difference which would amount to nothing if the potential were exactly that of a simple harmonic

oscillator: $V(x) = m\omega^2 x^2$. Since our potential is more complicated, this approximation will cause us to omit some interesting physics which will have to be recovered by hand later.)

Since we have fixed the endpoints (i.e., $x = 0$ at $\tau = 0, T$) we can parametrize all possible paths $x(\tau)$ in a Fourier series

$$x(\tau) = \sum_{n=1}^{N} a_n \sin\left(\frac{n\pi\tau}{T}\right) \tag{A.9}$$

and rewrite the integration over all paths $x(\tau)$ as separate integrations over the expansion coefficients a_n. Note here we are assuming that the time interval $(0, T)$ has been broken up into $N + 1$ chunks of equal size. Thus the change of variables is from the value of x at each of the N intermediate times to the N distinct a_n. The Jacobian for this transformation is known, but will not concern us since it is independent of ω — we will simply absorb this uninteresting constant into the already-undefined normalization constant C.

Making this change of variables, the integral in the exponential becomes

$$\int_0^T \frac{m}{2}(\dot{x}^2 + \omega^2 x^2) d\tau = \frac{m}{2}\frac{T}{2}\sum_n a_n^2 \left[\left(\frac{n\pi}{T}\right)^2 + \omega^2\right] \tag{A.10}$$

and we are left with N independent Gaussian integrals over the a_n. Performing these integrals gives

$$\begin{aligned} < 0|e^{-HT/\hbar}|0 > &= C\prod_{n=1}^{N}\left(1 + \frac{\omega^2 T^2}{n^2\pi^2}\right)^{-1/2} \\ &= C'\left(\frac{\sinh(\omega T)}{\omega T}\right)^{-1/2}. \end{aligned} \tag{A.11}$$

For future reference, it is worth noting that the functions we have used to expand around the classical solution (namely, the $\sin(n\pi\tau/T)$ for $n = 1, ..., N$) are eigenfunctions of the operator $(-\partial_\tau^2 + \omega^2)$:

$$(-\frac{d^2}{d\tau^2} + \omega^2)\sin\left(\frac{n\pi\tau}{T}\right) = \lambda_n \sin\left(\frac{n\pi\tau}{T}\right) \tag{A.12}$$

with eigenvalues $\lambda_n = \omega^2 + n^2\pi^2/T^2$. Thus, an elegant way of writing the previous result is in terms of the functional determinant of this operator:

$$< 0|e^{-HT/\hbar}|0 >= C''\left[\det(-\partial_\tau^2 + \omega^2)\right]^{-1/2}. \tag{A.13}$$

We may now take the the $T \to \infty$ limit of the result, and read off the ground state energy. In this limit, $\sinh(\omega T) \to \exp(\omega T)$ and we find that

$$< 0|e^{-HT/\hbar}|0 >= \frac{C'}{(\omega T)^{-1/2}} \exp[-\frac{1}{2}\hbar\omega T/\hbar] \; + \; \cdots \tag{A.14}$$

and we can immediately identify

$$E_0 = \frac{1}{2}\hbar\omega. \tag{A.15}$$

This is the expected result for the quantum zero-point energy of a particle in an oscillator potential. Note that this result would be exact in the case $V(x) = m\omega^2 x^2$. We got it by expanding $V(x) = V(0) + xV'(0) + \frac{1}{2}x^2V''(0) + \cdots$ and keeping only the terms shown.

Our real potential shown in Figure A.1, however, is not simply quadratic, so we expect additional contributions to the ground state energy E_0. In particular, since we know that the state localized near $x = 0$ is metastable, we expect E_0 to develop an imaginary component, whose magnitude we will associate with the decay rate of this state. That is the quantity we are really interested in calculating.

It can be shown [66] that the leading contribution to the imaginary part of E_0 arises from paths which begin at $x = 0$ at $\tau = -T/2$, cross through the boundary and explore the region near $x = x_0$ for a finite time near $\tau = 0$, then cross back through the boundary and settle down to $x = 0$ as $\tau \to T/2$. We can find the classical path which does this by solving the (Euclidean) equation of motion

$$\frac{\delta S_E}{\delta x_{bounce}} = 0 \tag{A.16}$$

subject to the boundary conditions $x_{bounce}(-T/2) = x_{bounce}(T/2) = 0$ as well as $dx_{bounce}/d\tau|_{\tau=0} = 0$. This path was named "the bounce" by Sidney Coleman. The reason for this is that the Euclidean equation of motion above is equivalent to the normal equation of motion for a particle moving in a potential $-V(x)$. The bounce solution then refers to a trajectory in which the particle starts off at the top of the hill near $x = 0$ (which is a hill rather than a well because the potential is upside down!), slides down the well to its right and bounces off the classical turning point near $x = x_0$ at $\tau = 0$, and then finally returns to rest at $x = 0$.

(I have actually simplified a bit in the above description. The case of a single degree of freedom is unique in that the contribution to the path integral is independent of the number of distinct bounces. So the correct "bounce solution" is actually a sum over all possible numbers of back-and-forth traversals of the barrier. The description involving a single bounce with a well-defined location and width in imaginary time, however, is correct for the case of several degrees of freedom. Since we are ultimately interested in the field theory case in which the number of degrees of freedom is taken to infinity, we will retain the slightly imprecise but pedagogically useful description of a single well-defined bounce.)

In any case, we may follow essentially the procedure outlined before to calculate the contribution of this path (and the ones near it) to the ground state energy E_0. As advertised, this contribution turns out to be imaginary — this can be understood from the fact that one of the eigenvalues λ_n that comes in when we consider small fluctuations about $x_{bounce}(\tau)$ is negative. This occurs because the bounce configuration lies at a saddle point in configuration space. Hence, the functional determinant is the product of one negative number and several positive numbers, and its square root (the quantity appearing in Equation A.13) will be imaginary. (Actually, there is also a zero eigenvalue coming from the stationarity of the action under translations in the time of the bounce - this degree of freedom is integrated over explicitly, so the zero eigenvalue is omitted from the functional determinant.)

We will here simply quote the result, as we need to move on and discuss the generalization to field theory. For the details of the calculation, see Coleman's book [66]. The result is again an expression for the $x = 0 \rightarrow x = 0$ transition amplitude:

$$< 0|e^{-HT/\hbar}|0 >= \left(\frac{\omega}{\pi\hbar}\right)^{1/2} e^{-\omega T/2}\exp[KTe^{-S_0/\hbar}] \tag{A.17}$$

from which we read off the ground state energy

$$E_0 = \frac{1}{2}\hbar\omega + \hbar K e^{-S_0/\hbar}. \tag{A.18}$$

Here $\Gamma = \mathrm{Im}E_0/\hbar = |K|e^{-S_0/\hbar}$ is the decay rate of the metastable configuration in which the particle is located near $x = 0$. Note that as promised the new contribution to E_0 is proportional to K — a pure imaginary number. S_0 is the (Euclidean) action associated

with the one-way traversal of the barrier:

$$\begin{aligned} S_0 &= \int d\tau \left[\frac{1}{2}m(dx/d\tau)^2 + V(x)\right] \\ &= \int d\tau m(dx/d\tau)^2 \\ &= \int_0^{x_0} dx\,(2V(x))^{1/2}\,. \end{aligned} \tag{A.19}$$

which we recognize as the integral appearing in the WKB formula for the barrier transmission probability derived at the beginning of the chapter.

Finally, the constant K can be written formally as a ratio of functional determinants:

$$K = \left(\frac{S_0}{2\pi\hbar}\right)^{1/2} \left|\frac{\det(-\partial_\tau^2 + \omega^2)}{\det'(-\partial_\tau^2 + V''(x_{bounce}))}\right|^{1/2} \tag{A.20}$$

where the prime on "det" indicates that the zero eigenvalue mentioned above is not to be included. (The zero eigenvalue actually gives rise to the overall factor of $\sqrt{S_0/2\pi\hbar}$.) The presence of a single negative eigenvalue in the functional determinant gives rise to a pure imaginary K.

A few words are in order about this result. We have shown that the decay rate of a metastable state due to quantum tunneling can be written

$$\Gamma = \Gamma_0\, e^{-S_0/\hbar} \tag{A.21}$$

where Γ_0 is a constant with dimensions of $[time]^{-1}$ which can be written formally in terms of functional determinants. It can be understood physically as a microscopic fluctuation rate characterizing the rate at which quantum fluctuations allow the metastable system to explore other possible configurations. The exponential factor depends on the classical (Euclidean) action associated with the so-called bounce solution in which the system tunnels through the barrier and then tunnels back to its initial configuration. We will see later that this exponential factor not only gives the most important contribution to the metastable state decay rate in many important cases, but also that it can be calculated in a straightforward way. First, though, let us generalize the above to the case of an infinite number of degrees of freedom, which is what we need for a discussion of metastable state decay in field theory.

A.2 Metastable State Decay in Field Theory

Let us assume that we again have a potential as shown in Figure A.1. Now, however, we interpret the picture as describing the potential energy per unit volume as a function of the value of a scalar field ϕ: $U = U(\phi)$. To be explicit, the Lagrangian (density) for this fieldwill be given by

$$\mathcal{L} = \frac{1}{2}\partial^{\mu}\phi\,\partial_{\mu}\phi - U(\phi) \tag{A.22}$$

from which we can derive the Euclidean equation of motion:

$$\left(\frac{\partial^2}{\partial\tau^2} + \nabla^2\right)\phi = \frac{\partial U(\phi)}{\partial\phi}. \tag{A.23}$$

Let us assume that the potential has the explicit form

$$\begin{aligned} U(\phi) &= U_0(\phi) - \epsilon\phi \\ &= \lambda\phi^2(\phi - \phi_0)^2 - \epsilon\phi \end{aligned} \tag{A.24}$$

where λ and ϕ_0 are constants. For $\epsilon < 0$, the well on the right is higher than the well on the left, and a configuration in which $\phi(\vec{r}) = 0$ will be the true ground state of the system. For $\epsilon > 0$ this configuration will be rendered unstable by quantum tunneling through the barrier to the configuration in which $\phi = \phi_0$. This, of course, will be the case we are interested in. We can solve the problem analytically in the case of very small ϵ, which is the case shown in Fig. A.1.

Physically, we may guess that the initial metastable configuration in which $\phi = 0$ everywhere will decay by nucleating a seed of the true ground state through a quantum fluctuation. A sufficiently large seed will then grow in size and take over the universe, completing the transition to the energetically favored phase with $\phi = \phi_0$.

Let us assume this process can be described by an $O(4)$-symmetric solution to the Euclidean equations of motion. In this case, we may write $x = \sqrt{\tau^2 + \vec{r}^2}$ and assume the bounce configuration $\phi_B(\vec{r}, \tau) = \phi_B(x)$ only. The Euclidean equation of motion in terms of the variable x reads:

$$\frac{d^2\phi_B(x)}{dx^2} + \frac{3}{x}\frac{d\phi_B(x)}{dx} = \frac{\partial U(\phi)}{\partial\phi}. \tag{A.25}$$

Just as in the 1-D quantum mechanics problem, the bounce solution is subject to the following boundary conditions:

$$\lim_{|\vec{r}|\to\infty} \phi_B = 0 \tag{A.26}$$

which says that the field remains at the metastable value at spatial infinity during the quantum fluctuation (which is assumed to be centered at the origin — as before, translational invariance will give rise to zero eigenvalues which will be integrated over explicitly and will therefore not appear in the functional determinant). We also require

$$\lim_{\tau\to\pm\infty} \phi_B = 0 \tag{A.27}$$

which says that the field must begin in and eventually return to the metastable configuration in which $\phi = 0$. Finally, in analogy with the one-degree-of-freedom case, we require

$$\left.\frac{\partial\phi_B}{\partial\tau}\right|_{\tau=0} = 0 \tag{A.28}$$

which means that the configuration is stationary in (imaginary) time at the moment of the bounce. In terms of the $O(4)$-radius variable x, these boundary conditions become

$$\lim_{x\to\infty} \phi_B(x) = 0 \tag{A.29}$$

and

$$\left.\frac{d\phi_B}{dx}\right|_{x=0} = 0. \tag{A.30}$$

For help visualizing this configuration, please see Figure A.2.

By identifying $\phi_B(x)$ with $x_{bounce}(\tau)$ from the previous section, we see that Equation A.25 can be interpreted as the equation of motion for a particle whose potential $V(x)$ is identified with our $U(\phi)$. The only difference is the extra term proportional to $3/x$, which can be interpreted in this 1-D analog as a time-dependent damping force. We expect, however, that this term will be negligible in the small-ϵ limit, since in this limit the particle spends a lot of time in the true ground state phase $\phi = \phi_0$ before returning to $\phi = 0$. Hence, by the time all the action occurs (so to speak) the damping term will be reduced by a factor of order $1/R$ which, as we will show below, is proportional to ϵ. Let us therefore drop this term and come back later to discuss the range of validity of our approximation.

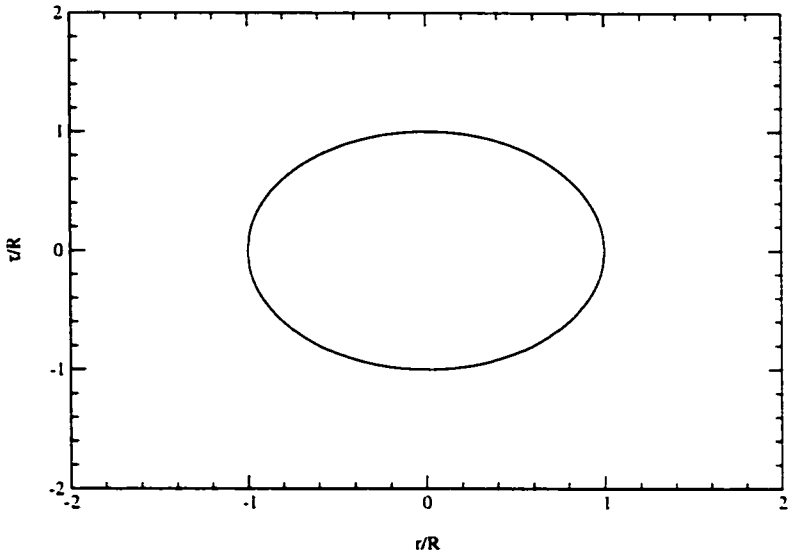

Figure A.2: Schematic representation of the $O(4)$-symmetric bounce solution. The circle represents the boundary layer between the regions where $\phi = 0$ (outside) and $\phi = \phi_0$ (inside). The constant R describes the radius of the bounce (i.e., the value of x at which $\phi_B(x)$ goes from $\phi = \phi_0$ to $\phi = 0$). Note that $r = |\vec{r}|$, so three spatial dimensions are projected onto the horizontal axis of the figure.

The bounce configuration is then quite simple, being given by

$$\phi_B(x) = \begin{cases} \phi_0 & \text{for } x \ll R \\ \phi_t(x) & \text{for } x \approx R \\ 0 & \text{for } x \gg R \end{cases} \tag{A.31}$$

where R is the radius of the bounce, and $\phi_t(x)$ describes the smooth transition from $\phi = \phi_0$ to $\phi = 0$. Since we have thrown out the damping term in Equation A.25, we can write a simple analytic expression for $\phi_t(x)$. The equation of motion to be solved is

$$\frac{d^2\phi_t(x)}{dx^2} = U_0(\phi_t) \tag{A.32}$$

where we have also ignored the small order-ϵ term in $U(\phi)$. The solution is given by

$$x = \int_0^{\phi_t(x)} \frac{d\phi}{[2U_0(\phi)]^{1/2}} \tag{A.33}$$

which, for the quartic double well potential written out above, can be simplified to

$$\phi_t(x) = \frac{\phi_0}{2}\left[1 + \tanh\left(\frac{R-x}{w}\right)\right] \tag{A.34}$$

where $w = (\lambda\phi_0^2/2)^{-1/2}$ measures the width of the transition. This completes our specification of the bounce solution except that the radius R is not yet determined. This can be determined by extremizing the (Euclidean) action associated with the bounce:

$$S_E = 2\pi^2 \int_0^\infty x^3 dx \left[\frac{1}{2}\left(\frac{d\phi_B(x)}{dx}\right)^2 + U(\phi_B)\right]. \tag{A.35}$$

We can approximate this integral as the sum of two terms: one which tallies the cost of the transition between the two phases and is proportional to the "area" of the boundary between them, and another which measures the action savings of sitting near the true ground state and will be proportional to the volume of the $O(4)$-symmetric sphere pictured in Figure A.2.

The first contribution comes from the region around $x \approx R$, so we may write

$$\begin{aligned} S_E^{(surface)} &= 2\pi^2 \int_{x\approx R} x^3 dx \left[\frac{1}{2}\left(\frac{d\phi_B(x)}{dx}\right)^2 + U(\phi_B)\right] \\ &\approx 2\pi^2 R^3 \sigma \end{aligned} \tag{A.36}$$

where

$$\begin{aligned} \sigma &= \int dx \left[\frac{1}{2}\left(\frac{d\phi_t}{dx}\right)^2 + U_0(\phi)\right] \\ &= \int d\phi \sqrt{2U_0(\phi)} \\ &= \frac{\phi_0}{3}\sqrt{\frac{\lambda\phi_0^4}{2}} \end{aligned} \tag{A.37}$$

is the "surface tension" between the $\phi = 0$ and $\phi = \phi_0$ regions.

The second contribution comes from the region $x \ll R$ and is given simply by the value of the potential at ϕ_0 ($U(\phi_0) = -\epsilon\phi_0$) integrated over the 4-sphere of radius R:

$$S_E^{(volume)} = 2\pi^2(-\epsilon\phi_0)\frac{R^4}{4}. \tag{A.38}$$

The total action of the bounce can then be written

$$S_E = \pi^2 \left(R^3\sigma - R^4\phi_0\epsilon/2\right) \tag{A.39}$$

which is extremized for

$$R_{crit} = \frac{1}{\lambda w^3 \phi_0 \epsilon}. \tag{A.40}$$

Thus, as promised, the radius of the bounce is proportional to $1/\epsilon$ and we were justified in ignoring the $\sim 1/R$ damping term in Equation A.25.

This completes our specification of the bounce solution. Note that the extremization just performed is tantamount to finding the location of the saddle point in configuration space — that is, the bounce is precisely the solution which is a local extremum of the Euclidean action with one negative eigenvalue corresponding to the instability of this configuration in the R-direction of configuration space. (If one is curious, it is trivial to show that the second derivative of S_E with respect to R is negative when evaluated at R_{crit}. Hence, the bounce configuration really is unstable along the R-direction, i.e., is a saddle point.) This corresponds exactly to the 1-D problem considered previously, in which the saddle point configuration with a single negative eigenvalue gave the leading contribution to the decay rate of the metastable configuration.

We can thus again write our final result as:

$$\Gamma = \Gamma_0 e^{-S_E/\hbar} \tag{A.41}$$

where, as before, Γ_0 is a microscopic fluctuation rate that can be written explicitly in terms of functional determinants:

$$\Gamma_0 = \left(\frac{S_E(\phi_B)}{2\pi\hbar}\right)^2 \left(\frac{\det[-\Box + V''(0)]}{\det'[-\Box + V''(\phi_B)]}\right)^{1/2}. \tag{A.42}$$

Also as before, S_E is the Euclidean action of the classical bounce configuration. The decay rate Γ now represents the rate (per unit time and per unit volume) at which the initial state $\phi(\vec{r}) = 0$ will decay into the true ground state with $\phi = \phi_0$ everywhere.

A.3 Thermal Nucleation

So far we have been working at zero temperature and have therefore considered quantum tunneling as the only means for a metastable system to decay to the true ground state. At finite temperature, however, the system may also cross the energy barrier by means of thermal activation. It has been known for a long time that the formula for the decay rate of a metastable field configuration should in this case be given by a formula just like Equation A.41 except that the exponential factor there should be replaced by a Boltzmann factor

$\sim \exp(-\Delta F/T)$. (See, e.g., Ref. [67].) Here ΔF is the excess free energy (compared to the uniform metastable configuration) of a critical droplet of the new lower energy phase. The critical droplet is defined as the droplet whose size is just between those which will grow spontaneously and those which will spontaneously shrink, i.e., $\partial \Delta F(R)/\partial R = 0$. The exponential factor can then be understood as simply the Boltzmann factor expressing the probability for a thermal fluctuation to produce a super-critical droplet.

Let us understand how this same physics can be derived from our general expression for the quantum tunneling rate developed in the previous section. The quantum statistics of bosons at $T \neq 0$ is formally equivalent to quantum field theory in Euclidean space with periodic boundary conditions in the imaginary time direction, with period given by $\beta = 1/T$. For very large β, the change from the boundary conditions stated in the previous section to periodic boundary conditions in the τ-direction will have a negligible effect. The only change will be that, instead of the bounce configuration dying off to the metastable phase $\phi = 0$ for large τ, we will now have a widely-separated "string of pearls" with (imaginary time) separation β between their centers. The nonzero temperature will have broken the $O(4)$-symmetric bounce solutions down to a solution that is globally only $O(3)$-symmetric, even though each individual bounce solution will have an almost perfect $O(4)$-symmetry about its center.

At higher temperatures, however, the separation between the centers of adjacent bounces becomes comparable to the radius R, and the configuration which extremizes the Euclidean action subject to the correct boundary conditions will become completely uniform in the τ-direction. Intuitively, we may visualize this as the merging of droplets to form a rod-like structure, exactly analogous to the process described earlier in the context of heterogenous mixed phases in neutron star matter. Of course, in the present case, we have the merging of 4-spheres into a 3-rod in the four-dimensional Euclidean space-time, whereas the earlier case involved the merging of 3-spheres into two-dimensional rods in physical 3-D space. Nevertheless, the physics involved is precisely the same: subject to the given boundary conditions, the overall free energy (or, in the present case, the overall 4-dimensional Euclidean action) is minimized by reducing the surface tension cost by forming a structure of reduced dimensionality.

Once this transition has occurred (i.e., for $\beta \lesssim R$) the 4-dimensional Euclidean action for the "bounce" solution (which, of course, is no longer particularly bouncy) is given by

$$\begin{aligned} S_E &= \int d^4x \left[\frac{1}{2} \left(\frac{d\phi_B}{d\tau} \right)^2 + \frac{1}{2} \left(\vec{\nabla} \phi_B \right)^2 + U(\phi_B) \right] \\ &= \beta S_3 \end{aligned} \tag{A.43}$$

where

$$S_3 = \int d^3x \left[\frac{1}{2} \left(\vec{\nabla} \phi_B \right)^2 + U(\phi_B) \right]. \tag{A.44}$$

is the 3-dimensional Euclidean action. In the case of time-independent fields, however, and assuming $U(\phi = 0) = 0$ (which is the case we have been considering all along), this quantity is nothing but the excess free energy of a (3-) spherically symmetric droplet of the $\phi = \phi_0$ phase immersed in a background of the metastable $\phi = 0$ phase. With the condition on R derived previously, then, we have shown that the factor $\exp(-S_E/\hbar)$ goes smoothly over into the expected Boltzmann factor $\exp(-\Delta F(R_{crit})/T)$ as the temperature is raised above $T \sim R_{crit}^{-1}$.

Thus, at sufficiently high temperature, the barrier penetration rate is indeed dominated by thermal activation and is proportional to the expected Boltzmann factor. In addition, it can be argued that for sufficiently large temperatures, the microscopic fluctuation rates entering into the pre-factor Γ_0 in the rate equation are dominated by thermal fluctuations as well. The pre-factor may then be approximated by dimensional analysis as $\Gamma_0 \sim T^4$ (see, e.g., [68] for details). That is, the total nucleation rate per unit volume will be given by

$$\Gamma \sim T^4 e^{-\Delta F(R_{crit})/T}. \tag{A.45}$$

Calculation of the rate is thus reduced to understanding the low-energy (effective) potential sufficiently that $\Delta F(R)$ can be calculated.

As a final comment, we note that the crucial parameter entering into the functional determinant or pre-factor is the value of λ_{-1}, i.e., the negative eigenvalue corresponding to fluctuations of the droplet along the unstable R-direction in configuration space. For $R \approx R_{crit}$ the free-energy may be expanded as

$$\Delta F(R) \sim \Delta F(R_{crit}) + \frac{1}{2} R^2 \Delta F''(R_{crit}). \tag{A.46}$$

The classical equation of motion for small fluctuations in R is then simply

$$M(R)\ddot{R} = -\frac{d\Delta F(R)}{dR} = \kappa R \tag{A.47}$$

where $\kappa = -\Delta F''(R_{crit})$ and $M(R)$ is some effective mass for oscillations in the size of the droplet. The solution to this equation of motion is simply $R(t) \sim R_0 e^{\pm\omega t}$ (where $\omega = \sqrt{\kappa/M}$) which shows that small perturbations away from the critical size grow (or shrink, in the case of $R < R_{crit}$) exponentially in time. This is, of course, not surprising since (by definition) we are expanding around a point which is unstable. The point here is simply to relate our formulae to similar formulae often encountered in the literature (e.g., in so-called Lifschitz-Kagan theory [69, 70]) in which the pre-factor is said to depend on the "growth rate of a just-supercritical droplet". This rate is nothing but what we have called ω above. More sophisticated treatments allow one to demonstrate the functional dependence of the pre-factor on various other transport properties of the fields, e.g., the viscosity.

In the following chapter we will use this result to study the rate at which droplets of a kaon-condensed phase are formed by thermal fluctuations during the formation of a neutron star.

Appendix B

SOME COMMENTS ON THE WALECKA MODEL, PIONS, AND CHIRAL SYMMETRY

It is well-known that pion-exchange dominates the long-range part of the attractive interaction between nucleons, yet the Walecka model as presented in Chapter 2 does not include pionic degrees of freedom. To understand this, let us add pions and examine the conditions under which they can be expected to have a significant effect. The lowest-order pion-nucleon couplings in $SU(3)$ chiral perturbation theory (leaving aside, for the moment, perturbative corrections proportional to quark masses) are given by

$$\mathcal{L}_{\pi N} = i\,\mathrm{Tr}\bar{B}\gamma^{\mu}\,[V_{\mu}, B] + D\,\mathrm{Tr}\bar{B}\gamma^{\mu}\gamma_5\,\{A_{\mu}, B\} + F\,\mathrm{Tr}\bar{B}\gamma^{\mu}\gamma_5\,[A_{\mu}, B] \tag{B.1}$$

where B is the baryon octet (defined in Chapter 3) and V_{μ} and A_{μ} are, respectively, the vector and axial vector meson currents: $V_{\mu} = \frac{1}{2}(\xi^{\dagger}\partial_{\mu}\xi + \xi\partial_{\mu}\xi^{\dagger})$ and $A_{\mu} = \frac{i}{2}(\xi^{\dagger}\partial_{\mu}\xi - \xi\partial_{\mu}\xi^{\dagger})$. (The traces are over flavor indices.) The meson field $\xi = \Sigma^{1/2} = \exp(i\pi/\sqrt{2}f)$, where π is the pseudoscalar meson octet (also defined in Chapter 3) and $f = 93MeV$ is the pion decay constant. D and F are coupling constants that should be fit to experiment (see below).

Considering only the pion and nucleon degrees of freedom in π and B, and expanding to lowest order in the pion fields, the D and F terms above combine to produce the usual pseudovector pion-nucleon coupling:

$$\mathcal{L}_{\gamma^{\mu}\gamma_5} = \frac{g_A}{2f}\bar{N}\gamma^{\mu}\gamma_5\,\vec{\tau}\,N\cdot\partial_{\mu}\vec{\pi} \tag{B.2}$$

where $\vec{\pi}$ is the isotriplet of pion fields and $N = (\,p\;n\,)^T$ represents the proton and neutron fields. $g_A = D + F = 1.267$ [118] is the usual nucleon axial vector coupling constant. Similarly, the term involving the vector current V_{μ} gives, in lowest order, the Tomozawa-Weinberg (TW) vertex

$$\mathcal{L}_{TW} = \frac{1}{4f^2}\left(\bar{N}\gamma^{\mu}\vec{\tau}\times\vec{\pi}N\right)\cdot\partial_{\mu}\vec{\pi}. \tag{B.3}$$

The pseudovector coupling of Equation B.2 will generate no contribution to the properties of uniform nuclear matter at the mean field level. To see this, one need simply note that the momentum flowing through the pion propagator is constrained to be zero in Hartree diagram contributions to the energy density. However, although one generally expects the Hartree approximation to dominate the bulk properties [119], these diagrams do not exhaust the allowed contributions, and pions may contribute through exchange diagrams ("Fock terms"), etc. Several such contributions have been calculated and they are generally found to be small [35]. [1] The TW interaction does not necessarily vanish in uniform, isospin asymmetric nuclear matter; for neutron-rich matter (relevant to neutron stars), however, this term represents a repulsive interaction between negatively charged pions and baryons. It therefore suppresses a uniform condensate of charged pions. (See Ref. [120] for an excellent discussion of the possibility of charged pion condensation in neutron matter in the $SU(2)$ chiral limit.)

Pions may potentially play a large role in dense hadronic matter if we relax the assumption of uniformity which has been implicit up to this point. Its derivative (pseudovector) coupling allows the pion to couple with the nuclear axial density which, in terms of non-relativistic nucleon wave functions, appears as

$$\psi_N^\dagger \vec{\nabla} \cdot \vec{\sigma} \psi_N \tag{B.4}$$

where $\vec{\sigma}$ is the nucleon spin operator. Hence a spatially-varying pion condensate may form in the presence of a nuclear spin-density wave. In practice, one studies this possibility

[1] This statement is extremely model-dependent, however. The full statement is that the (2-loop) Fock term contributions to the energy density coming from the interaction in Equation B.2 are quite small at reasonable densities near nuclear matter density. However, as has been shown recently in Ref. [121], one can reproduce nuclear matter saturation curves at the $\sim 10\%$ level with nothing but the pion-nucleon interactions above when one goes to the 3-loop level and includes two-pion-exchange diagrams. Actually, in addition to the interaction terms written above, the calculation involves one free parameter (a momentum cutoff) which is fine-tuned to reproduce the empirical saturation density. (Note that using a momentum cutoff to regulate loop integrations may introduce uncontrolled chiral-symmetry-breaking effects; this casts doubt on the authors' claim that they have described nuclear saturation in a fully chiral model.) Nevertheless, that one can generate qualitatively reasonable saturation from pion interactions alone is quite remarkable. In the Walecka model, the effects of two-pion-exchange are hidden in the σ and ω meson fields. The lesson is that although explicit pion physics plays only a small role in the Walecka model, it may play a large (or even dominant) role within the context of other models. The detailed relations among various models — in particular, the extent to which one can reliably calculate the bulk properties of dense matter within chiral models — remains a promising and active area of ongoing research.

by calculating the contributions to the pion self-energy from in-medium nucleon-hole pair excitations. The resulting dispersion relation will show an instability at some particular wavelength in the case that a non-uniform condensate of pions is favored. This has been studied extensively since it was originally suggested in the early 1970's [37, 122]. More recent calculations show that the p-wave pion-nucleon interactions (which are attractive for scattering in vacuum) become repulsive in a dense nuclear medium; this pushes the critical density for pion condensation up to densities which are not likely to be realized in nuclei or neutron star matter [38]. The absense of pion condensation near nuclear matter density is also confirmed by the lack of experimental evidence for a periodic spin-density standing wave in finite nuclei.

To summarize, despite their importance for understanding nucleon-nucleon interactions in vacuum, pions are not expected to play a large role in nuclear matter — at least, within the purview of the Walecka model where the dominant two-pion-exchange interaction is hidden in non-pion degrees of freedom.

Since the pions and kaons live within the same $SU(3)$ multiplet, it is perhaps not obvious why the kaon is thought to possibly play such a large role in dense hadronic matter (in the form of the kaon condensates discussed throughout this work). The kaon and pion have similar derivative couplings to the odd-parity nuclear currents (spin-density waves, etc.) appearing in Equation B.2, so how does the kaon elude the arguments presented above?

The answer is that in the above discussion we assumed the chiral limit (quark masses set to zero). This is an extremely good approximation when we are dealing only with the isospin $SU(2)$ subspace of the full $SU(3)$ chiral theory. Because of the large mass of the strange quark relative to the up and down flavors, however, we must include the effects of explicit chiral symmetry breaking when we talk about kaons and their interactions with nucleons. At leading order in the quark masses (i.e., with one factor of $M = \mathrm{diag}(m_u, m_d, m_s)$) we can write down the following meson-baryon interactions:

$$\begin{aligned}\mathcal{L}_{M^1} &= a_1 \,\mathrm{Tr}\bar{B}(\xi M\xi + \xi^\dagger M^\dagger \xi^\dagger)B + a_2 \,\mathrm{Tr}\bar{B}B(\xi M\xi + \xi^\dagger M^\dagger \xi^\dagger) \\ &\quad + a_3 \,\mathrm{Tr}\bar{B}B \cdot \mathrm{Tr}\left(M(\Sigma - 1) + M^\dagger(\Sigma^\dagger - 1)\right). \qquad \text{(B.5)}\end{aligned}$$

These terms generate 4-point ($\pi\pi NN$) vertices among nucleons and pions which, in prin-

ciple, should have been included in our earlier discussion. However, the pion terms scale as $\frac{a_i m_{u,d}}{f^2} n^{(s)} |\pi|^2$ where $n^{(s)}$ is the (scalar) baryon density. That is, they are suppressed by the small factor $m_{u,d}/f$ and therefore have only a tiny effect on the properties of nuclear matter.

The kaon terms, on the other hand, can be relatively large due to the relatively large strange quark mass. Assuming only charged kaons are present, the interaction terms in Equation B.5 reduce (at leading order in the kaon fields) to:

$$\mathcal{L}_{\Sigma_{KN}} = \frac{\Sigma_{KN}}{f^2} n^{(s)} K^+ K^- \tag{B.6}$$

where $\Sigma_{KN} = -(a_1/2 + a_2 + 2a_3) m_s$. The empirically large value of the term $a_3 m_s$ (related to the strangeness content of the nucleon) is thus seen to produce a strong attractive interaction between charged kaons and nucleons. Of particular importance is the fact that this term couples the kaons to the nucleon scalar density ($\bar{N}N$) rather than the odd-parity densities discussed above for the case of a hypothetical charged pion condensate. This means that a spatially uniform (s-wave) kaon condensate (like the one discussed in Chapters 3 and 4) is favorable at large $n^{(s)}$.

It should be noted that in addition to the kaon-nucleon Σ_{KN}-term there is an attractive interaction coming from the kaon analogue of the Tomozawa-Weinberg term written above for pions. This is

$$\mathcal{L}_{TW(K)} = \frac{3i}{8f^2} n (K^+ \partial_0 K^- - K^- \partial_0 K^+) \tag{B.7}$$

where $n = \bar{N}\gamma^0 N$ is the normal ("vector") baryon density. (Note that in the case of kaons this term describes an attraction to the total baryon number density.) An s-wave kaon condensate therefore couples to both n and $n^{(s)}$. Or, as it is often said, an in-medium kaon receives optical potential contributions from both scalar and vector channels [51]:

$$U_{opt}^{K^-} = S + V = -\frac{\Sigma_{KN} n^{(s)}}{2 m_K f^2} - \frac{3n}{8f^2}. \tag{B.8}$$

In the Walecka model developed in Chapters 3 and 4, the charged kaons interact with nucleons via the exchange of σ and ω (and ρ) mesons rather than the direct point-coupling interactions of the chiral theory. [2] The scalar and vector interactions are thus incorporated

[2]The point-coupling vs. meson-exchange issue is itself somewhat controversial. There is some justification

in this model by the kaon couplings to the scalar (σ) and vector (ω) meson fields:

$$U_{opt}^{K^-}(n_0) = S + V \rightarrow -g_{\sigma K}\sigma_0 - g_{\omega K}\omega_0 \tag{B.9}$$

where σ_0 and ω_0 are the values of the scalar and vector fields in symmetric nuclear matter at saturation (where the optical potential $U_{opt}^{K^-}(n_0)$ is empirically known — see the footnote in Section 3.2). Matching between the chiral (Equation B.8) and meson-exchange (Equation B.9) expressions for the kaon optical potential at nuclear matter density gives the conditions

$$\frac{g_{\omega N} g_{\omega K}}{m_\omega^2} = \frac{3}{8f^2} \tag{B.10}$$

for the vector part of the potential, and

$$\frac{g_{\sigma N} g_{\sigma K}}{m_\sigma^2} = \frac{\Sigma_{KN}}{m_K f^2} \tag{B.11}$$

for the scalar part. (Note the last expression omits the small contributions from σ self-interactions.) The condition on the vector part of the potential is very well satisfied by the parameters used in this work (recall that $g_{\omega K}$ was chosen based on the naive quark counting rule mentioned in Chapter 3). The condition for matching of the scalar part of the potential is not particularly well-satisfied by our parameters, as the coupling constant $g_{\sigma K}$ was fit to produce the empirically-motivated value $U_{opt}^{K^-}(n_0) = -120MeV$.

As discussed in Section 3.2, however, the extraction of the kaon optical potential from experimental data is somewhat model-dependent and remains controversial. One hopes that ultimately chiral theories will succeed in predicting (or, at any rate, postdicting) $U_{opt}^{K^-}(n_0)$. thus greatly increasing our confidence that this model parameter has been extracted correctly from the data. This will most certainly involve going beyond the leading-order K-N couplings discussed here; $m_K/\Lambda_\chi \sim 1/2$, so several additional orders in the expansion may be required to approach even the 10% level of accuracy. In addition, the realistic description of high-density baryonic matter within the chiral theory is in all likelihood a long way off.

for a meson-exchange picture in which one treats kaons as matter fields (on par with the nucleons) from heavy quark physics — see References [123, 124, 125] for more detailed discussions. On the other hand, the chiral theory is clearly the safest approach in terms of generating K-N interactions in a reliably converging expansion. Suffice it to say that these and related issues (for example, using the chiral expansion to estimate the size of higher-order kaon self-interactions [51] which potentially modify the in-medium effective potential for kaons) are ripe for further exploration.

In the meantime, then, the meson-exchange picture of kaon-nucleon interactions remains an efficient (though non-rigorous) way to describe the strong interactions of kaons and nucleons in a model that can be easily extrapolated to densities relevant to the cores of neutron stars.

VITA

Travis is excited and optimistic about the next phase of his life: being married to Sarah, teaching physics to undergraduates, and pursuing, at long last, the physics issues *he* finds important.